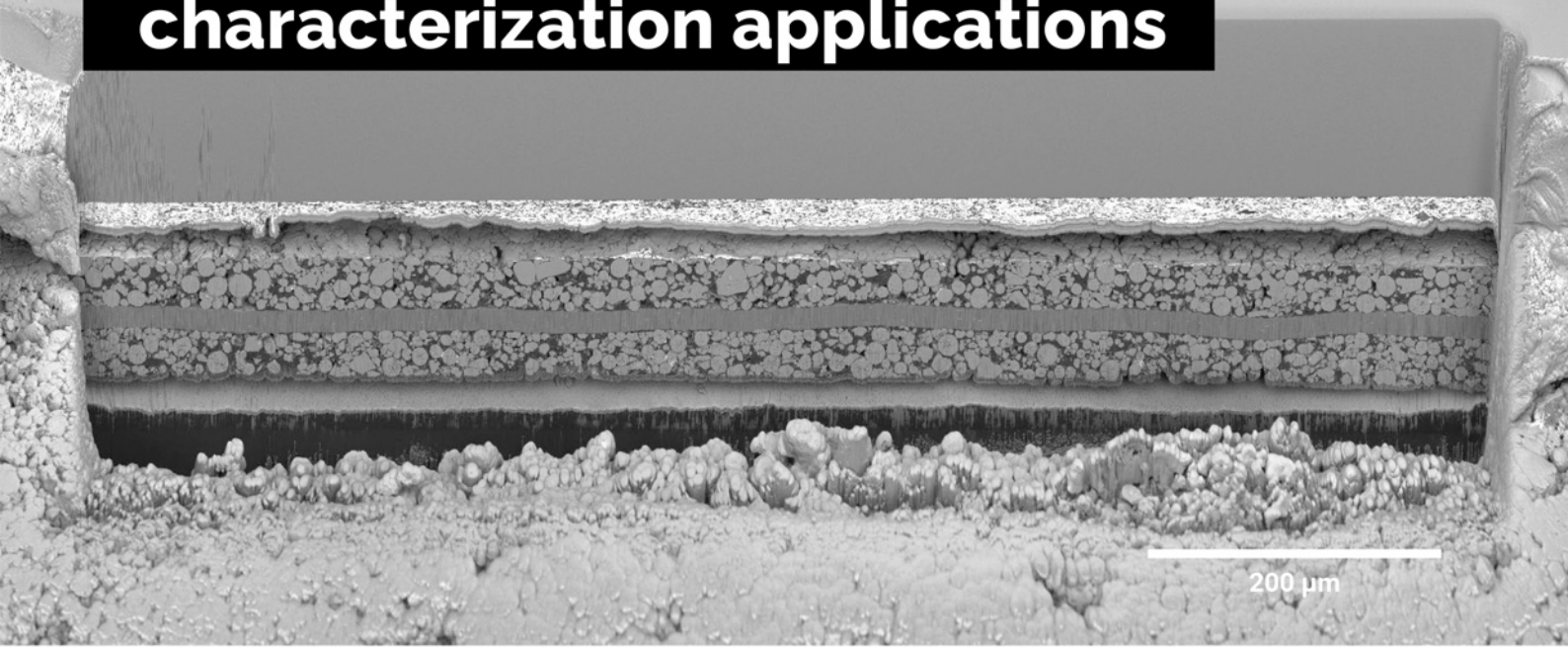


# A unique combination of Plasma FIB and field-free UHR SEM for the widest range of multiscale materials characterization applications



1 mm cross-section through a Li-ion battery electrode

## TESCAN AMBER X

- ✓ High throughput, large area FIB milling up to 1 mm
- ✓ Ga-free microsample preparation
- ✓ Ultra-high resolution, field-free FE-SEM imaging and analysis
- ✓ In-column SE and BSE detection
- ✓ Spot optimization for high-throughput, multi-modal FIB-SEM tomography
- ✓ Superior field of view for easy navigation
- ✓ Essence™ easy-to-use, modular graphical user interface



For more information visit

[www.tescan.com](http://www.tescan.com)

# Modeling and Simulation of Flow Batteries

Oladapo Christopher Esan, Xingyi Shi, Zhefei Pan, Xiaoyu Huo, Liang An,\* and T.S. Zhao\*

**Flow batteries have received extensive recognition for large-scale energy storage such as connection to the electricity grid, due to their intriguing features and advantages including their simple structure and principles, long operation life, fast response, and inbuilt safety. Market penetration of this technology, however, is still hindered by some critical issues such as electroactive species crossover and its corresponding capacity loss, undesirable side reactions, scale-up and optimization of structural geometries at different scales, and battery operating conditions. Overcoming these remaining challenges requires a comprehensive understanding of the interrelated structural design parameters and the multivariable operations within the battery system. Numerical modeling and simulation are effective tools not only for gaining an understanding of the underlying mechanisms at different spatial and time scales of flow batteries but also for cost-effective optimization of reaction interfaces, battery components, and the entire system. Here, the research and development progress in modeling and simulation of flow batteries is presented. In addition to the most studied all-vanadium redox flow batteries, the modelling and simulation efforts made for other types of flow battery are also discussed. Finally, perspectives for future directions on model development for flow batteries, particularly for the ones with limited model-based studies are highlighted.**

## 1. Introduction

The carbon footprint coupled with the inefficiency of conventional energy sources has spurred the necessity to largely pursue clean and sustainable energy alternatives to match up with the numerous energy-demanding lifestyles of the rising global population.<sup>[1]</sup> As a result, joint efforts from different technologies has led to the proliferation of harnessing renewable power sources, particularly solar and wind, for competitive and

O. C. Esan, X. Shi, Z. Pan, X. Huo, Dr. L. An  
Department of Mechanical Engineering  
The Hong Kong Polytechnic University  
Hung Hom, Kowloon, Hong Kong SAR 999077, China  
E-mail: liang.an@polyu.edu.hk

Prof. T.S. Zhao  
Department of Mechanical and Aerospace Engineering  
The Hong Kong University of Science and Technology  
Clear Water Bay, Kowloon, Hong Kong SAR 999077, China  
E-mail: metzhao@ust.hk

 The ORCID identification number(s) for the author(s) of this article can be found under <https://doi.org/10.1002/aenm.202000758>.

DOI: 10.1002/aenm.202000758

sustainable electricity generation, as well as gradual adoption in the transportation sector for electric vehicles.<sup>[1a,d,2]</sup> However, the sporadic nature of the renewable sources with time and climatic conditions in generating energy has significantly heightened the needs for electrical energy storage devices. This is to guarantee the effective utilization of these power sources and provide flexible energy infrastructures for reliable and continual power supply.<sup>[3]</sup> To productively achieve this target, there is a need to deploy highly efficient energy storage systems with long-term stability and safety at an affordable capital cost.

Over the years, various types of electrochemical energy storage devices have been developed, including pumped hydroelectric, compressed air, hydrogen storage, super-capacitors, and solid-state batteries.<sup>[4]</sup> However, none of these systems satisfactorily possesses the essential features for sustainable and large-scale applications. For example, the pumped hydroelectric and compressed air energy storage devices are constrained by site-specification requirements and transmis-

sion cost.<sup>[5]</sup> Low energy density and high self-discharge rate are the major drawbacks of super-capacitors.<sup>[6]</sup> Hydrogen storage systems are limited by their low energy efficiency, short lifetime, and safety issues.<sup>[7]</sup> Solid-state batteries such as lithium-ion batteries are also constrained by high cost and safety issues especially when developed on the large scale.<sup>[8]</sup> To eliminate most of these shortcomings, battery technology was revolutionized through the advent of redox flow batteries (RFBs), which is basically a rechargeable flow cell concept.<sup>[9]</sup> RFBs are electrochemical energy storage systems that reversibly orchestrates the transformation between electrical and chemical energy through electrochemical reactions between two redox couples; where ferric/ferrous and chromic/chromous ions are the first redox couples employed to successfully demonstrate the operations of a classic rechargeable redox flow cell.<sup>[10]</sup>

The structural design of a flow battery essentially comprises two independent storage tanks holding separated electrolyte solutions (anolyte and catholyte), and two porous electrodes separated by a membrane. During the battery operation, the electrolytes flow through the pipes into the porous electrode surface for electrochemical reactions, and also flow back into the tanks to complete the cycle.<sup>[11]</sup> Unlike conventional batteries, where energy is usually stored in the porous electrodes,

RFBs chemically store electrical charges in the liquid electrolytes. This leads to the distinct modular separation of the power rating and energy capacity components of the battery, thereby allowing smooth and optimum scaling of two independent components. While the power rating is a function of the number of cells present in the stack together with the geometric area of the porous electrodes; the volume of electrolytes and the concentration of electroactive species determine the energy capacity of RFBs.<sup>[12]</sup> This design approach provides the opportunities for flexible and relatively low-cost electrochemical energy storage devices. For instance, the smooth scalability of the electrolyte tanks for storage capacity render a distinctive solution toward grid-scale energy storage. Other intriguing characteristics and advantages of RFBs over other available energy storage technologies are well documented and discussed in refs. [12b, 13]. RFBs have therefore been extensively developed and shown to be the most promising candidate for wide range of energy storage applications notably for boosting the reliability of electricity grid infrastructure.<sup>[14]</sup>

Due to the advantageous design flexibility of the flow battery system, many redox couples have been proposed for battery chemistries. Some of the common design types include the all-vanadium,<sup>[15]</sup> iron-chromium,<sup>[16]</sup> soluble lead-acid,<sup>[17]</sup> hydrogen-bromine,<sup>[18]</sup> zinc-bromine,<sup>[19]</sup> organic,<sup>[20]</sup> and semisolid flow batteries.<sup>[21]</sup> Till date, RFBs are increasingly attracting attentions for advancements, consequently stimulating innovations for more improved redox chemistries toward addressing the problems of the growing electricity storage demands as well as managing the renewable-electricity grid. Of all the flow batteries, however, the all-vanadium redox flow battery (VRFB) is the most developed and studied option for large-scale energy storage due to the presence of the same element, vanadium, in the electrolyte solutions. Cross-contamination of electrolyte solution is thus eliminated. In addition, the VRFB is environmentally friendly as it does not release toxic gases or flammable substances. Long operating life cycle, even above 20 000 cycles, is another significant advantage of VRFB. The electrolyte solutions, both catholyte and anolyte, can be effortlessly recycled during the battery operations.<sup>[22]</sup> With these and other salient features, the VRFB has attained the industrialization stage through its various successful installations and remarkable project performance across the globe.<sup>[23]</sup>

In addition to the VRFBs, other types of flow battery should be given more research and development attention in order to favorably compete with, and supplement VRFB for large-scale applications. The soluble lead-acid flow battery (SLFB) is a promising and an economical electrochemical energy storage system with simple structural design housing a single electrolyte tank for both electrode reactions to eliminate issues of electrolyte crossover, hence no need for membrane.<sup>[24]</sup> With these attributes, many of the limitations of static lead-acid batteries are tackled. Semisolid flow batteries also boast of flexible yet low cost structural design for large-scale energy storage with high energy density more than many aqueous flow batteries.<sup>[21]</sup> The Organic flow batteries are also suitable energy storage options which eliminate solubility issues common in metal-based flow batteries, and therefore achieve increase in energy density with the use of low-cost organic molecules or compounds.<sup>[25]</sup> The high energy density, stability in aqueous solutions and low-cost advantages render zinc-based flow batteries,



**Oladapo Christopher Esan** received his B.S. degree from the Federal University of Technology Akure, Nigeria in 2015 and M.Sc. degree in 2018 from Cranfield University, UK. He is currently pursuing his Ph.D. degree under the supervision of Dr. Liang An at The Hong Kong Polytechnic University. His current research is focused on the modeling and simulation of redox flow batteries.



**Liang An** received his B.S. degree from Harbin Institute of Technology in 2008 and Ph.D. degree from The Hong Kong University of Science and Technology in 2012. He is currently an Assistant Professor of Mechanical Engineering at The Hong Kong Polytechnic University. His research interests include advanced energy conversion and storage technologies, such as fuel cells and batteries.



**T.S. Zhao** is currently Cheong Ying Chan Professor of Engineering and Environment, the Chair Professor of Mechanical and Aerospace Engineering, and the Director of the HKUST Energy Institute. Professor Zhao combines his expertise in research and technological innovation with a commitment to creating clean energy production and storage devices for a sustainable future. His research interests include fuel cells, advanced batteries, multi-scale multiphase heat/mass transport with electrochemical reactions, and computational modeling.

including zinc nickel and zinc bromine, well suitable for stationary energy storage applications.<sup>[26]</sup> Hydrogen bromine flow batteries are another promising candidate for large-scale storage applications due to their fast rate of redox and kinetic reactions, good reversibility of the electrode reactions, high energy capacity, abundance of reactants materials, and low cost.<sup>[18]</sup> The abundance of sodium and air, in addition to other advantages, also offer sodium-air flow battery a great prospect for an inexpensive application in electrochemical energy storage devices.<sup>[27]</sup> The vanadium–cerium flow battery system which

combines the advantages of Vanadium and Cerium as suitable elements for energy storage applications is another compelling energy-storage option. The comparatively large gaps between the electrode potentials of both vanadium and cerium in the aqueous solution also suggests their combination as a promising system for flow battery.<sup>[28]</sup> However, some of the common challenges obstructing the widespread development of flow battery technologies include capacity deterioration, materials degradation, undesirable effects of side reactions, thermal issues, relatively low energy density, high financial cost, and scalability.<sup>[23a,29]</sup> These lingering challenges need to be thoroughly addressed for more practical applications of these energy storage systems. It is therefore of paramount importance to develop more experimental and modeling approaches to gain broad insight into the operational mechanisms of all these flow battery systems in order to achieve rational design for structural and capacity enhancement as well as widespread applications.

To address these critical issues, several experimental studies have been carried out; however, experimental investigations can hardly quantify most of the multicomponent parameters and processes that govern the flow battery operation.<sup>[29b,30]</sup> For instance, it is difficult to investigate the various complicated and interconnected transport processes in electrodes and membranes by experiments. Considering the financial and time implications, addressing most of these barriers through experimental studies may not be comprehensive enough. To unravel these limiting factors, battery modeling and simulation are essential. Modeling, as a cost-effective tool, provides adequate framework for comprehensive understanding of the underlying theoretical and working principle of complex systems. In other words, the complex phenomena of the multivariable cell components and the entire battery system can not only be explored but also be optimized through modeling. Battery modeling is also important for monitoring and controlling procedures in revealing the design parameters that are more crucial for performance enhancement.<sup>[31]</sup> In addition, numerical simulations provide computational platforms not only to achieve effective modeling results, but to accurately capture and predict the real application behavior of the system, which can always be validated with experimental data. Modeling and simulation have also been severally employed to evaluate and optimize the components and operational variables in fuel cells,<sup>[32]</sup> and lithium batteries<sup>[33]</sup> toward improving their overall performance.

The modeling techniques of flow batteries have experienced different transitions starting from empirical modeling to equivalent circuit modeling to lumped parameter models and to macroscopic continuum modeling method which is commonly applied in battery modeling. The modeling approach to be used in any study depends on the number and nature of operation parameters to be simulated. In some studies, continuum model has also been combined with an equivalent circuit model to evaluate some key parameters in flow batteries.<sup>[34]</sup> The equivalent circuit models use electrical components to investigate electrical behavior, while macroscopic continuum modeling approach typically adopts volume-averaged and homogenized properties and structures for electrodes and membrane. The macroscopic continuum method also follows some set of conservation or governing equations such as continuity equation, mass/species, charge, momentum, and energy conservation equations to resolve transport and electrode

reactions in battery systems.<sup>[23a,31,35]</sup> Due to the complex mechanisms in the operation of flow batteries, some assumptions and simplifications which could be in form of modeling domain, study state and isothermal condition are usually considered while developing battery models. In this regard, the complexity of the modeling framework is simplified while criteria that are of less importance to the study are ignored. Moreover, the introduction and continuous improvement of modeling techniques has also facilitated the development of more in-depth and reliable battery model approach. For example, molecular dynamics (MD) and density functional theory (DFT) are being used to unravel the atomic and molecular properties and structures of materials. Lattice Boltzmann method (LBM) is commonly used modeling for pore-scale studies in flow batteries. Multiphysics software, supercomputers and high-resolution X-ray computing systems are also employed in modeling and simulation processes, even at different length scales including multiscale, which have all reduced computational time and cost.<sup>[35–36]</sup>

Modeling and simulation of different flow battery chemistries have therefore increasingly attracted intensive research attention in the last decade. However, few review papers pertinent to modeling of flow batteries have been published, with a good number of them majorly focusing on all-vanadium redox flow batteries.<sup>[23a,29b,37]</sup> When there were still few research efforts on the modeling of flow batteries, Pan et al.<sup>[37]</sup> summarized the model-based studies on VRFBs. Zheng et al.<sup>[23a]</sup> later discussed the scale-level classifications for VRFBs model development (macro, micro/pore, and molecular/atomic), and modeling application levels (market, stack/system, cell, and material). Xu and Zhao<sup>[29b]</sup> discussed the fundamental transport properties and processes for porous medium with more reference to VRFBs. The research and development progress on the operation characteristics, performance prediction and improvement on other flow battery systems via modeling and simulation tools are therefore not covered. In a comprehensive review of redox flow batteries, Weber et al.<sup>[12b]</sup> incorporated a brief overview of the available modeling efforts on selected flow batteries while discussing the physical processes and the various components of redox flow batteries. It is worth to note that after these earlier reviews, several numerical investigations, which play significant roles in improving battery designs and providing insights into the operations and performance of more flow battery chemistries other than VRFBs, have been successfully performed. Other reviews on flow batteries<sup>[11c,38]</sup> randomly mentioned the simulation results obtained from the modeling frameworks of some selected flow batteries. Till date, there is no existing review article that entirely covers the modeling and simulation of these flow batteries. Hence, exploring the various modeling frameworks and the simulation outcomes of more flow batteries becomes necessary for knowledge update and useful direction toward further investigations and improvements of flow battery technologies.

In this article, we extend the modeling and simulation review of flow batteries beyond the all-vanadium, to include soluble lead-acid, semisolid, organic, zinc-nickel, zinc-bromine, hydrogen-bromine, sodium-air, and vanadium-cerium flow batteries. A comprehensive review on the recent research and development progress on the modeling and simulation of all these flow batteries are discussed while taking cognizance

of their length scales. We first discussed the key material components and operation parameters that markedly influence the power density and energy efficiency of flow batteries with much attention to the broadly studied VRFB. A detailed state-of-the-art advancement in the optimization of the operating conditions and parameter designs of all the aforementioned flow batteries through modeling and simulation are summarized and discussed. The architectural designs, physicochemical processes, working strategies, as well as the limitations of these flow batteries are also presented. Finally, new directions in the future modeling and simulation of these flow batteries are highlighted.

## 2. Key Components and Design/Operation Parameters

The performance and reliability of flow batteries are generally governed by key material components and operation variables. This buttresses the need for rational design of efficient materials and optimization of the broad range of operation variables for improved power and energy density, component durability, and energy efficiency of the whole battery system. Thus, this section briefly summarizes the functions and desired properties of key components and design parameters that are commonly investigated for the optimization of flow batteries structural design, by considering the most studied VRFB.

### 2.1. Electrode

Flow battery electrodes are generally porous media ingrained with interlinked pores primarily for the inflow of electroactive species. Electrodes play the crucial role of conversion sites in the operation of flow batteries, even though the electrochemical redox reactions usually take place on the electrode surface, the electrodes are usually not subjected to physicochemical changes during the battery operations. The actual site that is catalytically active for the electrode redox reaction is the interface between the porous electrode and electrolyte known as the active surface area. The design and structure of electrodes not only influence the rate of electrochemical reactions, but also affect the transport mechanisms of mass and charge (ions and electrons).<sup>[39]</sup> Some of the expected requirements of flow battery electrodes to obtain high power density and energy efficiency include large active surface area for electrochemical reactions to minimize the activation polarization, excellent electronic conductivity to minimize the ohmic polarization, excellent electrolyte permeability to enhance mass-transfer rate and reduce the concentration polarization, high wettability with aqueous electrolytes, good chemical and corrosion resistance, good mechanical strength, and low cost.<sup>[39a,40]</sup> Physical features, such as tortuosity and porosity, which provide channels for fast and smooth transport of electroactive species, are another significant property of electrodes which are also essential for porous electrode modeling. A high ratio of electrode length to its thickness is also advisable for lowering concentration polarization.<sup>[39d]</sup> The common electrode materials suitable for flow batteries are various forms of carbon such as carbon cloth, carbon felt, carbon black, and graphite felt.<sup>[39a,41]</sup> While porous carbon electrode materials

are commonly used in VRFBs, the soluble lead acid flow batteries typically employ nonporous/planar electrodes. In order to improve the reactivity properties and general performance of electrode materials, several structural/surface modifications and treatments, have been experimentally demonstrated.<sup>[42]</sup> In addition, a number of numerical studies many of which are pore-scale models have been conducted to further probe into the microstructural information and properties,<sup>[43]</sup> transport processes,<sup>[36b,44]</sup> and compression effects<sup>[45]</sup> of porous electrodes. In later sections, macro-scale models which assumed homogenized materials and porous electrode theory, and the pore-scale models on porous electrodes in VRFBs will be discussed.

### 2.2. Membrane/Separator

The membrane is another prominent component of flow battery, which plays important roles in the cycling performance of the battery system. However, some flow battery designs, such as soluble lead acid flow battery and other hybrid/single flow batteries, are without membrane.<sup>[46]</sup> The membrane essentially separates two electrolyte compartments (negative and positive sides), thereby obviating crisscrossing of electroactive species. In addition, the membrane is generally resistant to the passage of electrons but allows the transport of charge-carrier species between both half-cells to complete the electrical circuit while disallowing short circuit. Membrane, therefore, influences the voltage and coulombic efficiencies of flow batteries.<sup>[40a]</sup> Some of the vital properties of a high-performance membrane include excellent ionic selectivity and conductivity, low ohmic resistance, excellent chemical and thermal stability, moderate water uptake, and low capital cost.<sup>[47]</sup> Poor properties and degradation of membrane augments the capacity decay in flow batteries. The major categories of membrane mostly employed in the operation of flow batteries are the ion exchange membranes (cationic and anionic) and sometimes porous separators as a less expensive alternative.<sup>[48]</sup> Recent reviews have outlined various classes of membranes for rechargeable flow batteries including VFB.<sup>[47a,b,49]</sup> Nafion series ion exchange membrane has been widely employed, despite its high cost, by VRFB developers due to its excellent chemical stability and proton conductivity. Nevertheless, numerous experimental research efforts in membrane science and engineering have been focused on novel membranes design and development, modifications and optimizations of existing membranes for better performance including lower vanadium ions crossover, water crossover, and ohmic resistance, even at low cost.<sup>[50]</sup> Numerical investigations on transport phenomena across membrane in VRFBs are discussed in another section.

### 2.3. Electrolyte

The electrolyte is one of the most significant components of the battery system, which notably influences the electrochemical performance. Commonly, the corrosive solution that containing the dissolved electroactive species circulates through the battery system. As mentioned earlier, the volume and concentration of the electrolyte determines the energy capacity of the battery.

Flow battery electrolyte can either be in aqueous or nonaqueous state, however, the former is mostly used in VRFBs due to low ionic conductivity of the latter.<sup>[3c,9c,12b]</sup> Regarding VRFBs, the electrolyte in positive and negative compartments are vanadium redox couples  $V^{2+}/V^{3+}$  and  $VO_2^+/VO_2^{2+}$ , respectively, combined with a supporting electrolyte, commonly sulfuric acid. Various preparation and processing methods of these electrolytes for VRFB applications are discussed in refs. [22b,51]. Electrolyte composition, concentration, solubility, thermal stability, conductivity, viscosity, and diffusivity coefficient are the key properties to pay attention to in selecting and preparing electrolytes for flow battery utilization. For example, Zhao et al.<sup>[52]</sup> reported that an increase in the concentration of a supporting electrolyte ( $H_2SO_4$ ) from about 2 to roughly 4 M in a VRFB would consequently lead to an increase in electrolyte conductivity and viscosity. These properties not only influence the performance and cycling durability of the battery system, but also significantly contribute to the cost of the battery. Due to the crucial roles of electrolytes on flow-cell characteristics, many research efforts have been made to optimize and improve their electrochemical properties and performance for high vanadium ions solubility and stability through the removal of impurities, usage of additives, introduction of mixed electrolytes, addition of precipitation inhibitors, and the development of novel electrolytes.<sup>[53]</sup> More importantly, a mathematical model, based on experimental measurements has also been developed to estimate and improve the metastability of catholyte in VRFBs.<sup>[54]</sup> Thermal stability improvement, together with solubility of catholyte is a critical need for boosting energy density and advancing the commercialization of the flow battery. Hence, modeling and simulations addressing the underlying physical and chemical properties of electroactive species in flow batteries, especially at molecular level, should be carried out.

#### 2.4. Membrane–Electrolyte Interface

During the operation of VRFBs, the flow-cell membrane is always in direct contact with the flowing electrolyte around the porous electrodes; hence, membrane–electrolyte (M–E) interface is the resulting boundary between the electrolyte and membrane. It has been described as a narrow boundary known for steep ion concentration jump. Donnan effect, a vital consideration for accurate modeling of ions transport through the pores of ion-exchange membranes, occurs at the M–E interface.<sup>[55]</sup> Electroactive species and current flux were pointed out to be continuous at this interfacial region, but due to the permselective nature of ion-exchange membranes, ion concentration, and potential are discontinuous at the interface.<sup>[56]</sup> Despite the pivotal roles of this interface on transport processes and ion selectivity processes in membranes, it was not considered in early models for VRFBs. However, this interfacial region was later incorporated in a modeling framework for VRFB to account for concentration and potential discontinuities.<sup>[56b]</sup> Detailed study on Donnan effect and its roles at the M–E interface was later reported and included in some other models.<sup>[55,57]</sup> The consideration of this crucial interface in the numerical investigation of the various transport processes in flow battery systems is of paramount importance.

#### 2.5. Flow Field Designs

Flow field is an integral design of fluidic routes over the electrode surface to regulate the circulation and utilization of reacting species, as well as minimize pressure loss. In other words, the essential functions of flow fields is to effectively distribute electrolytes over the surface of the porous electrodes; supply/withdraw electric current to and from the external circuit; provide structural and mechanical support for the electrode; and enhance proper heat management of the flow cell.<sup>[58]</sup> Flow-through and flow-by designs are two major designs that have been widely used in flow batteries. The flow-through design is without channels in its bipolar plates and therefore facilitates forced convective flow of electrolyte through the porous electrode. Unlike the flow-by design, the flow of electrolyte via the flow-through design is perpendicular to the direction of current flow in fuel cells and many flow batteries.<sup>[39d]</sup> Although, the flow-through design requires thick electrodes to suppress pressure loss, mass transport of electroactive species has been reported to be extremely good.<sup>[39b]</sup> The flow-by design is commonly featured in thin electrodes, and now exists in different patterns including serpentine, parallel, spiral, and interdigitated designs, all of which are also applicable in fuel cells<sup>[59]</sup> Apart from these flow field designs, new configurations for flow batteries have been recently developed, these include corrugated flow field,<sup>[11b,60]</sup> aspect ratio and equal path length flow fields,<sup>[61]</sup> hierarchical interdigitated,<sup>[62]</sup> trapezoid flow field,<sup>[63]</sup> and tapered miniaturized-interdigitated flow field.<sup>[64]</sup> The selection of appropriate flow field design has been reported to yield a peak power density,<sup>[65]</sup> a high round-trip efficiency,<sup>[58b]</sup> a small ohmic loss,<sup>[39b]</sup> and a low concentration overpotential.<sup>[58c]</sup> In addition to the channel patterns, the dimension and geometry should be carefully selected and designed. Since there are various flow field designs, the choice of suitable designs and their optimization is therefore paramount to flow battery performance as different flow field structures exhibit different operation characteristics.

#### 2.6. Flow Rate

Electrolyte flow rate basically refers to the quantity of fluid passing through a specific channel area of the flow system in a specified period. Flow rate serves as a means to regulate the distribution of electrolyte composition and concentration, which largely influences the energy density as well as the optimal operation of battery.<sup>[53a]</sup> Since the electrolyte solution carries the electroactive materials, the magnitude of electrolyte flow therefore influences the flow cell performance. During discharge process, a high flow rate was reported to increase cell voltage as well as raises the depth of discharge.<sup>[66]</sup> In addition, the flow rate is also crucial in determining and controlling the electrolyte temperature within desirable limits during so as to preclude the precipitation of vanadium ions.<sup>[67]</sup> Moreover, the magnitude of the flow rate influences shunt current loss, pressure drop, and concentration overpotential, which all contribute to the total system efficiency.<sup>[68]</sup> For instance, in VRFBs, a high flow rate with its corresponding increase in mass transport has been reported to yield a capacity increase but at the same

time degrade charge efficiency due to the high pump consumption. A low electrolyte flow rate, on the other hand, demands a low pump power but results in early voltage cut-off due to the increase in the concentration overpotential.<sup>[67a,69]</sup> In these cases, modeling and simulation for trade-off between high and low flow rates, and other influential parameters is required so as to achieve optimal operational flow rate in flow batteries.

## 2.7. Operating Temperature

This describes the thermal range, behavior and management of flow batteries. A temperature range within 10–40 °C has been reported for operating VRFBs with a corresponding optimal vanadium-ion concentration usually between 1.6 and 2.4 M.<sup>[51f,70]</sup> Such a broad temperature range is to ensure the optimal balance with the differences in the solubility and stability range of vanadium ions. For instance, the solubilities of V<sup>2+</sup>, V<sup>3+</sup>, and V<sup>4+</sup> increase with the temperature, and thus three vanadium ions perform well at high temperatures but poorly at low temperatures. It is not the case with V<sup>5+</sup>, however, as it undergoes precipitation at high temperatures.<sup>[51f]</sup> As such, operating the battery outside this range can significantly alter the physical properties and chemical stability of electrolytes, as well as the general safety of the battery system. Furthermore, the operating temperature range contributes to mass transport of electroactive species and different side reactions occurring during the battery operation.<sup>[71]</sup> These underline the importance of considering nonisothermal condition while designing and optimizing flow batteries. Also, the thermal behavior of flow batteries notably changes with the ambient or environmental temperature of the geographical location of the battery operation, and thus has influence on the battery performance.<sup>[72]</sup> This particular aspect is sometimes overlooked during the battery design. In more details, the effects of a number of battery design parameters including number of cell, electrolyte tank dimension have been numerically examined on the thermal behavior of VRFBs.<sup>[72b]</sup> The collective effects of the ambient temperature, electrolyte temperature and cell-stack temperature on the performance of flow batteries should also be considered in future research works.

## 3. All-Vanadium Redox Flow Batteries

The most studied and technologically developed flow battery technology is the all-vanadium redox flow battery (VRFB) due to its huge potential for large-scale energy applications. The quest for a flow battery system that uses a single electroactive element, to effectively avoid the undesired cross-mixing of electrolytes experienced in early flow cells, led to the development of VRFBs in 1985 at the University of New South Wales, Australia.<sup>[15a,73]</sup> The battery system capitalizes on four valence states of vanadium to form two active redox couples whose electrochemical reactions are known for a very low environmental impact as toxic emissions and explosive gases are not produced. Other than this, the reliability of vanadium metal to be charged and discharged for lengthy period of cycles renders the element suitable for large energy storage technologies<sup>[22a,74]</sup>

Another important point about vanadium is that the potential of the electroactive species (V<sup>2+</sup>/V<sup>3+</sup>) utilized in the negative electrolyte is much higher than the potential value at which the evolution of hydrogen takes place on carbon-material electrodes, which is vital for maintaining the electrolyte stability.<sup>[22a]</sup> Moreover, VRFB has been found to be most attractive, coupled with its various unique advantages of high round-trip efficiency, excellent electrolyte utilization, fast response, long cycle life exceeding 20 000 cycles, and huge potentials for large energy storage capacity and power output.<sup>[75]</sup> However, the major constraint of VRFB when compared to other battery systems is the relatively low energy density, corresponding to the finite solubility of vanadium ions. Many a time, this is not really a drawback particularly for stationary utilizations.

### 3.1. Working Principle

The configuration of a VRFB simply consists of two sides—positive and negative half-cells, interconnected to an external circuit, an electrically conductive pathway. Each side comprises a porous electrode and an electrolyte tank, and two electrodes are usually separated by an ion exchange membrane as shown in **Figure 1**. However, a VRFB design of four storage tanks, with two electrolyte tanks on both sides of the cell, was recently introduced.<sup>[76]</sup> Practical VRFB typically constitute tens or hundreds of cells connected in series to form cell-stack capable of providing required power output for a specific application. All-vanadium redox flow batteries (VRFBs) employ two tanks to store vanadium ions as V<sup>2+</sup>/V<sup>3+</sup> redox couple as the negative electrolyte while using VO<sup>2+</sup>/VO<sub>2</sub><sup>+</sup> in the positive electrolyte by dissolving both redox couples in dilute sulfuric acid (H<sub>2</sub>SO<sub>4</sub>).<sup>[15a,73,77]</sup> The electrolytes are separately fed into the battery cell and then flow back into the tanks in order to be recirculated. Without a change in the flowing electrolyte phase, reversible electrochemical oxidation and reduction of the electroactive species take place, thereby converting chemical energy to electrical energy (discharge process) and reversibly storing electrical energy as chemical (charging process).

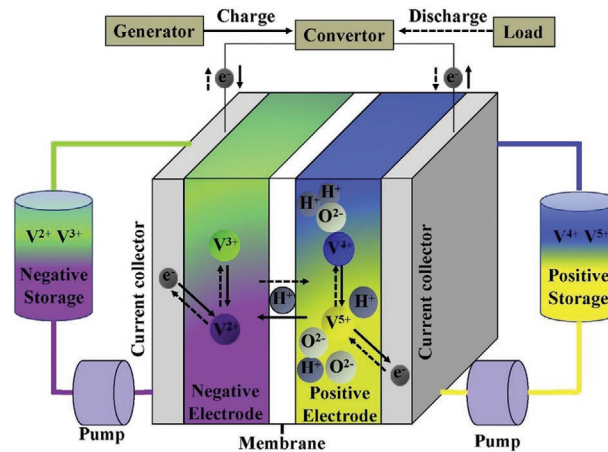
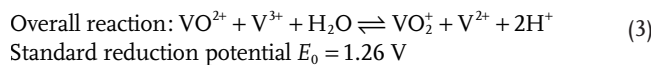
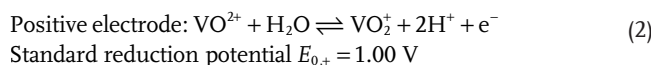
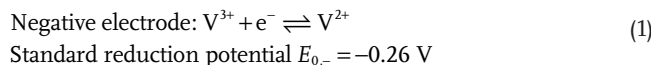


**Figure 1.** Schematic of an all-vanadium redox flow battery system. Reproduced with permission.<sup>[95b]</sup> Copyright 2019, Elsevier.

During the discharge process, particularly at molecular level,  $V^{2+}$  and  $VO_2^+$  are released into the electrochemical flow cell from the negative and positive electrolyte tanks, respectively. At the negative electrode,  $V^{2+}$  is oxidized to  $V^{3+}$ , thereby losing an electron, which carries the electrical energy and flows through the external circuit to the positive electrode. At the positive electrode,  $VO_2^+$  is reduced to  $VO^{2+}$  by absorbing the incoming electron. During this reduction–oxidation process, protons  $H^+$  are migrated through the ion exchange membrane from the negative side to the positive in order to maintain the overall charge balance. Consequently, water is produced as a by-product in the positive electrode to balance the stoichiometry.<sup>[22b,78]</sup>  $V^{3+}$  and  $VO^{2+}$  eventually leave the negative and positive half-cells, respectively, in discharged states. On the other hand, charging process is simply the opposite trend of the discharge process. In this case,  $V^{2+}$  and  $VO_2^+$  leave the negative and positive half-cell, respectively, in charged state. Comparatively, the reactions and charge transfer mechanisms at the positive electrode is slower and more complicated, respectively, than those at the negative electrode. This is because only electron transfer takes place in the  $V^{2+}/V^{3+}$  conversion reaction while oxygen transfer in addition to electron transfer occurring in the  $VO^{2+}/VO_2^+$  conversion reaction.<sup>[39a,79]</sup> The redox reactions occurring at the electrode surface in each half-cell, including the overall reaction are represented as follows<sup>[23b,38b]</sup>



### 3.2. Modeling of All-Vanadium Redox Flow Batteries

As mentioned earlier, VRFB has received the most model-based studies, particularly with the recent introduction of various computational and simulation software packages to facilitate useful optimization designs and development of the battery and its various components, even at different length scales. While many of VRFB models rely on macroscopic continuum modeling approach, modeling studies based on other scale levels are clearly stated in the discussion.

Li and Hikihara<sup>[80]</sup> first reported a modeling framework on a VRFB in 2008, where they established a 0D model based on physical processes and chemical kinetic reactions to investigate the pump power and electrochemical performance of the battery. As such, the spatial representation, operation characteristics, and overall performance of the battery system were not properly demonstrated, primarily because many parameters including vanadium-ion concentrations at both electrodes, proton concentration, membrane properties, and flow rate were all taken as constant in the lumped parameter model. To better predict the battery performance, a 2D dynamic model

of a single-cell VRFB, validated against experimental results, was developed by Shah et al.<sup>[81]</sup> The macroscopic model was employed to analyze the effects of variations in vanadium-ion concentration, electrolyte flow rate, and level of electrode porosity. The model was further extended by the same research team to examine the influence of temperature range and heat loss,<sup>[82]</sup> hydrogen evolution,<sup>[83]</sup> and oxygen evolution<sup>[84]</sup> on the VRFB performance. Based on the model concept by Shah et al.,<sup>[81]</sup> You et al.<sup>[85]</sup> also developed a stationary cell model to demonstrate the effects of state of charge, local mass transfer coefficient, and applied current density on the operation characteristics of VRFBs on macro scale. Few years later, an asymptotically reduced model was proposed to analytically understand the highly coupled fluid dynamics and electrochemical reactions in VRFBs.<sup>[86]</sup> The modeling approach also account for the transportation of ionic species by migration which was neglected in one of the previous models.<sup>[85]</sup> Based on a kilowatt VRFB stack, You et al.<sup>[87]</sup> built a mathematical model to analyze self-discharge mechanism. A detailed mathematical model for controlling and monitoring a single-cell VRFB was also developed.<sup>[88]</sup> Bayanov and Vanhaelst<sup>[89]</sup> also reported the numerical solution for the fluid dynamics and electrochemical model of a VRFB. Afterward, a 3D model and simulation of a negative electrode was developed to provide more details on the significant impacts of electrolyte velocity on the vanadium flow-cell design.<sup>[90]</sup> These pioneer model research works not only lay the groundwork, but also present valuable tools for the increase in exploration of working principles of flow batteries. However, these early studies were established on some assumptions that limit the models from fully capturing the physicochemical processes of VRFBs. First, the ion exchange membrane in all these studies were taken to be permeable only to protons, but every other charged species cannot crossover the membrane. This is not ideally correct, as the membranes are not completely permselective and therefore also permit the transport of vanadium ions and other charges.<sup>[56a]</sup> These critical observations, therefore, demands the development of VRFB models that would incorporate and examine the transport of all charges across the membrane. Another flaw observed in the early VRFB models is the inaccurate estimation of the open circuit voltage (OCV), which brings about the wide difference between cell voltages obtained from simulation and experimental studies.<sup>[91]</sup> The incomplete description of Nernst equation at the positive electrode as shown in Equation (4) and overall system Nernst equation as shown in Equation (5) was identified as one of the major causes, which in turn leads to random fitting of simulated voltage to march up with experimental data<sup>[81,85]</sup>

$$E^+ = E_0^+ + \frac{RT}{F} \ln \left( \frac{c_{V^{5+}}}{c_{V^{4+}}} \right) \quad (4)$$

$$E = E_0 + \frac{RT}{F} \ln \left( \frac{c_{V^{5+}}}{c_{V^{4+}}} \right) \cdot \left( \frac{c_{V^{2+}}}{c_{V^{3+}}} \right) \quad (5)$$

To correct this, the complete form of Nernst equation at the positive side described in Equation (6) was shown by incorporating the proton concentration missing in Equation (5), which truly participates in the redox reaction at the positive electrode<sup>[91]</sup>

$$E^+ = E_0^+ + \frac{RT}{F} \ln \left( \frac{c_{V^{3+}} \cdot (c_{H^+})^2}{c_{V^{4+}}} \right) \quad (6)$$

Another aspect ignored by the former Nernst equation is the Donnan potential that usually exists as a result of proton concentration difference between the two electrolyte sides of the membrane. Thus, the Donnan potential present in a VRFB is given as<sup>[91]</sup>

$$E_m = \frac{RT}{F} \ln \left( \frac{c_{H^+}^+}{c_{H^+}^-} \right) \quad (7)$$

The resulting complete Nernst equation by considering Equations (5) and (6) in addition to the one from negative side was validated against experimental data and the comparisons shows better agreement, indicating a complete representation of the underlying mechanisms and high-accuracy modeling of the flow battery system. This led to the adoption of the complete Nernst equation in subsequent VRFB models<sup>[91]</sup>

$$E = E_0 + \frac{RT}{F} \ln \left( \frac{c_{V^{3+}} \cdot (c_{H^+})^2}{c_{V^{4+}}} \right) \cdot \left( \frac{c_{V^{2+}}}{c_{V^{3+}}} \right) \cdot \left( \frac{c_{H^+}^+}{c_{H^+}^-} \right) \quad (8)$$

where  $E^+$  is the equilibrium potential of the positive electrode,  $E_m$  is the membrane potential, and  $E_0$  is the standard reduction potential.

The common computational model domain, especially at macroscopic continuum scale, for VRFBs indicating the key components of the model framework is schematically shown in **Figure 2**. Most of the physical and chemical phenomena and operation variables explored and optimized through the modeling and simulations of VRFBs are discussed in the following sections.

### 3.2.1. Electrolyte Flow

Electrolyte flow in a VRFB, which is a function of flow rate and flow field structure, is one of the key variables that significantly influence battery cycling operations and efficiencies. Thus,

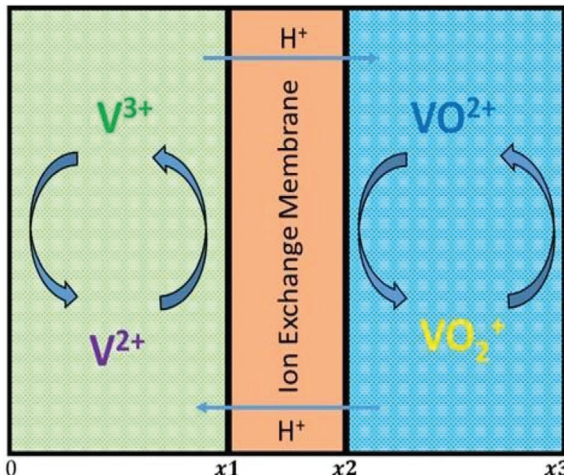


**Figure 2.** 2D modeling domain for all-vanadium redox flow batteries.

effective design and optimization of flow rates and flow field is required for battery improvement.

**Electrolyte Flow Rate:** The rate of electrolyte flow is a crucial factor that significantly influences the efficiencies of VRFBs. For instance, flow rate dictates the pumping energy losses and in turn influences the power output of the battery. The magnitude of electrolyte flow also contributes to the amount of heat transfer and exchange between the storage tanks and the cell-stack.<sup>[67,71b]</sup> While operating the battery at a high flow rate reduces the system efficiency through high pump work; low flow rate increases concentration overpotential resulting from the insufficient supply of electroactive species into the flow-cell. A trade-off between losses due to concentration overpotential and pump energy consumption is thus necessary to attain an optimal flow rate for VRFBs. In an experimental-based study carried out by Ma et al.,<sup>[69a]</sup> an increase in electrolyte flow rate was reported to be beneficial to the battery capacity, however, at the expense of the overall battery system efficiency due to pump loss. They therefore emphasized the critical need for an optimized flow rate. Following the numerical demonstration of the effects of flow rate on the performance of VRFBs,<sup>[66,67b]</sup> more modeling approaches have been applied in optimizing flow rate in the battery system.<sup>[34a,67a,69b,92]</sup> The basis for optimal flow rate is to ensure VRFBs provide maximum battery energy at discharge through improved stack energy and reduced pump work, while requiring the least possible battery energy for charging as a result of reduced stack and pump energy.<sup>[69b,92a]</sup> As such, optimized flow rates concurrently improve the system efficiency while maintaining a high energy capacity.

In a lump parameter model, Xiong et al.<sup>[69b,92a]</sup> reported flow rates around  $90 \text{ cm}^3 \text{ s}^{-1}$  as shown in **Figure 3** as the optimized flow rates through a kilowatt VRFB with a single cell design of 20 cm in length, height of 44 cm, 0.4 cm in thickness with  $875 \text{ cm}^{-1}$  as the electrode specific area. Constant flow rate through the pump power was used at all SOC and current in the model analysis to determine the flow rate with the highest battery efficiency as the optimal flow rate. Elsewhere,  $420 \text{ mL min}^{-1}$  was pointed out as the optimal pump flow rate through pipe of 2 cm diameter, 50 cm in length, and 30 cm height into a six-cell

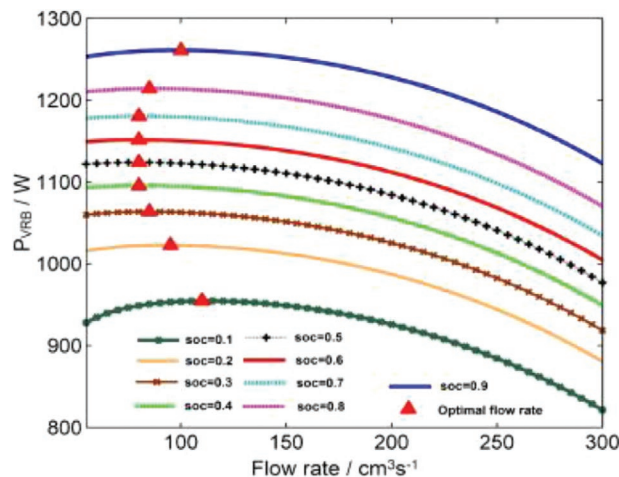


**Figure 3.** Optimal flow rates of the battery during the discharge process when a current load of 60 A was applied. Reproduced with permission.<sup>[69b]</sup> Copyright 2013, Elsevier.

flow battery as  $70 \text{ mL min}^{-1}$  for each cell to achieving maximum discharge-depth as well as high energy and exergy efficiencies.<sup>[66]</sup> While these studies use constant pump flow rates which maintain the same magnitude of electrolyte flow throughout the operating SOCs and currents, it was however pointed out that flow rate should vary with SOC and currents. This is because more supply of species through high flow rates are needed at high and low SOCs to resupply the scanty species. Moreover, as shown in **Figure 4**, cell voltages are almost the same at the middle SOCs at all flow rates, hence reducing the electrolyte flow at such a stage would reduce pump power consumption.<sup>[66,69b]</sup> Other than SOC, species were observed to be consumed more at large currents and therefore requires higher flow rates than that at low currents. It was also pointed out by Kim et al.<sup>[92e]</sup> in their parametric study that regulating the electrolyte flow rate for different operation points (SOC and current density) is an effective strategies to enhance system efficiency. Therefore, a means to control flow rate by eliminating the unnecessary pump loss and in turn improve battery performance is required.

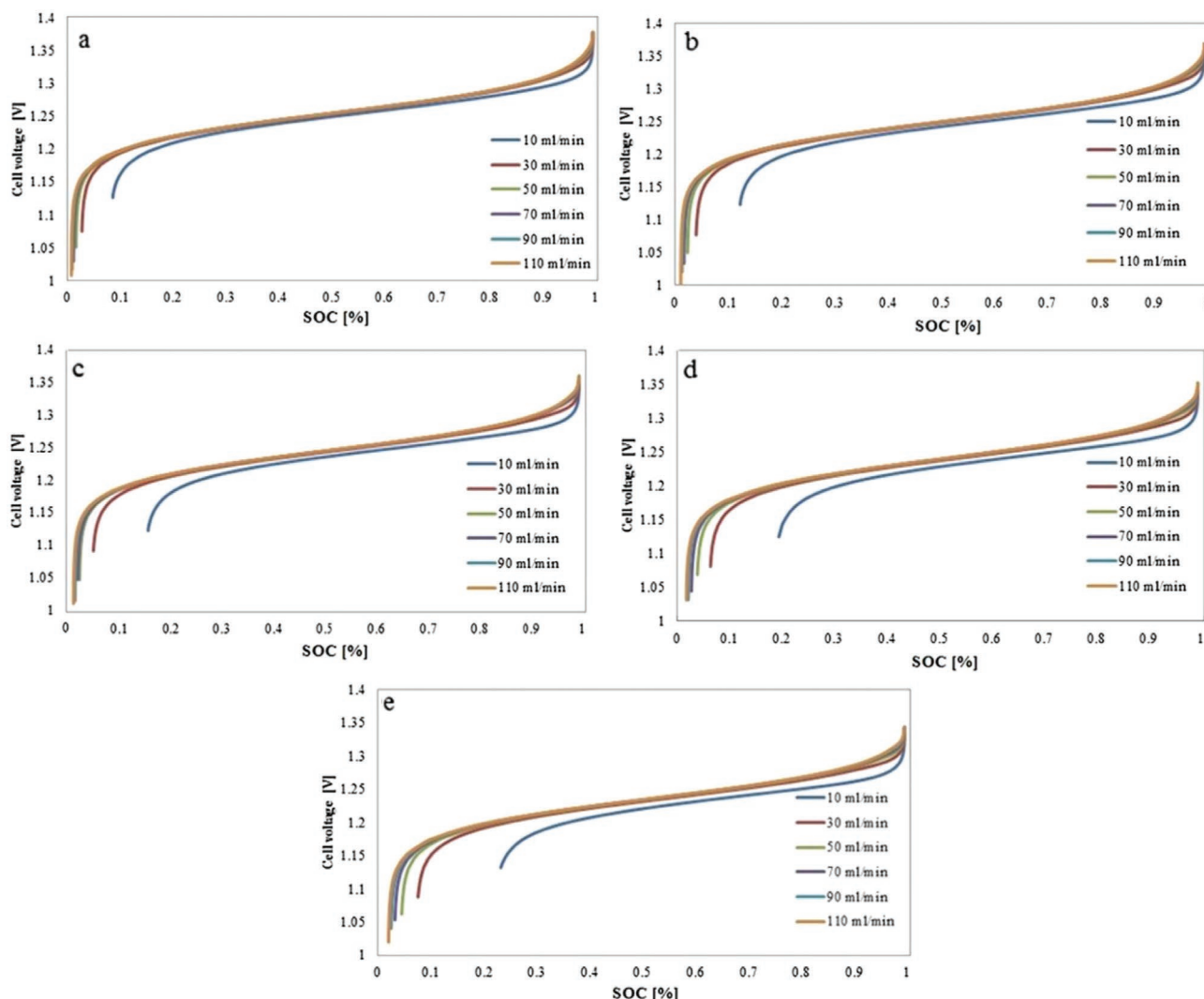


**Figure 4.** Cell voltage profiles indicating cell voltages are almost the same at the middle range SOCs at all flow rates simulated at different applied current densities a)  $40 \text{ mA cm}^{-2}$ , b)  $60 \text{ mA cm}^{-2}$ , c)  $80 \text{ mA cm}^{-2}$ , d)  $100 \text{ mA cm}^{-2}$ , and e)  $120 \text{ mA cm}^{-2}$ . Reproduced with permission.<sup>[66]</sup> Copyright 2015, Elsevier.

In a more detailed study, the use of variable flow rate was introduced while also considering the influence of both concentration overpotential and every component of pressure losses in a VRFB.<sup>[67a]</sup> The variable flow rate regulates the magnitude of flow rate as a function of reactant concentration by modifying the Faraday's law of electrolysis through the incorporation of a flow factor to give

$$Q = \text{Factor} \frac{I}{n \cdot F \cdot c_i} \quad (9)$$

where  $Q$  is the flow rate,  $I$  is the current,  $n$  is the number of electrons involved in the reaction,  $F$  is the Faraday's constant, and  $c_i$  is the concentration of the reactants. The introduction of variable flow rates not only leads to a decrease in the concentration overpotential but also yields better discharge capacity as shown in **Figure 5**, as well as higher efficiencies as shown in **Figure 6** compared to that of constant flow rates. An optimal flow factor between 7 and 8 was also recommended to

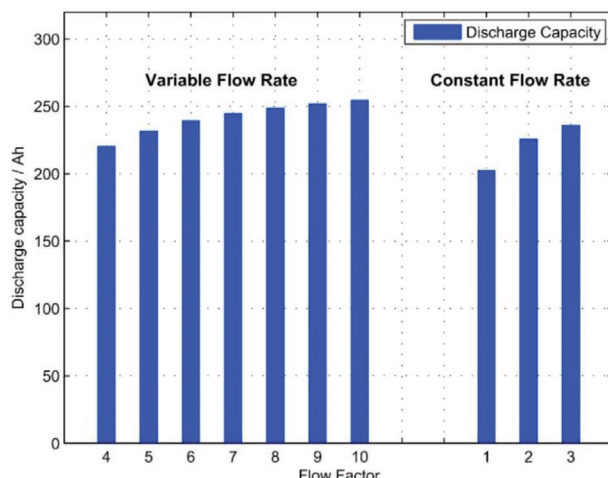


**Figure 5.** Discharge capacity of the VRFB under different electrolyte flow rates. Reproduced with permission.<sup>[67a]</sup> Copyright 2013, Elsevier.

efficiently operate the VRFB. At such optimal flow factors, compromise between the effects of pump losses and concentration overpotential was achieved, which in turn yield high energy efficiency and overall system efficiency. Using the variable flow rate strategy with flow factor, a modeling framework for flow rate optimization by Fu et al.<sup>[92b,f]</sup> considered SOC and current in their equations expressed as

$$\text{For discharge: } Q = \text{Factor} \frac{I}{F \cdot c_i \cdot \text{SOC}} \quad (10\text{a})$$

$$\text{For discharge: } Q = \text{Factor} \frac{I}{F \cdot c_i \cdot (1-\text{SOC})} \quad (10\text{b})$$

The flow rate optimization analysis based on calculated efficiencies from the model were in agreement with Tang et al.<sup>[67a]</sup> that the variable flow rate strategy outperforms the constant flow rate.

However, optimal flow factor was reported to fluctuate between 5 and 7. In both studies, only one flow factor (constant flow factor) was tested for round-trips efficiency of the same current.

Konig et al.<sup>[92c]</sup> therefore demonstrated a multiphysical model using different flow factors between 5 and 11 (variable flow factor) to evaluate efficiencies while also considering both current loads and SOC. The introduction of variable flow factor not only facilitate a better increase of the system efficiency than constant flow factor, but also allows the use of smaller pump system. The research group later developed flow rate optimization algorithm for a number of operation points described by charge/discharge current and SOC.<sup>[92d]</sup> In addition to losses from pump power and concentration overpotential, diffusion of vanadium ions through membrane was also discovered as a critical factor that influences flow rate optimization. The model simulation presented a better trade-off among pump power loss, concentration overpotential and diffusion to deliver maximum system efficiency and even at a very high discharge capacity. Compared to previous methods, a better improvement in discharge capacity and system efficiency was obtained. However, in all the aforementioned studies, pump efficiency was taken as constant, which is not the case in real application. To account for the pump efficiency which also vary with different operating conditions including flow rates, a new control strategy was recently introduced<sup>[34a]</sup> Instead of flow factor, the method employed Equations (11a) and (11b) expressed in a modified form of Faraday's law of electrolysis such that limitation region is set for flow rate while the system model coefficients can be estimated and controlled based on the operating conditions

$$\text{For charge: } Q = a \times \left( \frac{1}{\text{SOC}_{\text{cell}}} \right)^m + b \quad (11\text{a})$$

$$\text{For discharge: } Q = a \times \left( \frac{1}{\text{SOD}_{\text{cell}}} \right)^m + b \quad (11\text{b})$$

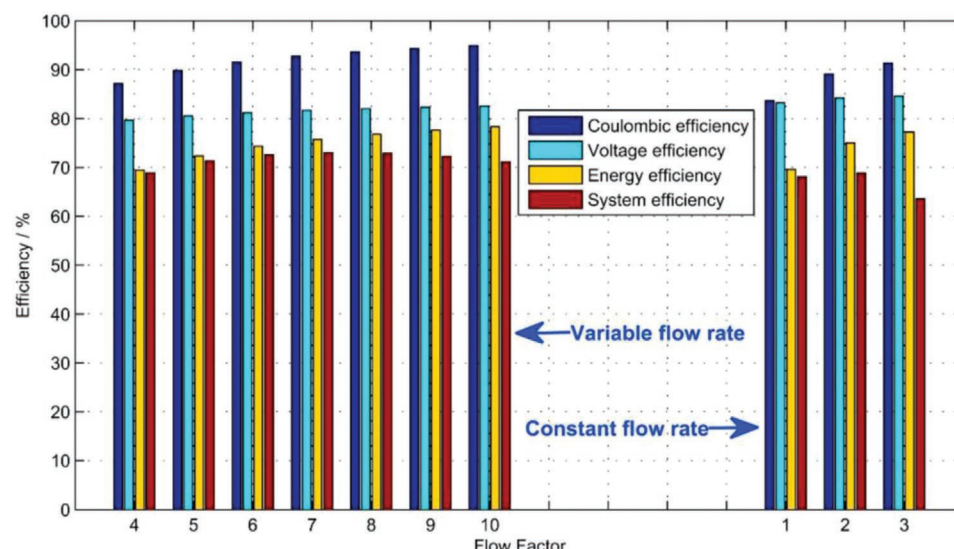


**Figure 6.** Comparison of the efficiencies at variable and constant flow rates. Reproduced with permission.<sup>[67a]</sup> Copyright 2013, Elsevier.

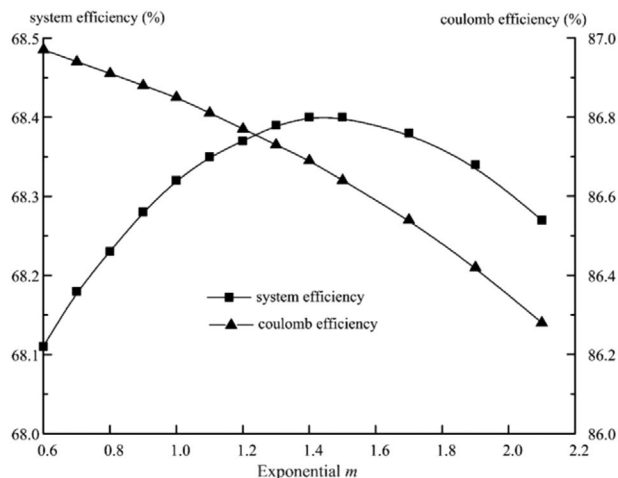


**Figure 7.** Simulated system and coulomb efficiencies in one charge-discharge cycle at different values of exponential  $m$ . Reproduced with permission.<sup>[34a]</sup> Copyright 2018, Elsevier.

where SOC and SOD are state of charge and state of discharge, respectively,  $m$  is the optimal exponential,  $a$  and  $b$  are coefficients to be determined. Simulation results performed at different values of exponential  $m$  under variable flow rate in a single cycle is shown in **Figure 7**. The system and coulomb efficiencies under the new variable flow rate approach were about 4% higher than the results of the constant flow rate at the selected charge and discharge currents as shown in **Table 1**. This was attributed to the consumption of less pump energy in the new strategy, which also promote and validate the benefits of variation of flow rates for improved performance of VRFBs. Therefore, this strategy offers a reliable guidance to optimally regulate electrolyte flow rate in battery systems. The influence of flow field architectures on this control strategy should also be investigated.

**Flow Field Designs:** The selection of appropriate flow field design in VRFBs is of vital importance to achieve adequate mass transport of electroactive species in porous electrodes, which can further influence the operation and power output of

the battery. Hence many researchers have developed interest in understanding the flow field designs which led to numerous experimental studies on the design, functional testing, and comparison of different flow field channels.<sup>[61,64,93]</sup> To better analyze the suitability of these flow field designs, a number of demonstrated numerical modeling and simulations which are based on macroscopic level are discussed in this section.

The first numerical investigation of flow field designs in the operations of VRFBs was reported by Xu et al.<sup>[58b]</sup> The 3D continuum model analyzed and compared the effects of parallel, serpentine, and flow-through structures on performance of VRFBs. Since the uniformity of electrolyte distribution over the surface of electrode is vital importance in determining the effectiveness of flow field design,<sup>[94]</sup> a uniformity factor  $U$  was thus introduced to account for the distribution uniformity of vanadium ions concentration over the electrode surface area<sup>[58b]</sup>

$$U = 1 - \frac{1}{c_{m,i}} \sqrt{\frac{1}{A} \int \int (c_i - c_{m,i})^2 dA} \quad (12)$$

where  $A$  is active surface area of the electrode, and  $c_{m,i}$  denotes the mean vanadium ions concentration at the surface. In comparison with the flow-through electrode, both parallel and serpentine flow field designs were found to facilitate more uniform distribution of electrolytes through the electrode, leading to a decrease in overpotential. However, much reduction in overpotential and pump work, and highest overall cell efficiency was observed in the VRFB with serpentine flow field. This led to more research works toward optimizing the geometry and dimensions of serpentine channel design<sup>[95]</sup> while Zheng et al.<sup>[96]</sup> introduced plug flow field design to regulate and optimize mass transport polarization in flow-through type VRFB. Based on a systematic and optimization study, using a lumped parameter model, on different sizes of serpentine design, an increase in channel width with a reduced rib width has been reported reduce pressure drop for cell performance enhancement.<sup>[95a]</sup> Elsewhere, the height of serpentine channel was reported as the most important geometric variable that influences battery performance. The channel with the smallest height produced the best energy and battery efficiencies as it

**Table 1.** System and coulomb efficiency of constant flow rate and variable flow rate at optimal exponential  $m$  for different charge/discharge. Reproduced with permission.<sup>[34a]</sup> Copyright 2018, Elsevier.

Charging current [A]	Discharging current [A]	Constant flow rate		Variable flow rate		
		System efficiency [%]	Coulomb efficiency [%]	Optimal exponential $m$	System efficiency [%]	Coulomb efficiency [%]
60	60	69.14	85.24	4	72.90	90.29
60	80	65.00	82.74	1.4	68.40	86.69
60	100	60.20	80.02	0.3	63.43	82.77
80	60	68.05	86.40	3.1	71.68	90.53
80	80	63.8	83.00	1.1	67.34	86.97
80	100	59.39	79.33	0.1	62.50	82.96
100	60	66.82	86.54	2.4	70.02	90.63
100	80	62.30	83.06	0.7	65.79	87.01
100	100	58.33	79.01	0.05	61.04	83.04

required least optimal flow rates.<sup>[95c]</sup> More recently, Lee et al.<sup>[95b]</sup> carried out a similar numerical investigation to provide optimal and specific mensuration serpentine flow field. After the consideration of pump losses, serpentine channel of about 2 mm width operating at a flow rate of 60 mL min<sup>-1</sup> produced the highest power-based efficiency. Performing a trade-off analysis among the channel width, height, and depth will therefore provide sufficient details on the geometry of an optimized serpentine channel.

As a result of the omission of interdigitated design in the first modeling framework on flow field,<sup>[58b]</sup> Yin et al.<sup>[97]</sup> employed a 3D continuum model to examine the performance of interdigitated flow field in VRFBs. Interdigitated flow field was described to be more efficient, as it involves less pressure drop and excellent mass transport, than other designs. Various cell characteristics including the velocity of electrolyte flow and distribution of local current in an electrode designed with an interdigitated channel flow were later visualized in through-plane direction.<sup>[98]</sup> The obtained data revealed better understanding on the effects of interdigitated channels in VRFBs. To demonstrate the most efficient flow field design, Zhang et al.<sup>[94]</sup> compared the effects serpentine and interdigitated designs in VRFBs at macroscopic modeling level. Similar to a previous study,<sup>[58b]</sup> uniformity factor was used, not only for the distribution uniformity of vanadium ions only but also for distribution uniformity of current density given as<sup>[94]</sup>

$$U_1 = 1 - \frac{1}{I_m} \sqrt{\frac{1}{A} \iint (I - I_m)^2 dA} \quad (13)$$

where  $I$  is the current density. The interdigitated flow field, with its shorter flow path, not only demonstrate more uniform circulation of vanadium ions, but also performs the least pumping work to attain the highest system efficiency. The result is in good agreement with a recent numerical model developed by Yin et al.<sup>[99]</sup> that compared the interdigitated design with a flow through channel. The interdigitated flow field was also presented as the optimal design for VRFB, using a small-scale topology optimization approach.<sup>[100]</sup> Such approach allows model formulation in a material distribution manner in order to achieve an improved structural design in a particular domain. It was thus applied to the electrode domain to compare the performance of interdigitate design with parallel flow field.

Beyond uniform distribution of species and pump work, a computational fluid dynamics (CFD) model was used to compare the performance of VRFBs with interdigitated and serpentine flow fields under several operating conditions.<sup>[101]</sup> Serpentine performed better than interdigitated design under various operating conditions at fixed flow rate but with higher additional consumption including pressure drop at increase flow rate. Such high pressure drops in serpentine flow field lead to nonuniform reaction rate distribution while uniform reaction rate was observed in interdigitated channels due to the low flow velocity in the electrode. In a more detailed study, Messaggi et al.<sup>[102]</sup> employed a 10 regions macrosegmented cell to investigate the interplay between fluid flow in channels, morphology of electrodes, and local current distribution to compare serpentine and interdigitated designs. Separate analysis and comparison were done at positive electrode, negative electrode,

and the full cell configuration. Just like their previous study,<sup>[101]</sup> both flow field designs also outperformed each other at different operating conditions. This clearly emphasized the conclusion of other studies<sup>[93b,103]</sup> that deciding optimal flow design does not solely depend on the uniform distribution of species and pump work configuration, but on the collective roles of channel designs, electrode and electrolyte properties, and the various operating conditions including pressure drop and current density. Thus, a comprehensive model considering all these factors to evaluate and compare the performance of serpentine, parallel, interdigitated, and perhaps the flow-through designs is needed.

### 3.2.2. Transport Phenomena in Porous Electrodes

**Porous Electrode Theory in Macroscopic Models:** Some theoretical analysis and mathematical models at macroscopic level were earlier performed to study the effects of a number of operating factors such as mass transport resistance, ohmic resistance, and kinetics on the effectiveness of porous electrodes.<sup>[39d,104]</sup> However, only Saleh<sup>[104b]</sup> and You et al.<sup>[39d]</sup> account for electrolyte flow in the flow-through porous electrode. Even though these numerical studies were not performed in the context of VRFBs, they provide guidance to the modeling of flow through porous electrodes within flow battery systems.

In many VRFB models, the transport processes through porous electrode are commonly investigated at macroscopic/volume-averaged level. As such, the electrode properties and structures are assumed to be homogeneous and well distributed all over their entire volume. Thus, the theories and equations on which the modeling of fluid/species/mass transport through porous electrodes on macro scale rely are discussed in this section. Darcy's law is normally used in describing the velocity of electrolyte flow through porous electrodes as follows<sup>[81,85]</sup>

$$\vec{v} = -\frac{K}{\mu} \nabla P \quad (14)$$

With the consideration of continuity equation given as

$$\nabla \cdot \vec{v} = 0 \quad (15)$$

However, when considering the flow in flow field channels with the porous media flow in electrodes, the Brinkman equation is commonly used as<sup>[23a,97]</sup>

$$\frac{\mu}{K} \vec{v} = -P + \mu \left[ \nabla \vec{v} + (\nabla \vec{v})^T \right] \quad (16)$$

where  $v$  is electrolyte velocity,  $\mu$  is dynamic viscosity of fluid,  $P$  is the pressure,  $K$  is permeability of the porous electrode usually described by Carman–Kozeny equation<sup>[85]</sup>

$$K = \frac{d^2 \epsilon^3}{16 C_k (1-\epsilon)^2} \quad (17)$$

where  $d$  is the fiber diameter,  $\epsilon$  is the electrode porosity, and  $C_k$  is the Carman–Kozeny constant mostly used as fitting

parameter depending on the media. Due to the macroscopic continuum approach, the volume-averaged mass conservation in porous electrode is given as<sup>[81]</sup>

$$\frac{\partial}{\partial t}(\varepsilon c_i) + \nabla \cdot \vec{N}_i = -S_i \quad (18)$$

With the assumption of dilute-solution theory, the flux of species in electrolyte flow through the porous electrode is generally modeled using the modified Nernst–Planck equation  $\vec{N}_i$ <sup>[81]</sup>

$$\vec{N}_i = -D_i^{\text{eff}} \nabla c_i - z_i c_i u_i F \nabla \mathcal{O}_s + \vec{v}_c \quad (19)$$

Also, electrolyte in the porous electrode is normally taken to be electrically neutral using the electroneutrality condition<sup>[81]</sup>

$$\sum_i z_i c_i = 0 \quad (20)$$

where subscript i is the species,  $D_i^{\text{eff}}$  is the effective diffusion coefficient,  $c_i$  is the concentration for species,  $z_i$  is the valence of species,  $S_i$  is the source term for species,  $u_i$  is ionic mobility,  $F$  is Faraday's constant, and  $\mathcal{O}_s$  is ionic potential of electrolyte. The effective transport properties such as effective diffusion coefficient ( $D_i^{\text{eff}}$ ) of the porous electrode are calculated using the porosity value. The common method used in previous macroscopic continuum models is known as the Bruggeman correction given as<sup>[81,85]</sup>

$$D_i^{\text{eff}} = \varepsilon^{1.5} D_i \quad (21)$$

Also, the ability of ion to transport through porous electrode known as effective conductivity is given as<sup>[85]</sup>

$$\sigma_s^{\text{eff}} = (1 - \varepsilon)^{1.5} \sigma_s \quad (22)$$

where  $D_i$  is diffusion coefficient and  $\sigma_s$  is the electronic conductivity of the electrode.

Lastly, the charge entering the electrolyte solution is always taken to be equal to the amount of charge leaving the electrode for the conservation of charge expressed as<sup>[85]</sup>

$$\nabla \cdot \vec{i}_e + \nabla \cdot \vec{i}_s = 0 \quad (23)$$

As a result of this approach, sufficient details on the specific surface area and precise porous electrode. Some of these parameters are thus taken as fitted values. This clearly indicates that simulating porous electrodes at macroscopic level may not be accurate to predict the influence of fluid flow through the pore phases and other electrode geometry on the performance of battery system. All these therefore emphasize the need for pore-scale modeling of porous electrodes to resolve the lingering mass transport limitations confronting flow batteries, especially at the pore-level.

**Pore-Scale Modeling:** Xu and Zhao<sup>[39c]</sup> earlier identified the needs to examine the transport mechanisms and properties in porous electrodes not only at the representative element volume (REV) level, but also at the pore-level. Hence a number of pore-scale modeling and simulations have been used to accurately quantify the real geometry and provide information on the microstructure, properties, and transport processes in

porous electrodes in investigating their influence on the performance of VRFBs. In pore-scale models, the precise and detailed pore-scale geometry of porous electrodes and the characteristics of the electrode materials are commonly obtained using X-ray computed tomography (XCT). Lattice Boltzmann method (LBM), which describe the fluid/particles motion by a set of particle velocity distribution functions (PDFs), is mostly used to simulate the electrolyte flow and other reactive transport phenomena in the porous regions of the electrode. A number of recent works have been performed by applying the XCT and the LBM to study the influence of electrode microstructure and transport phenomena in VRFBs.<sup>[43a–c,44]</sup> Qui et al.<sup>[44a]</sup> simulated the flow of electrolyte through the porous electrode of a VRFB using the LBM while the coupled charge and species transport were resolved using finite volume method (FVM) in a 3D pore-scale model with the simulation geometry shown in Figure 8. With this novel method, the actual effects of electrode geometry, electrolyte flow rates, and applied current density on the performance of VRFB were well captured at different operating conditions. The 3D pore-scale model was later applied to analyze the impact of three different electrode morphologies on the performance of VRFBs under varying operating conditions.<sup>[43a]</sup> Electrode structure with high surface area and low porosity was reported to improve battery performance as a result of low and uniform current density and overpotential. In another pore-scale numerical simulation, the effects of microstructural anisotropy on the mass transfer coefficients of three different fibrous electrode materials.<sup>[44d]</sup> In nondimensional forms, the relationship between the mass transfer coefficient and the permeability of the fibrous media with varying anisotropy were determined. Banerjee et al.<sup>[44c]</sup> developed a pore network model to investigate and compare a number of transport properties including permeability and diffusivity of four carbon felt porous electrodes with different geometry but

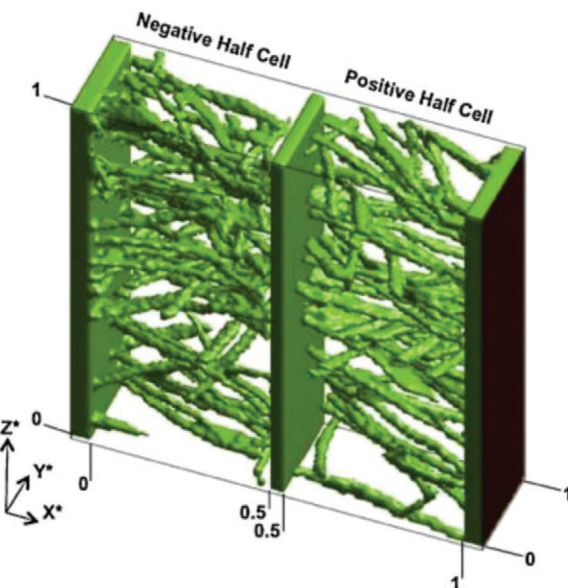


**Figure 8.** Simulation geometry of the pore-scale model. The fiber structure used in the geometry is a subset taken from the original master XCT geometry and exhibits an optimal match of geometric parameters. Reproduced with permission.<sup>[43a]</sup> Copyright 2011, Elsevier.

similar internal pore structures. Single-phase diffusivity and permeability were shown to decrease with increase in the electrodes thickness while relative diffusivity of the electrodes is not influenced by thickness but internal pore structure. Using the LBM and XCT, the dispersion and reaction rate of electrolyte in two samples of porous electrodes (vitrified carbon foam and fibrous carbon felt) were simulated and analyzed at microscopic level.<sup>[43c]</sup> The simulation result shows that the higher tortuosity and active surface area of carbon foam facilitate its capacity for better reaction rate than carbon felt electrode. Pore scale multiphase flow simulations have also been conducted.<sup>[43b,44b]</sup> Zhang et al.<sup>[43b]</sup> simulated capillary pressure of electrolyte transport into electrode using a 3D LBM to determine the effect of wetting surface area in hydrophobic electrode. During the electrolyte transport process, air bubbles were observed to get stuck in the porous electrode which increases concentration and activation overpotential. Increasing the capillary pressure for increase in wet surface was therefore concluded to eliminate air bubbles. In a more comprehensive pore-scale multiphase study, air bubbles at different electrode parameters such fiber diameter, porosity, gas saturations, and surface wettability were investigated for different fibrous electrodes.<sup>[44b]</sup> The LBM was also used to simulate the multiphase flow in the various electrodes and the electrochemical and side reactions at the electrolyte-fiber interface. The electrode surface area covered by gas bubbles were found to be smaller compared to how it is usually portrayed in macroscopic continuum models. The successful development of pore-scale modeling and simulations therefore provides a sound basis for investigating and improving the interrelation among structure, property, and performance of electrodes applied in VRFB. Hence, developing more pore-scale models to realistically examine the effects of electrolyte properties and flow field designs on electrodes is in great need.

### 3.2.3. Transport Phenomena in Membranes

Transport phenomena through the membrane, also referred to as crossover, has received numerous numerical investigations due to its associated capacity loss. Generally, the mathematical models developed to account for the mass and charge transport processes through the membrane in VRFB are transient models and commonly on macroscopic scale. Crossover is mostly a matter of membrane engineering, requiring a critical tradeoff between ohmic losses and undesirable species crossover.<sup>[93b,105]</sup> Species crossover through the membrane is therefore one of the critical issues that markedly affect the reliability and capacity well-being of VRFBs. Diffusion, migration, and convection have been reported as the major mechanisms of species transport through the membrane. Based on dilute-solution theory, the combination of these transport mechanisms forms the Nernst–Planck equation expressed as crossover flux for electroactive species<sup>[106]</sup>

$$\bar{N}_i = -D_i^{\text{eff}} \nabla c_i - \frac{z_i c_i D_i^{\text{eff}}}{RT} F \nabla \phi + \vec{v} c_i \quad (24)$$

The first term is driven by species concentration gradient, electric field determines the second term, and the third term

is driven by the pressure difference across the membrane. In the following section, we consider the macro- and microscale models that have been developed to provide better understanding on the behavior and mechanisms of the multicomponent transport of vanadium ions and water across the membrane.

**Vanadium-Ion Crossover:** The operation of VRFBs usually involve the inevitable transport of vanadium ions from across the membrane which consequently leads to concentration imbalance of electrolytes, temperature increase, side reactions, self-discharge and above all capacity loss.<sup>[56a,107]</sup> The interaction among vanadium ions and protons in each half-cell facilitates the transfer of vanadium ions across the cation exchange membrane mostly used in VRFBs.<sup>[108]</sup> Other than this, membrane properties, operating conditions and parameters, including electrolytes properties also influence the direction and magnitude of vanadium crossover.<sup>[56b]</sup> Modeling and simulations have been applied not only to provide improved prediction of ions transport and its effects on VRFB performance, but to also proffer insights on how to minimize crossover challenges. To numerically examine vanadium ions crossover and its effects in VRFBs, 0D macroscopic models were developed.<sup>[109]</sup> Both studies identified and considered diffusion as the only mechanisms of vanadium ions crossover through the membrane responsible for capacity loss, thereby neglecting the contributions of migration and convection mechanisms. Using a 3D model, Oh et al.<sup>[110]</sup> numerically analyzed and compared the effects of both diffusion and migration on vanadium-ion crossover. A significant change in the rate of vanadium crossover during charge and discharge as shown in **Figures 9** and **10** when migration was considered in addition to diffusion clearly shows the importance of migration mechanism. This emphasize the significant importance of migration. The roles of convective transport, which is the third mechanism, in vanadium ion crossover was modeled by Knehr and Kumbur.<sup>[111]</sup> Osmosis and electro-osmosis were further identified as the mechanisms that facilitate net convection crossover. Their simulation result show that convective transport of species also plays significant impacts on the net vanadium crossover. The theoretical analysis of the contribution of migration and electro-osmosis to vanadium-ion crossover was then performed by Darling et al.<sup>[112]</sup> to show the dependence of the two transport mechanisms on current density and membrane thickness. A lumped parameter modeling approach was later applied to account for the three mechanisms, with various membrane thickness, in determining their influence on battery capacity.<sup>[105]</sup> Another 0D model properly revealed the contribution of the three transport mechanisms toward capacity loss at different current densities of 40, 60, 80, and 100 mA cm<sup>-2</sup>.<sup>[113]</sup> As shown in **Figure 11**, the net crossover was concluded to be predominated by convection mechanism at the operating condition used and therefore should not be neglected in the simulation of vanadium-ion crossover. However, membrane-type and electrolyte properties in addition to operating conditions adopted in modeling and simulations of VRFBs also influence the contribution of each transport mechanism. This was justified by the 2D model developed by Agar et al.<sup>[114]</sup> to investigate and compare the individual contribution of the three transport mechanisms

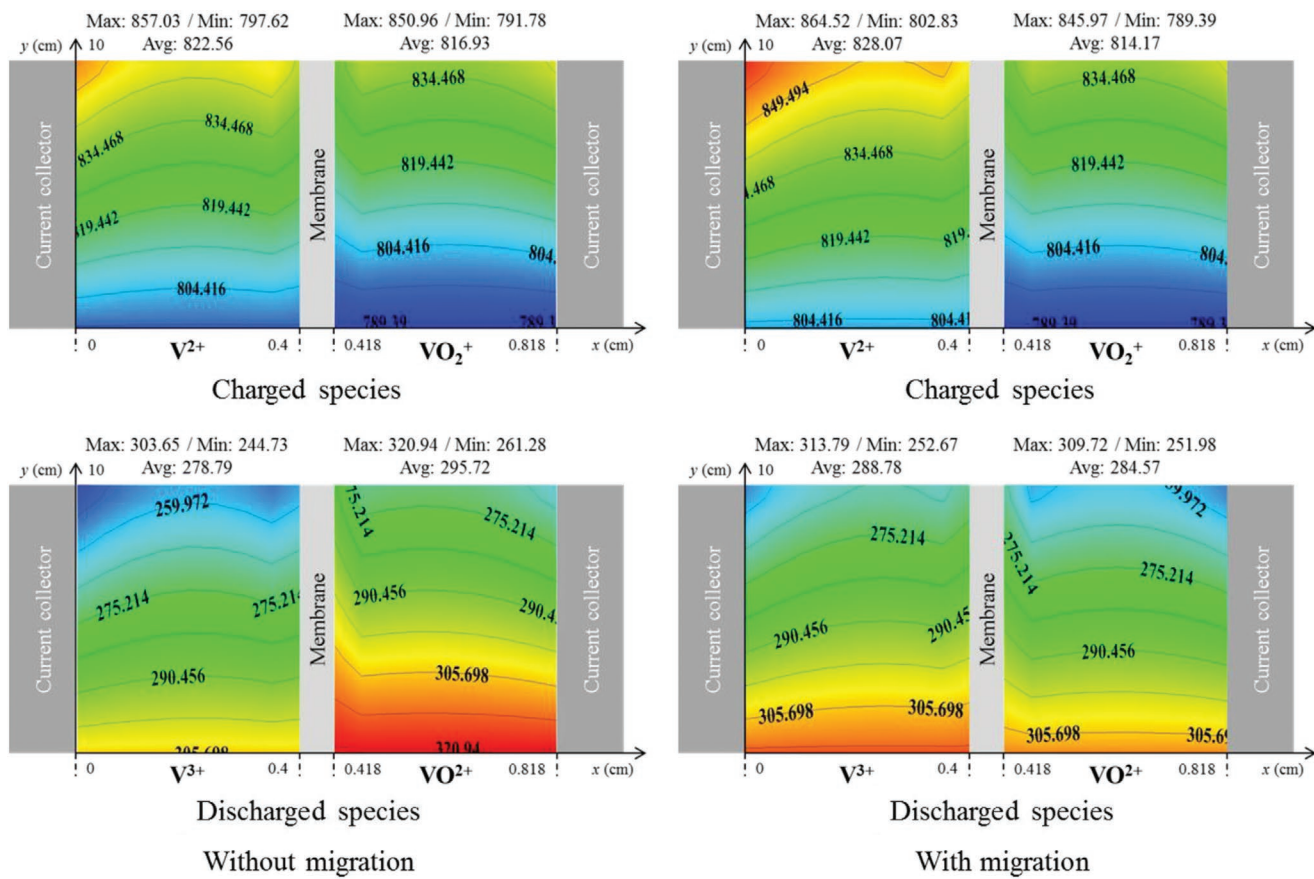


**Figure 9.** Contours showing the vanadium ions concentrations in the both electrodes during charging with  $0.1 \text{ A cm}^{-2}$  at 74% SOC. Reproduced with permission.<sup>[110]</sup> Copyright 2015, Elsevier.

in Nafion 117 and sulfonated Radel (s-Radel) membranes. Diffusion was found to be dominate crossover mechanism in the Nafion membrane, while convection dominates the net vanadium crossover in s-Radel membrane. While all these macroscopic numerical studies describe the various transport phenomena inside the membrane, they failed to account for the discontinuity of species concentration and ionic potential at the M-E interface. In real applications, Donnan potential occurs across the membrane due to the differences in proton concentrations between the electrolytes on both sides of the membrane<sup>[56b,91]</sup> and the presence of fixed charge concentration inside the membrane.<sup>[57]</sup> This indicates that the consideration of the Donnan effect at the membrane-electrolyte interface to accurately model ions transport across the membrane is required.

A number of modeling and simulations studies on VRFB have incorporated this interface and the Donnan effect to properly couple electrode and membrane physics.<sup>[55,56b,57,115]</sup> Knehr et al.<sup>[56b]</sup> considered the M-E interface as a finite thickness comprising a portion thickness from both electrolyte and membrane regions. The interface was incorporated into their model by discretizing only the diffusion and migration terms in Nernst–Planck equation, neglecting the term convection term. Species fluxes, except  $\text{HSO}_4^-$  due to the presence of fixed charge in the membrane, at the interface is therefore expressed as

$$N_i^{\text{er}} = -D_i^{\text{eff}} \frac{(c_i^e - c_i^{\text{junc}})}{\delta e} - z_i u_i^e F \frac{(c_i^e + c_i^{\text{junc}})}{2} \frac{K_{\emptyset} (\emptyset_i^e - \emptyset_i^m)}{\delta e} \quad (25a)$$

$$N_i^{\text{mr}} = -D_i \frac{(c_i^{\text{junc}} - c_i^m)}{\delta m} - z_i u_i^m F \frac{(c_i^{\text{junc}} + c_i^m)}{2} \frac{(1 - K_{\emptyset}) (\emptyset_i^e - \emptyset_i^m)}{\delta m} \quad (25b)$$

where  $N_i^{\text{er}}$  and  $N_i^{\text{mr}}$  are the species flux in the electrolyte and membrane part of interface, respectively,  $c_i^{\text{junc}}$  is the specie concentration at the interfacial junction which is solved by taking  $N_i^{\text{er}} = N_i^{\text{mr}}$ ,  $K_{\emptyset}$  is a fitting parameter that denotes the proportion of the potential discontinuity ( $\emptyset_i^e - \emptyset_i^m$ ) existing at the interface. Electroneutrality at the interface for  $\text{HSO}_4^-$  concentration on both sides of the membrane was assumed as

$$c_{\text{HSO}_4^-}^{\text{junc},m} = c_{\text{HSO}_4^-}^{\text{junc},e} - c_f \quad (26)$$

where  $c_f$  is the fixed charge concentration,  $c_{\text{HSO}_4^-}^{\text{junc},e}$  is solved by replacing  $c_i^{\text{junc}}$  in Equations (25a) and (25b) with  $c_{\text{HSO}_4^-}^{\text{junc},e}$  and  $c_{\text{HSO}_4^-}^{\text{junc},e} - c_f$ , respectively, and thereafter set  $N_{\text{HSO}_4^-}^{\text{er}} = N_{\text{HSO}_4^-}^{\text{mr}}$ . The individual direction and contribution of diffusion, migration, and convection components to the overall crossover during charge and discharge cycles was properly illustrated and compared. Yang et al.<sup>[115]</sup> did not include any fitting parameter or assumption at the interface, but only allows the species

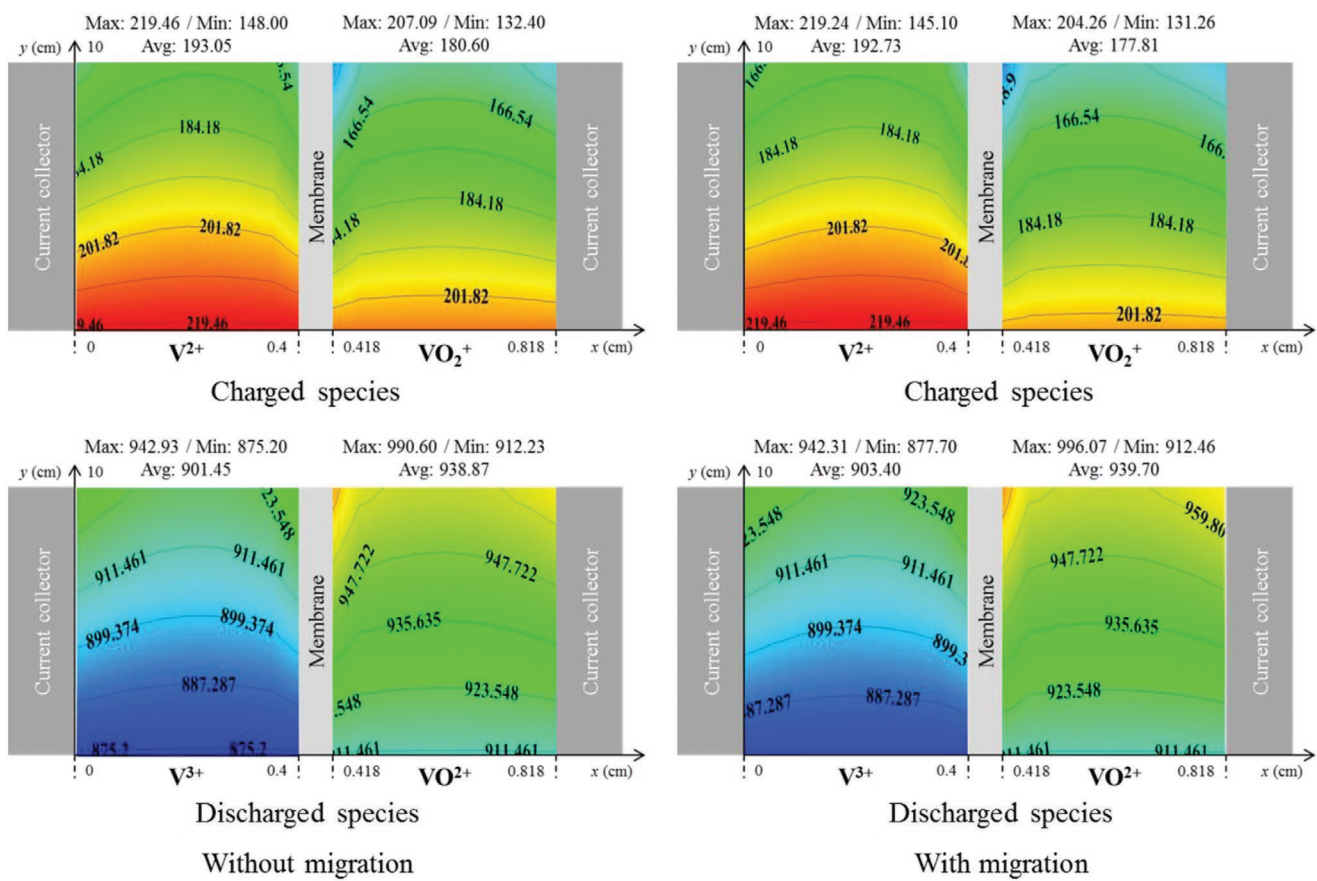


**Figure 10.** Contours showing the vanadium ions concentrations in the both electrodes during discharge with  $0.1 \text{ A cm}^{-2}$  at 74% SOC. Reproduced with permission.<sup>[110]</sup> Copyright 2015, Elsevier.

concentration and potential discontinuity to be directly captured in the modeling domain as shown in **Figure 12** without a precise mathematical analysis of the mechanism at the M–E interfaces. In addition, Donnan potential at the M–E interfaces was only taken as

$$\Delta\phi_D = \phi_e^m - \phi_e^{ele} \quad (27)$$

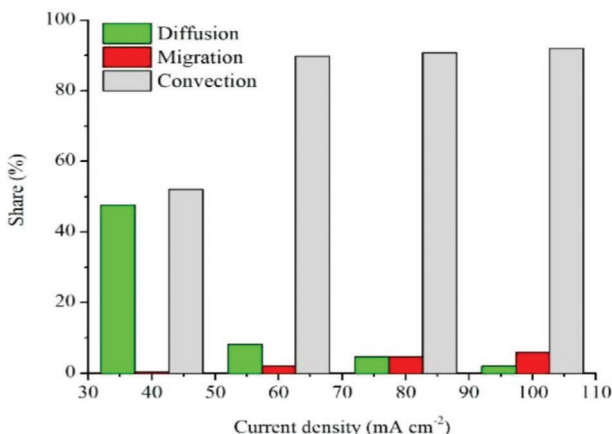


**Figure 11.** The individual contribution of transport mechanisms to capacity loss in a VRFB at different current densities. Reproduced with permission.<sup>[113]</sup> Copyright 2018, Elsevier.

Following the correlation given for Donnan potential at M–E interface by Kontturi et al.,<sup>[56a]</sup> such that  $Z_f\Delta\phi_D \geq 0$ . Where  $\phi_e^m$  and  $\phi_e^{ele}$ , and  $Z_f$  is the valence of fixed charge in cation exchange membrane is normally taken as  $-1$ . Unlike Knehr et al.<sup>[56b]</sup> model where the Donnan potential was assumed to be positive, a negative value was therefore used. The simulation results presented the direction of the net vanadium flux resulting from the three transport mechanisms during charge and discharge processes as shown in **Figure 13**. To accurately model the mechanisms at the M–E interface, a clear description of the complex transport processes occurring at the interface is essential. Lei et al.<sup>[55a]</sup> developed a model where Poisson equation was coupled with the Nernst–Planck equation to study the role of space charge region in addition to Donnan effect at the M–E interface. It was pointed out that electroneutrality is not suitable at the M–E interface, due to the presence of space charge region when the fixed charge in the membrane is exposed to electrolyte. As shown in **Figure 14**, the space charge region is explained to be neutral, hence the ionic charge in the electrolyte is taken as zero while that of the membrane is  $-z_m c_m$ , where  $z_m$  is the valence and  $c_m$  is the concentration of fixed charge. The simulation indicated that Donnan effect promotes vanadium crossover, particularly with increase in fixed charge concentration in the membrane, which in turn leads to decrease in the coulombic efficiency of the battery system. The same research group later developed a model for ion selective adsorption in

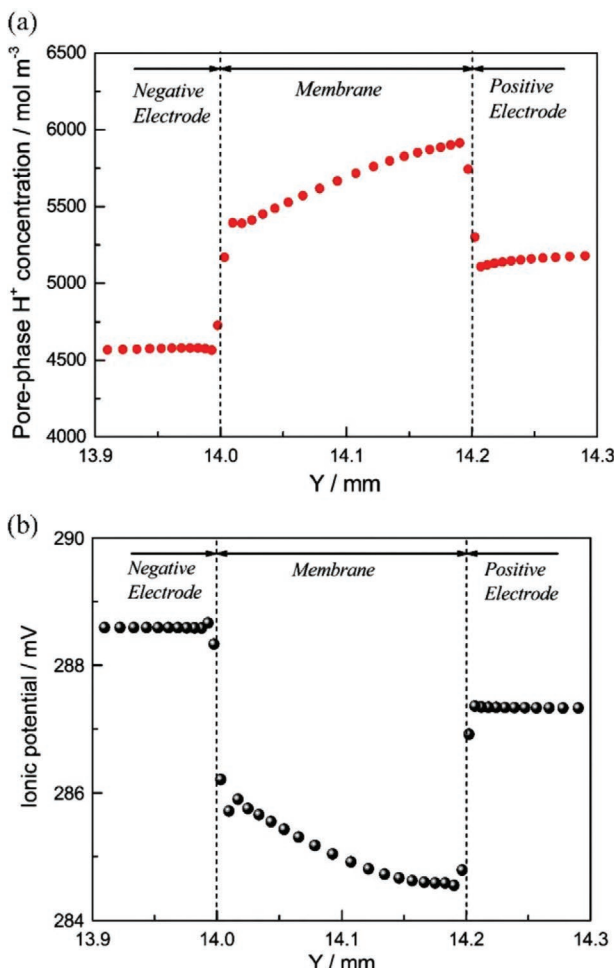


**Figure 12.** Distributions of a) pore-phase proton concentrations and b) ionic potential across the membrane. Reproduced with permission.<sup>[115]</sup> Copyright 2015, Elsevier.

membrane to accurately capture vanadium-ions crossover.<sup>[55b]</sup> Pore volume-averaged approach was introduced to describe the Donnan effect at the M-E interface particularly for movable ions and fixed charges in the pores of the membrane. Hence

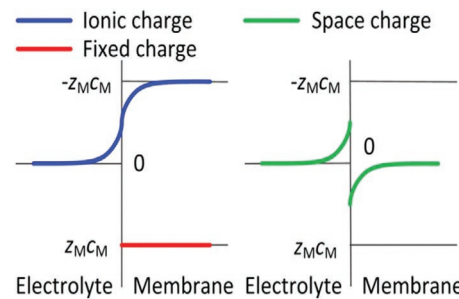


**Figure 14.** Ionic, fixed and space charges at the membrane-electrolyte interface. Reproduced with permission.<sup>[55a]</sup> Copyright 2015, Elsevier.

the electrochemical potential  $\mu_i$  for each ion at both M-E interfaces is expressed as

$$\mu_i = \mu_{i,e}^0 + RT \ln c_{i,e} + z_i F \mathcal{O}_{i,e} = \mu_{i,m}^0 + RT \ln c_{i,m} + z_i F \mathcal{O}_{i,m} \quad (28)$$

where  $\mathcal{O}_i$  denotes ionic potential, subscript s and m are the electrode and membrane side. This equation was later adopted in the models developed by Hao et al.<sup>[57]</sup> to further model species concentration and ionic potential at the M-E interface. The ion concentration ratio across the interface was combined with ionic potential difference, expressed as

$$\frac{c_i^m}{c_i^e} = \exp\left(\frac{\mu_{i,e}^0 - \mu_{i,m}^0}{RT}\right) \exp\left(z_i F \mathcal{O}_e - \mathcal{O}_m\right) \quad (29)$$

Also, the flux of each specie across the M-E interface was stated to be equal using

$$-D_i^e \nabla c_i^e - z_i u_i^e c_i^e F \nabla \mathcal{O}_e + c_i^e \nu = -D_i^m \nabla c_i^m - z_i u_i^m c_i^m F \nabla \mathcal{O}_m + c_i^m \nu \quad (30)$$

Apparently, the mechanisms of vanadium-ions transport across membrane has been modeled in different ways with diverse considerations and assumptions. Developing a comprehensive and general approach to this transport process, including better clarification at M-E interfaces, is therefore in great need for future numerical study.

**Water Crossover:** Apart from vanadium ions, water crossover through membrane in VRFBs is a salient issue that has also drawn the attention of researchers. The crossover of vanadium ions is one of modes for water crossover in the flow battery as vanadium ions transport is usually accompanied with bound water. Other factors causing water transfer across membrane include pressure difference from the two half-cells, and electro-osmotic drag from the ions transport through the membrane.<sup>[116]</sup> Water crossover phenomenon therefore leads to the precipitation of active species in one half-cell, and which in turn results to the flooding and dilution of species in the other half-cell. It is worth noting that water transport, alongside protons, through membrane is indispensable in the operations of VRFBs to balance the charges. As such, various experimental efforts have been made to reduce excessive and preferential transfer of water in the battery system.<sup>[117]</sup> Meanwhile few numerical studies have accounted for water transport mechanisms across the membrane in VRFB models. In one of the premier VRFB models, Shah et al.<sup>[81]</sup> considered the change in water concentration at the positive and

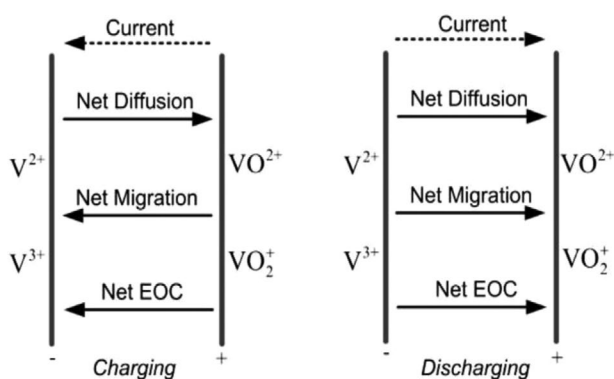


**Figure 13.** The direction of net vanadium crossover due to the three transport mechanisms in charging and discharging in relation to the direction of current. Reproduced with permission.<sup>[115]</sup> Copyright 2015, Elsevier.

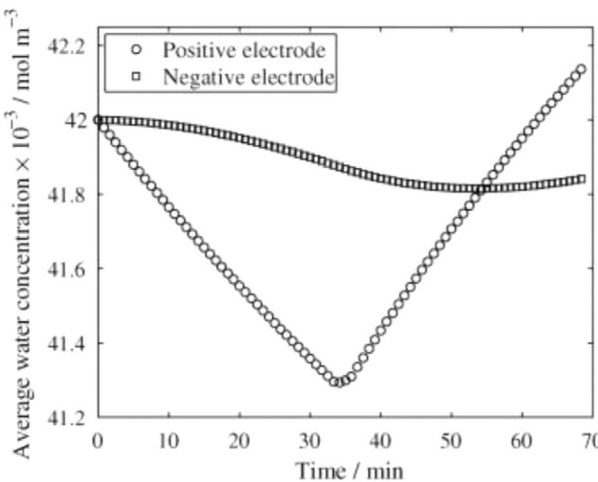


**Figure 15.** Average water concentration at the negative and positive electrodes during a charge–discharge cycle of a VRFB. Reproduced with permission.<sup>[81]</sup> Copyright 2008, Elsevier.

negative electrodes. The simulation shows that net water transfer occurs from the negative half-cell to the positive during charge and the opposite trend at the end of discharge. Based on the small timescale of the model, the variation of water concentration at the two electrodes is relatively small as shown in **Figure 15**. Wang and Hao<sup>[57a]</sup> and Knehr et al.<sup>[56b]</sup> and also considered water crossover in their VRFB models while investigating changes in electrolyte volume and ions transport mechanisms through the membrane.

In a more comprehensive model, Ju and his research team<sup>[118]</sup> developed a water transport model which accounts for the generation, consumption and transport mechanisms of water in VRFBs. The 3D transient numerical model considered vanadium species transfer, osmotic pressure gradient, and electro-osmotic drag as the three major mechanisms of water crossover. The model introduced a new water balance equation particularly useful when the model is based on dilute approximation theory. The equation is given as<sup>[118]</sup>

$$\frac{\partial(\varepsilon C_w)}{\partial t} + \nabla \cdot (-D_w^{\text{eff}} \nabla C_w + \bar{u} C_w) = S_w \quad (31)$$

where  $D_w^{\text{eff}} = \varepsilon^\tau D_w$  and  $\tau$  is electrode tortuosity. Water quantity in the membrane  $\lambda$  was taken in terms of water activity,  $a$  in order to determine the transport properties in the membrane

$$a = \frac{C_w^g RT}{P_{\text{sat}}} \quad (32)$$

$$\lambda = \begin{cases} \lambda^g = 0.043 + 17.81a - 39.85a^2 + 36a^3 & (0 < a \leq 1) \\ \lambda^l = 22 & \end{cases} \quad (33)$$

According to the simulation results, water crossover is predominated by diffusion and electro-osmotic drag components. While electro-osmotic drag-driven water crossover were found to be symmetric between charge and discharge process; diffusion-dominated water crossover is unidirectional. More numerical investigations illustrating the strategies to attain lower

water transfer across various types of membrane and methods of balancing water content on both sides of the membrane should be given consideration.

### 3.2.4. Electrochemical Kinetics

The Butler-Volmer equation has been widely employed to describe the reversible electrochemical reactions occurring at the solid surface of porous electrodes in VRFBs. Not only this, the equation also projects the relationship between the transfer current density ( $j_\pm$ ) of the electrochemical reactions and activation overpotential ( $\eta_\pm$ ) at the surface of both positive and negative porous electrodes.<sup>[29b,89]</sup>

At the positive porous electrode

$$j_+ = aFk_+ (c_{V^{4+}}^s)^{\alpha_{1,c}} (c_{V^{3+}}^s)^{\alpha_{1,a}} \left[ \exp\left(\frac{\alpha_{1,c} F \eta_+}{RT}\right) - \exp\left(-\frac{\alpha_{1,a} F \eta_+}{RT}\right) \right] \quad (34a)$$

$$\text{The exchange current density } i_+ = aFk_+ (c_{V^{4+}}^s)^{\alpha_{1,c}} (c_{V^{3+}}^s)^{\alpha_{1,a}} \quad (34b)$$

$$\text{Activation overpotential } \eta_+ = \phi_s - \phi_l - E^+ \quad (35)$$

At the negative porous electrode

$$j_- = aFk_- (c_{V^{3+}}^s)^{\alpha_{1,c}} (c_{V^{4+}}^s)^{\alpha_{1,a}} \left[ \exp\left(\frac{\alpha_{1,c} F \eta_-}{RT}\right) - \exp\left(-\frac{\alpha_{1,a} F \eta_-}{RT}\right) \right] \quad (36a)$$

$$\text{The exchange current density } i_- = aFk_- (c_{V^{3+}}^s)^{\alpha_{1,c}} (c_{V^{4+}}^s)^{\alpha_{1,a}} \quad (36b)$$

$$\text{Activation overpotential } \eta_- = \phi_s - \phi_l - E^- \quad (36c)$$

where  $a$  is the active specific surface area ( $\text{m}^{-1}$ ),  $F$  is the Faraday's constant ( $\text{C mol}^{-1}$ ),  $\alpha_{1,c}$  and  $\alpha_{1,a}$  are the cathodic and anodic charge transfer coefficients, respectively,  $k_+$  and  $k_-$  are the rate constants for the positive and negative reactions, respectively,  $\phi_s$  and  $\phi_l$  are the electrode and electrolyte potentials, respectively,  $c_i^s$  represents the vanadium species concentrations at the electrode–electrolyte interface of the porous area (surface concentration). It is generally different from the bulk concentration as a result of the added transport resistance to and from the bulk solution to the electrode surface. A more detailed derivation of the relationship between the bulk concentration, surface concentration, and the local mass transfer coefficient  $k_m$  is given in refs. [81, 85]. All these equations are conveniently used to accurately depict the kinetics of the redox reactions of VRFBs. However, there are some modeling and simulation studies on VRFBs that employ Marcus theory to account for the rate of electron transfer in redox reactions.<sup>[119]</sup>

### 3.2.5. Shunt Current

Shunt current is also one of the undesirable phenomena that take place during the cycling operation of VRFBs. It is a major

source of ohmic loss in the bipolar cell stacks design of the battery system.<sup>[12b,68b]</sup> Shunt current refers to the deviation of electrical current from the usual path in the serially connected cells of a VRFB stack. The connecting pipes and jointly-shared electrolyte manifold supplying electrolyte solution into the cells has been observed to be the cause of shunt current.<sup>[120]</sup> Shunt current through such structural existence markedly affects the performance of the flow battery. For instance, shunt current leads to the corrosion of cell stack materials, thereby shortening its life-cycle; and the reduction of energy and coulombic efficiencies of the flow battery through internal self-discharge.<sup>[121]</sup> The number of cells within the stack, the dimension and geometry of manifold and cell flow frame, state of electrolyte, electrolyte conductivity, system voltage are generally the sensitive factors that mostly influence the magnitude of shunt current in VRFBs.<sup>[122]</sup> To better understand the evolution of shunt in VRFBs, Skyllas-Kazacos et al.<sup>[121b]</sup> described the mechanism under three operating conditions—standby, charging, and discharging. In these three states, shunt current was observed to take place as a result of the internal self-discharge reactions in the stack under the influence of cell voltage, even at open-circuit, and without the flow of electrons through the external circuit. Consequently, the time required to charge the cell to a full state increases, leading to a drop in the current efficiency of the charging process, while the depletion of active species concentration during the discharge process contributes to capacity loss. In order to mitigate and even eliminate shunt current loss and maintain high energy efficiency of the battery, modeling, and simulation efforts have been taken by different research groups in this regard.

Researchers at NASA<sup>[123]</sup> were the first to model shunt current in FB. The model developed was based on electrical circuit model of bipolar stack. Till date, most of the models that have been proposed to analyze shunt current distribution and losses in VRFB are performed using equivalent electrical circuit analogy method<sup>[34b,68b,120b,c,121a,124]</sup> typically shown in Figure 16. Among them was the circuit analog model developed by Xing et al.<sup>[121a]</sup> to investigate shunt current in a VRFB comprising a number of cells in the stack during the charge and discharge process. The shunt current loss during the cycling process was estimated via the equation

$$Q_f = \int_0^{t_c} \sum_{num=1}^N I_{num}^c(t) dt + \int_0^{t_d} \sum_{num=1}^N I_{num}^d(t) dt \quad (37)$$

where  $I$  is the total shunt current in the manifold and channel during the charge  $c$ , and discharge  $d$  for a given number of cell num at time  $t$ . Tang et al.<sup>[34b]</sup> developed a dynamic thermal model to examine the impacts of shunt current not only on the stack performance but also on the thermal condition of a VRFB under a standby condition. As expected, their results indicate that the presence of shunt current led to a decrease in both energy and coulombic efficiencies during the charge and discharge cycle, which was attributed to poor flow-frame of the cell which promotes the deviation of ionic current. The simulation of the thermal effect shows that the temperature of the stack steadily increases because of the ohmic loss from shunt current together with its concomitant internal heat generated in the stack. This is in line with the simulation results of the effects

of shunt current on the thermal condition of VRFBs carried out by Trovo et al.<sup>[120b]</sup> The result shows that shunt current generates wider temperature gradient among cells within the stack which could lead to the precipitation of vanadium ion, particularly  $\text{VO}_2^+$ .

In another study, Wandschneider et al.<sup>[125]</sup> developed a simulation model of shunt currents based on an equivalent circuit for a VRFB system consisting of three stacks which are connected in series. The model was used to evaluate and compare the performance of three different pipe arrangements, which are stacks without pipe connection, inflow and outflow pipes on one side of the stack, and both pipes on opposite sides of the stacks as shown in Figure 17. Based on the simulation results, the stack set up without pipe connections gave the highest coulombic efficiency and energy efficiency at three different current densities. Much decrease in these efficiencies was observed in the arrangement where inflow and outflow pipes were placed on the same side of the stack. This is attributed to the addition of external shunt current to the battery system which correspondingly increase the internal shunt current of the stacks. A comprehensive model of shunt current combining hydraulic circuit and electrical model of VRFB was developed by Zhang et al.<sup>[68b]</sup> Their simulation results after considering a stack of 15 cells reveals that shunt current reduces the available current in the cell during charge while the current is increased during the discharge process.

Results from the sensitivity analysis of shunt current show that decreasing the number of single cells in series, increasing the resistance effect of the connecting channel and electrolyte manifolds, and increasing the power rating of individual cell in the stack would all contribute to minimize shunt current in VRFBs.<sup>[121a]</sup> Channels with longer length and reduced cross-sectional area was also recommended to reduce the adverse effect of shunt current.<sup>[121b,126]</sup> However, such dimension would result to increase in pressure drop and pump-work which could also reduce round trip efficiency. This is due to the fact that pressure drop and electrical resistance are proportional to pipe length.<sup>[127]</sup> Hence, a balance state between the two parameters is required for optimum performance. In response to this, Ye et al.<sup>[126]</sup> investigated the optimal trade-off between shunt current loss and pump-work loss in the piping design for a multi-stack VRFB. They provided useful piping system design guidelines which are very much applicable to other types of flow batteries.

The application of a protective current to the conductive route in the same direction with the shunt current through the flowing electrolyte have been proposed to reduce and or eliminate shunt currents in electrochemical devices<sup>[128]</sup> and likewise shunt resistors.<sup>[126]</sup> Recent modeling and simulation research work on VRFBs<sup>[120b,129]</sup> are now analyzing the effects of shunt currents on only the power system of the cell stack design. Shunt current loss becomes severe with the increase in the number of cells in the stack.<sup>[68b,122a,123a]</sup> This was justified by the simulation result of a 3D electrochemical model of shunt current distribution as a function of the number of cell and electrolyte conductivity as shown in Figure 18.<sup>[130]</sup> This highlights the importance of considering the side effects of the number of cells in a stack, especially shunt current, while designing a large-scale VRFB.

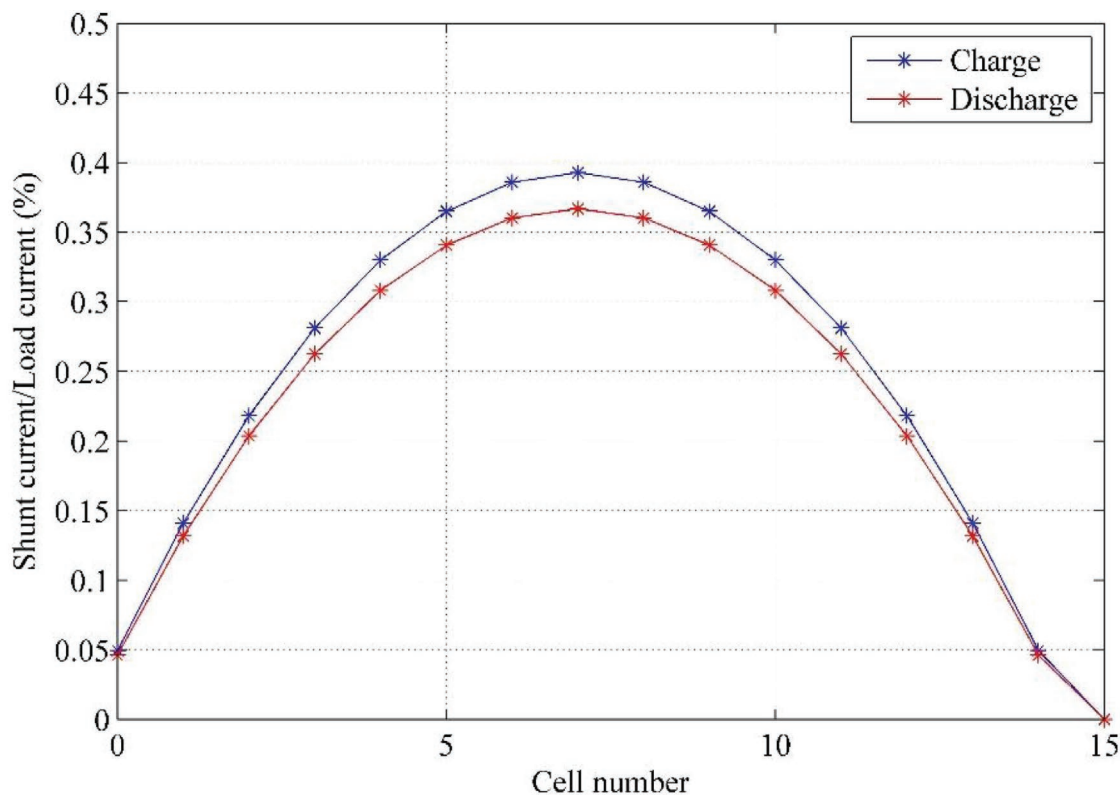
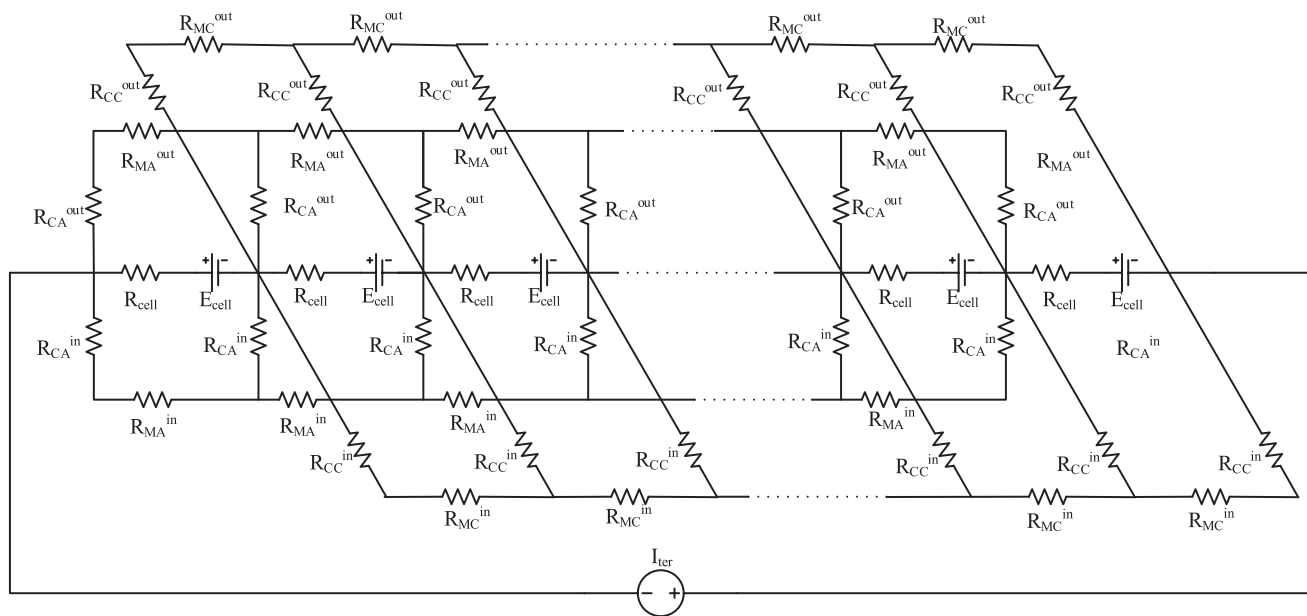


**Figure 16.** a) An equivalent electrical circuit for analyzing bipolar cell-stack; b) predicted shunt current distribution in a 15-cell stack at 50 mA cm<sup>-2</sup> and 0.5 SOC. Reproduced with permission.<sup>[68b]</sup> Copyright 2015, Elsevier.

### 3.2.6. Side Reactions

During a long-term operation of VRFBs, the electrochemical reactions on electrode surface have been reported to exhibit some undesired side reactions. These are in form of oxygen evolution reaction and carbon corrosion occurring at the positive

electrode; and oxidation of divalent vanadium ions by air and the evolution of hydrogen gas, both at the negative side.<sup>[131]</sup> While carbon electrode corrosion and oxidation of divalent vanadium ions has been reported to be relatively preventable,<sup>[132]</sup> the evolution of hydrogen and oxygen gases on the electrodes are a bit difficult to obviate, even though the application of a

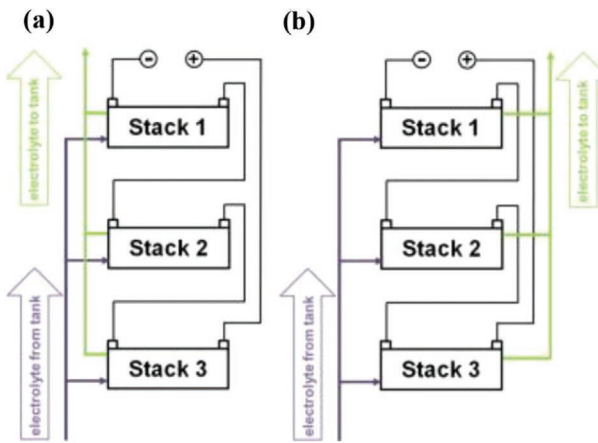


**Figure 17.** Serially connected VRFB multistack showing the electrolyte solution (anolyte) a) on the same side and b) on opposite sides, as the inlet and outlet of the catholyte is ordered in the same way. Reproduced with permission.<sup>[120c]</sup> Copyright 2014, Elsevier.

cut-off voltage was once mentioned to curtail oxygen evolution reaction.<sup>[133]</sup> Due to the significant role of side reactions to the detriment of flow battery performance, their identification and measurement including preventive approaches are expected to attract a lot of research attention. However, a good number of VRFB modeling and simulation studies always take the contributions of side reactions to be negligible during model formulation. Consequently, very few modeling works have been dedicated to analyzing the effects of side reactions on the battery efficiency, and how to minimize their occurrence. The research works by Shah and his research team on the effects of side reactions, particularly on the modeling of hydrogen evolution<sup>[83]</sup> and oxygen evolution<sup>[84]</sup> in VRFBs, are the major model-based investigation pertinent to this section.

**Hydrogen Evolution:** Hydrogen evolution reaction (HER) involves the production of hydrogen gas, usually in form of macroscopic bubbles, at the negative electrode of VRFB as follows<sup>[83]</sup>



It has been described as a parasitic side reaction as this process leads to severe negative impacts on battery performance including

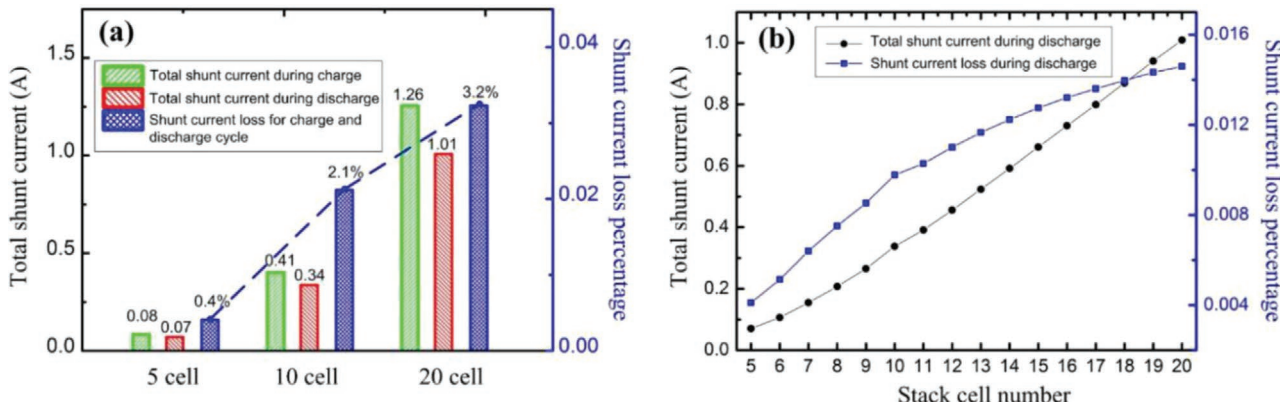


**Figure 18.** Total shunt current and shunt current loss of VRFB with respect to the number of cell in the stack in a) charge-discharge cycle and b) discharge process at 50% SOC. Reproduced with permission.<sup>[130]</sup> Copyright 2015, Elsevier.

electrolyte and charge imbalance.<sup>[39a,134]</sup> The gas bubbles obstruct the smooth flow of electrolyte solution through the porous electrode and therefore cut down the effective electrode active sites for redox reaction, which ultimately leads to mass transport resistance as well as activation losses.<sup>[71c,131c,135]</sup> All these effects are not desirable for the smooth performance of battery system.

The modeling of hydrogen evolution and its various sides effects in a VRFB was reported by Shah et al.<sup>[83]</sup> in which a modified multiphase-mixture strategy was employed. The corresponding decrease in the amount of electrolyte at the negative half-cell caused by the formation of hydrogen gas bubbles was considered in the model. The volume conservation for the gas and liquid electrolyte in the porous regions of the electrode was taken as

$$\alpha_l + \alpha_g = 1 \quad (39)$$

where  $\alpha_l$  and  $\alpha_g$  are the volume fraction of liquid electrolyte and gas bubbles. However, the liquid-phase was assumed to govern the momentum equation in the model. Hence, the continuity equation for the gas-liquid mixture was reduced to that of the liquid phase only

$$\nabla \cdot \bar{u}_l = 0 \quad (40)$$

where  $\bar{u}_l$  the velocity of the liquid through the porous electrode was given as

$$\bar{u}_l = -\frac{d^2}{K\mu} \frac{\varepsilon^3 (1-\alpha_g)^3}{(1-\varepsilon(1-\alpha_g))^2} \nabla P \quad (41)$$

Even though the authors mentioned that the actual multireaction processes involved is not well known, the reaction kinetics using the Butler–Volmer expression for the negative and positive electrodes, respectively, were expressed as

$$j_- = a\epsilon(1-\alpha_g)Fk_-(c_{V^{3+}}^s)^{\beta_-} (c_{V^{2+}}^s)^{(1-\beta_-)} \left[ \exp\left(\frac{F(1-\beta_-)\eta_-}{RT}\right) - \exp\left(-\frac{F\beta_-\eta_-}{RT}\right) \right] \quad (42a)$$

$$j_+ = a\epsilon(1-\alpha_g)Fk_+(c_{V^{4+}}^s)^{\beta_+} (c_{V^{5+}}^s)^{(1-\beta_+)} \left[ \exp\left(\frac{F(1-\beta_+)\eta_+}{RT}\right) - \exp\left(-\frac{F\beta_+\eta_+}{RT}\right) \right] \quad (42b)$$

where  $\beta_{\pm}$  and  $(1 - \beta_{\pm})$  are anodic and cathodic charge transfer coefficients, respectively. Tafel equation was used to describe the current density related to HER at the negative electrode as follows

$$\vec{j}_{H_2} = \nabla \cdot \vec{j}_{H_2} = -A\varepsilon(1-\alpha_g)j_{0,H_2} \exp\left(-\frac{F\beta_{H_2}\eta_{H_2}}{RT}\right) \quad (43)$$

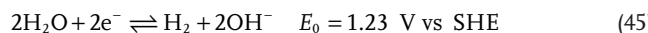
where  $j_{0,H_2}$  represents the exchange current density, and  $\eta_{H_2}$  is the HER overpotential.

The overall current density used at the negative electrode was then given as the summation of current density of HER and that of the redox reactions expressed as

$$\nabla \cdot \vec{j} = \nabla \cdot \vec{j}_- + 2\nabla \cdot \vec{j}_{H_2} = j_- + 2j_{H_2} \quad (44)$$

The numerical simulation results reveal that HER hinders the overall system performance. For instance, through the reduction of current density meant for the electrochemical reaction at the electrode which is partially consumed to fuel the evolution of hydrogen gas. Through the pore-scale model, the effects of HER on VRFBs should be studied so as to accurately account for the participation of both liquid and gas phases in the reaction mechanisms.

**Oxygen Evolution:** Another form of side reaction common in VRFBs is the oxygen evolution reaction (OER). This phenomenon involves the generation of oxygen gas as well as formation of the gas bubbles at the positive electrode surface, most especially during the charge cycling of the battery at high voltage.<sup>[131a,133]</sup> Similar to HER, the formation of oxygen bubbles not only reduces the reactive surface area of the electrode, but also prevents enough electrolyte solution from flowing into the electrode channels. Moreover, OER often leads to corrosion of the electrode material and on the long run mutilate battery operation.<sup>[132–133,136]</sup> The OER at the positive electrode is as follows, respectively<sup>[131a,137]</sup>



Using the modified multiphase-mixture method, Shah and his research team also developed a 2D model to investigate the impacts of oxygen evolution and its bubbles formation in VRFBs.<sup>[84]</sup> Unlike the model for HER, the effects of operating temperature were taken into consideration in this model. Hence, the reaction constants were taken to be temperature dependent as

$$k_{\pm} = k_{ref,\pm} \exp\left(-\frac{\Delta G_{0,\pm}}{R}\left[\frac{1}{T_{ref}} - \frac{1}{T}\right]\right) = k_{ref,\pm} \exp\left(-\frac{nFE_{0,\pm}}{R}\left[\frac{1}{T_{ref}} - \frac{1}{T}\right]\right) \quad (46)$$

where  $\Delta G_{0,\pm} = nFE_{0,\pm}$  is the standard Gibbs free energy change and  $k_{ref,\pm}$  is the value of  $k_{\pm}$  at  $T_{ref}$  which is the reference temperature. For OER, the Butler–Volmer expression was given as

$$j_+ = a\varepsilon(1-\alpha_g)Fk_+ \sqrt{c_{V^{4+}}^s c_{V^{5+}}^s} \left[ \exp\left(\frac{F\eta_+}{2RT}\right) - \exp\left(-\frac{F\eta_+}{2RT}\right) \right] \quad (47a)$$

$$j_- = a\varepsilon(1-\alpha_g)Fk_- \sqrt{c_{V^{3+}}^s c_{V^{2+}}^s} \left[ \exp\left(-\frac{F\eta_-}{2RT}\right) - \exp\left(\frac{F\eta_-}{2RT}\right) \right] \quad (47b)$$

Tafel equation was also used to describe the corresponding current density of the oxygen evolution at the positive electrode as follows

$$\nabla \cdot \vec{j}_{O_2} = -a\varepsilon(1-\alpha_g)j_{0,O_2} \exp\left(-\frac{F\beta_{O_2}\eta_{O_2}}{RT}\right) \quad (48)$$

where  $j_{0,O_2}$  represents the current density related to the oxygen evolution, which was taken as

$$j_{0,O_2}(T) = j_{0,O_2}(T_{ref}) \exp\left(-\frac{\Delta G_{0,O_2}}{R}\left[\frac{1}{T_{ref}} - \frac{1}{T}\right]\right) \quad (49a)$$

$$= j_{ref,O_2} \exp\left(\frac{nFE_{0,O_2}(T_{ref})}{R}\left[\frac{1}{T_{ref}} - \frac{1}{T}\right]\right) \quad (49b)$$

where  $\beta_{O_2}$  is the transfer coefficient,  $\Delta G_{0,O_2} = -4FE_{0,O_2}$  is the standard Gibbs free energy change  $T_{ref}$  is the reference temperature, and  $\eta_{O_2}$  is the overpotential for oxygen evolution reaction. The overall current density used at the positive electrode was then given as the summation of current density of OER and that of the redox reactions, expressed as

$$\nabla \cdot \vec{j} = \nabla \cdot \vec{j}_+ + 4\nabla \cdot \vec{j}_{O_2} = j_+ + j_{O_2} \quad (50)$$

Results from the model simulations show oxygen evolution contributes to a drop in battery current efficiency from about 95% (without considering OER) to 88% (with OER), which is closely similar to the 10% current efficiency drop as indicated by the mathematical model developed by Tang et al.<sup>[109a]</sup> Such decrease in current efficiency is simply due to the partly consumption from the current in the positive half-cell originally meant for the effective oxidization of  $V^{4+}$ . The volume and rate of oxygen evolution were also stated to increase with operating temperature, irrespective of other parameters. It is thus meaningful to investigate more effective approaches to predict the influence, and minimize OER through more detailed modeling frameworks, especially at the micro scale level.

### 3.2.7. Multiscale Modeling

As result of the multiple processes involved in the operation of flow batteries, a multiscale model that combines continuum models at macroscale with material and structural properties at pore-scale is required to simultaneously resolve physicochemical processes at both levels.<sup>[29b,138]</sup> To this effect, Bao et al.<sup>[139]</sup> recently established a multiscale modeling framework where an XTEK 225 microcomputed tomography (CT) system capable of providing 1  $\mu\text{m}$  resolution was applied to capture the geometrical information of porous electrode toward optimizing the inlet flow rate of a VRFB. Flow transport through the porous regions in the positive electrode with the electrochemical reactions in the VRFB was simulated using LBM, and quasi-Monte Carlo (QMC) technique was used to sample about 130 pore-scale flow and reactions. A deep neural network, coupled with the multiscale model, was trained and accurately tested using the pore-scale simulations to provide the relationship between

electrode reactions at the pore-scale level and the operating conditions of the battery at device or macroscale level. The multiscale model therefore provides a time-variant optimization of electrolyte flow rate which minimize electrolyte pump power consumption without deteriorating the power supply for discharge process. Unlike the common constant flow rate strategy, the simulation results indicate that the system efficiency of the VRFB is enhanced by more than 5%. Therefore, this model framework provides a reliable direction to design and examine the microstructure of battery components and optimize operating conditions of flow batteries. While more multiscale modeling studies are still needed for investigating the several parameters and operating characteristics in VRFBs, this novel concept should also be extended to other flow battery systems.

### 3.2.8. Other Recent Modeling Studies on VRFBs

The issues addressed, modeling concepts adopted, and simulation results from some of the recent modeling of VRFBs not covered in the sections above are summarized in **Table 2**.

## 4. Soluble Lead–Acid Flow Batteries

Another flow battery of interest that has received a considerable number of research publications is the soluble lead–acid flow battery (SLFB), following the current advances toward

improving the all-round performance of flow batteries while reducing their capital costs. The SLFB concept introduced in 2004 by Pletcher et al.<sup>[17,140]</sup> motivated several research designs and outcomes which further justify the battery system as a viable option for large-scale energy storage applications. Just like the VRFB, the SLFB makes use of a single element, Pb as the electroactive specie, exploiting its three major oxidation states Pb, Pb<sup>2+</sup>, and Pb<sup>4+</sup> (PbO<sub>2</sub>). In contrast to the conventional lead–acid batteries, SLFBs utilize an environmentally friendly electrolyte, methanesulfonic acid solution (CH<sub>3</sub>SO<sub>3</sub>H), which facilitates the solubility of Pb<sup>2+</sup> and therefore avoid complex electrode reactions. A detailed study on the engineering and performance differences between conventional lead acid battery and SLFB was reported in ref. [141], showing the superior characteristics of the latter. One of the prominent characteristics of the lead flow battery is the excellent discharge rate unaccompanied by voltage loss or system damage.<sup>[17,141]</sup> SLFBs are also different from other flow batteries in that they employ one electrolyte solution in a storage tank and their structural design requires no membrane, thereby reducing not only the structural complexity but also transport processes and cost.<sup>[17,140]</sup> However, Krishna et al.<sup>[142]</sup> recently investigated the cycling performance of a SLFB that incorporates a membrane in its configuration and operation. Despite the few enhancement studies in the energy efficiency and cyclability of this flow battery,<sup>[143]</sup> the commercialization of SLFBs is still plagued by limited cycle-life, currents leakage, incomplete dissolution of electroactive species at both electrodes during discharge, tendency of Pb dendritic formation particularly at the negative half-cell causing

**Table 2.** Summary for other recent application of modeling technology on VRFBs.

S/No	Year	Length scale	Focus	Modeling approach	Ref.
1.	2015	Macroscopic continuum model	Ion concentration and ion mobility	<ul style="list-style-type: none"> <li>– 2D, transient model iteratively solved by finite-element method</li> <li>– Correlate and determine ion mobility and concentrations using Stokes–Einstein relationship</li> </ul>	[203]
2.	2015	Lump parameter model	Aging prediction	<ul style="list-style-type: none"> <li>– Multiphysics model, solved in MATLAB/Simulink, combining thermal, electrochemical, mechanical models, and prominent battery characteristics</li> </ul>	[204]
3.	2016	Lump parameter model	Effects of flow rate, high SOC, and input current on a plug flow reactor representing a VRFB	<ul style="list-style-type: none"> <li>– Dynamic model for a single cell with VRFB cell and two electrolyte storage tanks as subsystems</li> <li>– Model solved with MATLAB ODE solver</li> </ul>	[205]
4.	2016	Macroscopic continuum model	Carbon paper-based electrodes	<ul style="list-style-type: none"> <li>– 3D, nonisothermal transient model solved in FLUENT, using the user-defined functions</li> <li>– Compared with conventional carbon felt-based electrode</li> </ul>	[206]
5.	2017	Lump parameter model	Influence of copper current collector in plug flow reactor VRFB	<ul style="list-style-type: none"> <li>– Equivalent electric circuit model extended to a 1D electrochemical model</li> </ul>	[207]
6.	2017	Empirical model	Electrolyte flow distributions and volumetric flow penetration at the interfacial region between flow channel and electrode	<ul style="list-style-type: none"> <li>– 2D model solved using COMSOL Multiphysics</li> <li>– Compared the flow distributions in plug and parabolic flow inlet boundary conditions</li> </ul>	[208]
7.	2019	Lump parameter model	Electrolyte transport delay in multistack VRFBs	0D dynamic model incorporating transport delay in multistack battery module	[209]
8.	2020	Macroscopic continuum model	Impact of electrode thickness and porosity on VRFB performance	3D model solved in COMSOL Multiphysics	[210]
9.	2020	Macroscopic continuum model	Uniformity of transfer current density	3D transient model solved in COMSOL Multiphysics	[211]

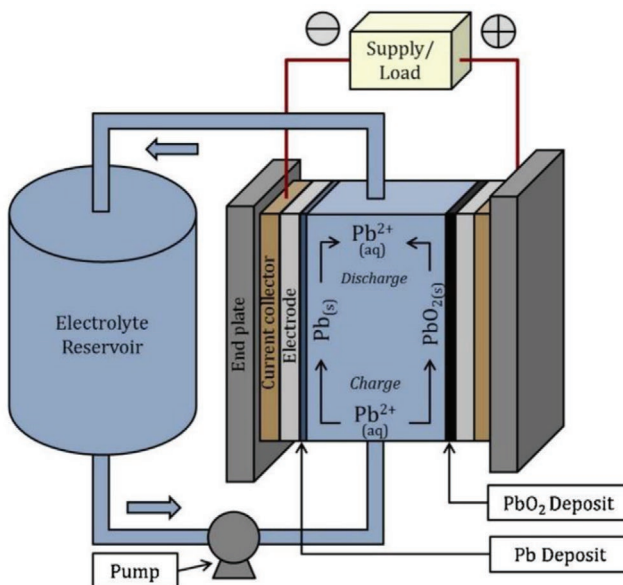


**Figure 19.** Schematic of a soluble lead flow battery showing its design components and electrode reactions. Reproduced with permission.<sup>[24]</sup> Copyright 2017, Elsevier.

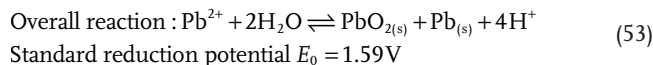
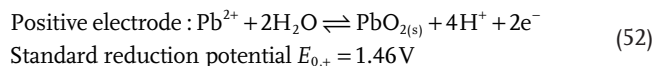
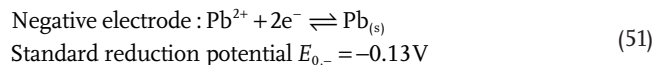
short-circuit, and ultimately the sluggish reaction kinetics and reversibility rate at the positive half-cell.<sup>[142,143b,144,145]</sup> The modeling and simulation of the charge/discharge behavior and other processes in SLFB is thus important to investigate these issues, which in turn facilitate the optimization of the battery system.

#### 4.1. Working Principle

The architectural design of a typical SLFB shown in **Figure 19** simply consists of a positive as well as a negative side, interconnected through an external load supply. Planar electrode materials from which Pb and PbO<sub>2</sub> can be reversibly deposited and removed are commonly employed in SLFBs.<sup>[141]</sup> As mentioned above, the battery system does not encompass any ion exchange membrane or porous separator between the positive and negative electrodes, hence a single electrolytic solution of Pb<sup>2+</sup> dissolved in aqueous methanesulfonic acid is circulated round the undivided flow cell to serve both electrode reactions. This therefore cut down the pumping system and its corresponding pumping energy consumption. Moreover, the electrode reactions of SLFBs is different from those of conventional lead-acid batteries as solid lead sulfate is never produced at the electrode surface of the former. It is worth to note that not all the electroactive species in SLFBs are soluble, thus the battery operation involves the deposition and dissolution of solid phases.

The redox couples at the negative electrode of a SLFB are Pb<sup>2+</sup> and Pb, while Pb<sup>2+</sup> and PbO<sub>2</sub> participates in the redox reactions on the positive electrode. During the charge cycle at the positive electrode, Pb<sup>2+</sup> are oxidized through the loss of two electrons. As a consequence, a phase change take place which deposit the resulting solid lead oxide PbO<sub>2</sub> on the electrode. Meanwhile, the donated electrons flow to the negative electrode passing through the external circuit. At the negative electrode,

these electrons reduces the Pb<sup>2+</sup> accompanied with a phase change leads to the deposition of solid Pb on the electrode surface.<sup>[141,144–145]</sup> These processes are reversed during the discharge periods, which involves the oxidation of Pb and reduction of PbO<sub>2</sub> at the negative and positive electrodes, respectively, both result to soluble lead ions Pb<sup>2+</sup> without electroactive species crossover.<sup>[12b,143b]</sup> While energy stored in a SLFB system largely depends on the thickness of the lead deposited on the surface of the electrodes,<sup>[146]</sup> the redox reaction at the positive electrode decides the energy and voltage efficiency.<sup>[147]</sup> The electrodeposition–dissolution of lead occurring at the electrodes in both half-cells, including the overall reaction are represented as follows<sup>[140,143a,144]</sup>



#### 4.2. Modeling of Soluble Lead–Acid Flow Batteries

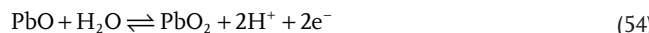
Unlike the VRFBs, the successful modelling of hybrid flow batteries including the SLFBs was not achieved on time, perhaps due to the involvement of solid or gas phases and the general complexity of the battery systems. However, Shah et al.<sup>[148]</sup> eventually formulated the first mathematical model for SLFB and reported the numerical simulation outcomes in 2010. The 2D transient model incorporated the mass and charge transport mechanisms and the electrochemical and surface reactions at electrodes. To ensure a comprehensive modeling for estimating the performance of a SLFB, the complex evolution and successive oxidation of lead oxide layer at the positive electrode was included in the model. The model simulation performed in MATLAB computational software was thereafter used to predict the concentration distribution of Pb<sup>2+</sup> and examine the charge-discharge performance of the battery at different applied current densities. The electrochemical reactions at the positive electrode from the two-steps charging approach used, particularly the oxidation of the lead oxide, was found to largely control the performance of the SLFB due to the high level of similarity between the positive electrode overpotential and the overall cell voltage. An increase in the applied current density was numerically found to result a decrease in the coulombic efficiency of the battery, which is consistent with an earlier study.<sup>[17]</sup> The model considered a possible side reaction generating PbO, however, neglected the influence of gases evolution at the electrode surface.

To better understand the influence of more operation parameters on lead deposition on the positive electrode and the overall performance characteristics of SLFBs, Bates et al.<sup>[149]</sup> performed a comprehensive numerical simulation study using COMSOL Multiphysics. The formation of multiple kinds of lead oxides as

**Table 3.** External electric potential values with change in operating cell temperature. Reproduced with permission.<sup>[149]</sup> Copyright 2013, Elsevier.

Temperature [K]	External electric potential charge [V]	External electric potential discharge [V]
300	2.15	1.54
350	2.23	1.51
400	2.27	1.47
600	2.51	1.09

side reaction at the positive electrode<sup>[148]</sup> was taken into consideration as



The effects of electrolyte flow rates, operating cell temperature, initial concentration of electroactive species, and applied current density were numerically investigated. An increase in the electrolyte flow rate from 0.01 to 0.2 ms<sup>-1</sup> was observed to drastically reduce the concentration of lead deposition, especially at the positive electrode. As other issues could be associated with this, it highlights the significant impacts of flow rates on lead deposition and the need for optimal flow rate of electrolytes in SLFBs operation. Regarding performance with varying operating temperature as seen in **Table 3**, the electric voltage increases with temperature under the charging cycle but markedly decreases during discharge. While the variation in initial species concentration has little or no effect on the surface concentration of PbO<sub>2</sub> at discharge, an increase in the initial concentration value of H<sup>+</sup> and Pb<sup>2+</sup> in the electrolyte increases and reduces the surface concentration of PbO. The concentration of both lead oxides at the positive electrode was found to increase at high applied current densities and decrease with low current densities. Consistent with the modeling result of Shah et al.,<sup>[148]</sup>

**Table 4.** External electric potential values with respect to applied current densities. Reproduced with permission.<sup>[149]</sup> Copyright 2013, Elsevier.

Applied current density [mA cm <sup>-2</sup> ]	External electric potential charge [V]	External electric potential discharge [V]
10	2.02	1.62
15	2.09	1.60
20	2.16	1.56
25	2.25	1.51
15 (experimental)	2.102	1.685

the overall cell voltage during the charging process but experience a drop at discharge when high current density is applied. The reverse trend is case with low current density as shown in **Table 4** and **Figure 20**. The study apparently shows the significance of variation in the operating conditions of a SLFB not only to regulate Pb deposition on the electrode but also to gain insight on optimizing these parameters for battery longevity.

The residual builds up on electrode surface resulting from the incomplete dissolution of is one of the major challenges leading to severe capacity degradation in SLFBs. Nandanwar and Kumar<sup>[150]</sup> therefore successful developed a mathematical model to investigate this phenomenon and their resulting effects on the battery performance. A nonuniform current density on electrode surface and electrolyte flow was included in the modeling framework in order to capture the deposition of nonuniform active materials on the electrodes. The numerical simulation of the modeling geometry which involved planar electrodes performed in COMSOL Multiphysics revealed the incremental thickness of the concentration boundary layer in the direction of electrolyte flow as a major cause of nonuniform residual formation. The deposited residues were also found to increase with subsequent charge–discharge processes which results to cell voltage drop. Some parameter designs of the

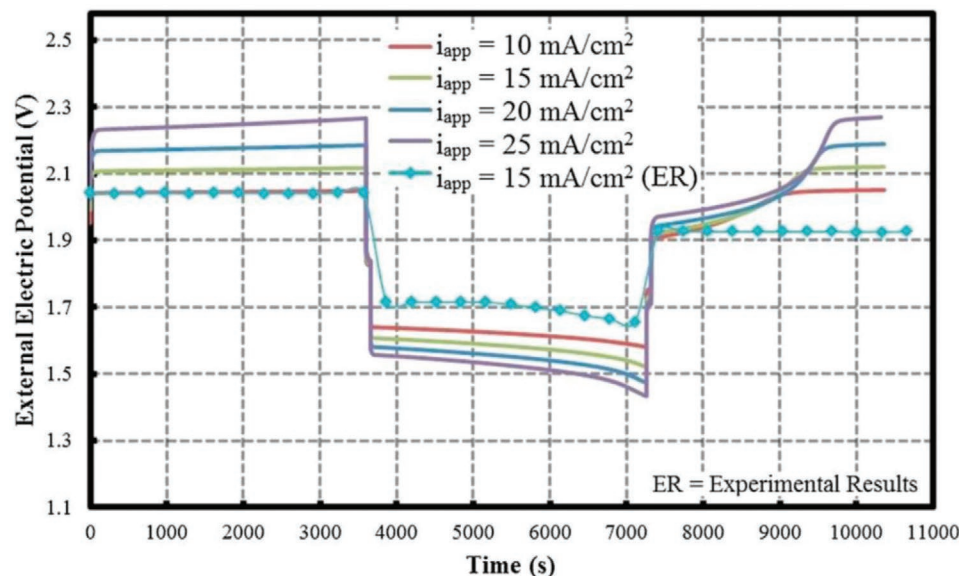


**Figure 20.** Simulated external electric potential at different applied current density, with a plot from experimental data. Reproduced with permission.<sup>[149]</sup> Copyright 2013, Elsevier.

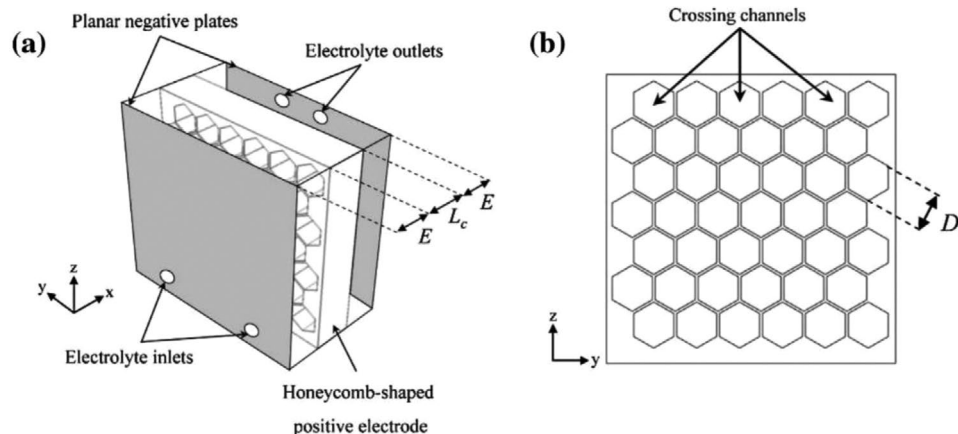


**Figure 21.** a) Schematic of the single-cell reactor housing a honeycomb-structured positive electrode placed between two planar negative electrodes. b) Front view of the honeycomb-shaped matrix. Reproduced with permission.<sup>[153]</sup> Copyright 2013, Elsevier.

flow battery were modified via reversing the flow direction and replacing the planar electrode with cylindrical electrodes. The simulation results show that reversed direction of flow substantially decrease the rate of residue deposit at the positive electrode while cylindrical electrodes improves the cell voltage as well as the energy efficiency of the battery system. The authors further developed a mathematical model, in addition to their experimental study, to unravel charge coup de fouet phenomenon in a SLFB driven by an induced natural convection.<sup>[151]</sup> The charge coup de fouet phenomenon, which reportedly also occurs in conventional lead acid batteries, is the sharp voltage drop that follows an initial voltage rise when charging a fully discharged battery. The magnitude of this behavior alongside its variation with discharge depth not only suggests the needs for more charging of battery, but also indicates the state of the health of such battery.<sup>[152]</sup> The model accurately captured the charge coup de fouet phenomenon by incorporating varying conductivity of PbO and PbO<sub>2</sub> deposits on the positive electrode and further gave more insight on the proportional relationship of the phenomenon with depth of discharge. The model results further emphasized their previous research outcomes<sup>[150]</sup> that residual specie deposits exist on the positive electrode during the discharge cycle.

To better address the slow kinetic and reversible reactions noticeable at the positive electrode of SLFBs, Oury et al.<sup>[153]</sup> designed a novel reactor which features new electrode morphology such that a honeycomb-like positive electrode is placed in between two conventional planar negative electrodes as shown in **Figure 21**. The need for an enhanced electrode structure for operating the battery system at low current density toward minimizing the charge transfer overvoltage from the positive electrode reaction motivated the innovative design. The authors further performed a stationary 2D numerical simulation to study the influence of the new structure and its dimensions on the charge–discharge behavior of the system.<sup>[153]</sup> The geometry of the new positive electrode largely influenced the current distribution in the electrode with little effects from electrolyte flow. With consideration of a number of electrolyte compositions, electrolyte contents of high H<sup>+</sup> and low Pb<sup>2+</sup> produced a moderately high cell voltage during the charging

period and also reduced overvoltage during discharge. Apparently, there is a need for more analysis and evaluations of the new cell reactor design and operations, particularly regarding the deficient dissolution of lead dioxide.

While most of the available SLFB models neglected the influence of free convection and its dynamic velocity field,<sup>[148–150,153]</sup> Nandanwar and Kumar<sup>[154]</sup> recently combined and modified their previously developed models<sup>[150–151]</sup> to concurrently investigate the influence of both forced and free convections on the performance behavior of the battery system. The velocity field was therefore integrated with the concentration field. The new model established the dominance of free convection, which better facilitates fluid flow, ions transport to the electrodes, and electrode kinetics, as the major determinant of the battery characteristics. As a consequence, the limit current density doubles that of forced convection. The model thus clearly explains the outcome of a previous experimental study<sup>[155]</sup> that the charge efficiencies of the battery system during charge cycles are more than those of the theoretical limit. It is worth to know that due to limited movement of Pb<sup>2+</sup> unlike H<sup>+</sup> during charging, free convection has more effects on the charge process. The simulation results also revealed that operating the battery at a low electrolyte flow rate has almost no effect on its performance, thereby reducing pumping energy consumption and cost. While there is still need for more modeling approaches for the design and optimization advancement of SLFBs, this latest model framework can be adopted to better develop and understand other hybrid flow batteries which involves similar mechanisms.

## 5. Semisolid Flow Batteries

The semisolid flow battery (SSFB) is an innovative electrochemical energy storage concept proposed and developed toward augmenting the limited energy density prevalent among the existing flow battery technologies. The first of its kind developed by Duduta et al.<sup>[21]</sup> successfully combined the high energy density attribute of a rechargeable lithium-ion battery with the flexible configuration design of a conventional flow battery,

thus exhibiting as high as 500 Wh L<sup>-1</sup> energy density. Apart from Lithium, other alkali metallic ions like sodium and Potassium are also suitable for this purpose owing to their similar chemical properties.<sup>[156]</sup> SSFB design not only enables high energy density, but also employs cheaper materials and construction cost than the common lithium-ion batteries. However, the complexity of the fundamental processes and the formation of solid electrolyte interphase,<sup>[157]</sup> which obstructs charge transfer between current collector and semisolid electrodes, are critical issues confronting SSFBs. Attaining an optimal regulation of suspension viscosity and flow distribution in SSFB is another challenge to its overall performance as well as commercialization.

### 5.1. Working Principle

In a typical SSFB shown in **Figure 22**, the electrolyte is a multiphase particle suspension which can either be aqueous<sup>[156b,158]</sup> or nonaqueous,<sup>[156a,159]</sup> usually transported to the active site of solid electrodes to jointly form flow or slurry electrode, yet conducting electrons. Energy is therefore stored in the non-Newtonian suspension to and from which charge transfer reactions take place.<sup>[21,156b]</sup> Continuous flow and intermittent flow conditions are the two major modes of operating SSFB. The continuous flow ensures constant flow of suspensions during the battery operations, whereas the intermittent mode requires suspension renewal at the end of every charge–discharge cycle. Due to the higher charging capacity of the solid portion of the suspension, the energy density of SSFB is at least ten times more than that of conventional redox batteries.<sup>[21]</sup>

### 5.2. Modeling of Semisolid Flow Batteries

Over the years, the influence of flow rate and transport mechanisms, kinetic operations coupled with the electrochemical phenomena within SSFBs have been described and analyzed

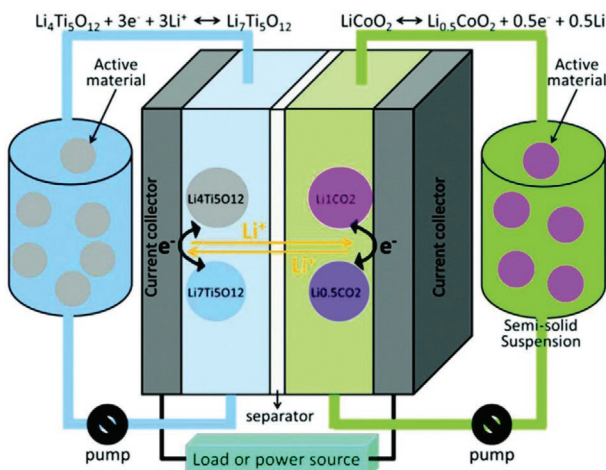


**Figure 22.** Schematic diagram illustrating the basic reactions in a typical semisolid flow battery. Reproduced according to the terms of the CC-BY-NC license.<sup>[157]</sup> Copyright 2015, RSC.

by few model-based studies.<sup>[156b,160]</sup> The Navier–Stokes equation for an incompressible non-Newtonian fluid is generally used in modeling the suspension flow together with a power law viscosity in SSFB

$$\rho \left( \frac{\partial \vec{u}}{\partial t} + \vec{u} \cdot \nabla \vec{u} \right) = -\nabla p + \nabla \cdot (\mu (\nabla \vec{u} + (\nabla \vec{u})^T)) \quad (55)$$

where  $\rho$  is the fluid density,  $\vec{u}$  the fluid velocity,  $p$  the pressure, and  $\mu$  power law viscosity expressed as

$$\mu = C \gamma^{n-1} \quad (56)$$

where  $C$  is the viscosity coefficient,  $\gamma$  the shear stress, and  $n$  viscosity exponent.

The premier modeling of a SSFB was implemented in 2012 by Brunini et al.<sup>[160a]</sup> to investigate the influence of electrochemical couple on the hydrodynamic performance and electrochemical efficiency of SSFB. To achieve their objective, a 3D model and a 1D model of lithium-ion based SSFB were developed and results from the numerical simulations of both models were compared. It was established that uniform current distribution and stoichiometric flow in SSFB largely depends on the cell voltage against state of charge relationship. Electrochemical couples involving lithium ion electrodes such as  $\text{Li}_4\text{Ti}_5\text{O}_{12}$  and  $\text{LiFePO}_4$ , were found to usually attain high cell efficiency. This is because such battery system produces flat polarization curve as shown in **Figure 23**, which not only enhances uniform current, but also gives enough room for complete charge and discharge cycles. Conversely, SSFB based on storage compound  $\text{LiCoO}_2$  exhibits high variance cell potential with the state of charge.

In addition to experimental demonstrations, Li et al.<sup>[156b]</sup> developed a computational model to explore rheology and its effects on the energy efficiency of an aqueous SSFB. Plug flow, slow flow rates and a pumping volume control (aliquot factor) were identified and emphasized as significant variables of the non-Newtonian suspensions in SSFB toward maximizing round-trip energy efficiency. The electrochemical performance of SSFBs therefore largely depends on its rheology. To further explore the SSFB, Lacroix et al.<sup>[160c]</sup> recently performed a modelling work to study the rheological and electrochemical performance of two SSFBs with suspension-based

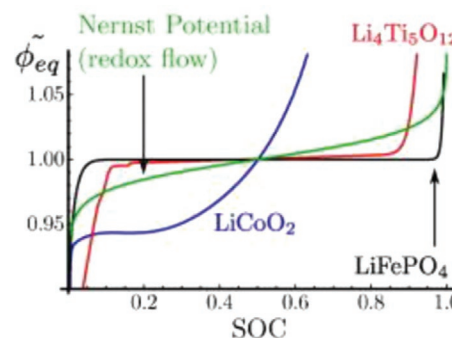


**Figure 23.** Equilibrium cell voltage against state of charge of three different electrochemical couples. Reproduced with permission.<sup>[160a]</sup> Copyright 2012, Elsevier.

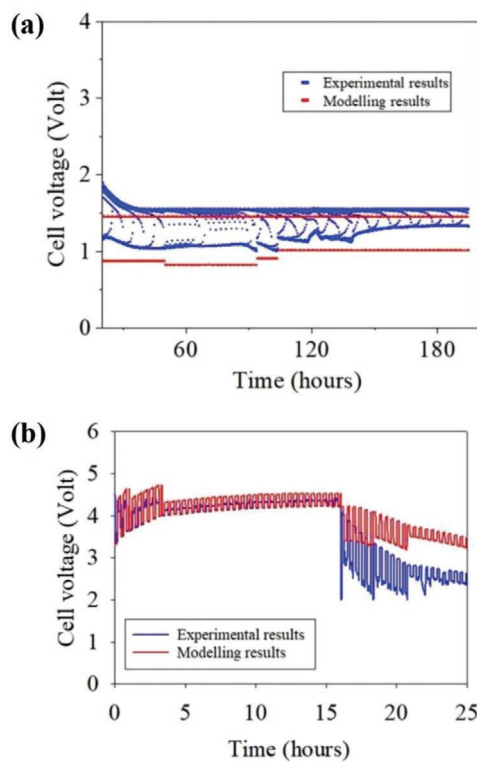
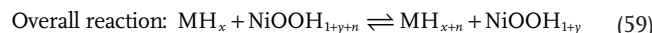
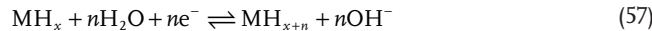


**Figure 24.** Comparison of the simulation results with experimental data for the a) LTO and b) LNMC-based suspensions. Reproduced with permission.<sup>[160c]</sup> Copyright 2019, Elsevier.

$\text{Li}_4\text{Ti}_5\text{O}_{12}$  (LTO) and  $\text{LiNi}_{1/3}\text{Co}_{1/3}\text{Mn}_{1/3}\text{O}_2$  (LNMC), respectively, each against lithium metal. Lithium ions diffusion in the active particles of both lithium storage compounds were estimated using a microscopic modelling approach. However, the potential and current distribution, flow velocity and pressure, and evolution of state of charge were all calculated at macroscopic level. For the rheology analysis, the simulation demonstrated good agreement with the experimental values and indicated pressure drops below 5000 Pa, and a comparatively homogenous velocity profiles for both suspensions. Adjusting the flow rate was further stated to rarely affect such pressure drop in the reaction channel. However, the comparison of the simulation results and experimental data of the cell potential notably shows significant differences as shown in **Figure 24**. Change in internal cell resistance and electrochemical stability both with respect to time was expressed as the reason for such differences in the case of LTO-based suspension. On the other hand, the reason for the cell potential deviation in LNMC was not explicitly mentioned. The authors, however, promised to further the study to give more clarifications on it.

More recently, Chayambuka et al.<sup>[160b]</sup> demonstrated the right modeling method of accounting for the kinetic and transport processes in SSFBs following the observed transport mechanism misconception in previous macroscopic model studies.<sup>[156b,160a]</sup> The multiscale transient model thus considered molecular diffusion as the only transport process which takes place inside the solid active materials and that the mass

transport of these particles does not relate to the diffusion. In contrast to previous SSFB studies which are based on Lithium materials, the model was applied to nickel-metal hydride (NiMH) SSFB which utilizes potassium hydroxide electrolyte. The charge and discharge reactions at the anode and cathode sides, respectively, are shown as



The NiMH SSFB was first modeled without considering the suspension flow using a pseudo 2D model. Afterward, a pseudo 3D model of a flowing SSFB was used to examine the battery transient voltage with respect to discharge time. The two models gave a better understanding of the differences as well as the similarities between the operation characteristics of flowing and nonflowing SSFBs. From the pseudo 3D model, a Ragone plot shown in **Figure 25**. was presented. Operating the battery under fast flow rates of flowing particles was concluded to be more superior to low flow rates. While complex operational designs are associated with low flow operation mode; fast flow rates enhance power output and improves discharge rates of the battery system. The numerical model and simulation clearly predict the interconnection between the rheology and electrochemical performance of SSFBs, thereby aiding the rational design of more viable SSFB chemistries.

A mechanistic modeling approach involving parameter sensitivity analysis and graph theory was also developed for understanding and quantifying the complexity and dynamic behavior of SSFBs.<sup>[161]</sup> Apart from the rheology of multiphase suspension, the lithiation rate of electroactive particles and some other phenomena were captured by the Monte Carlo-based model. In agreement with other modeling techniques, the systematic

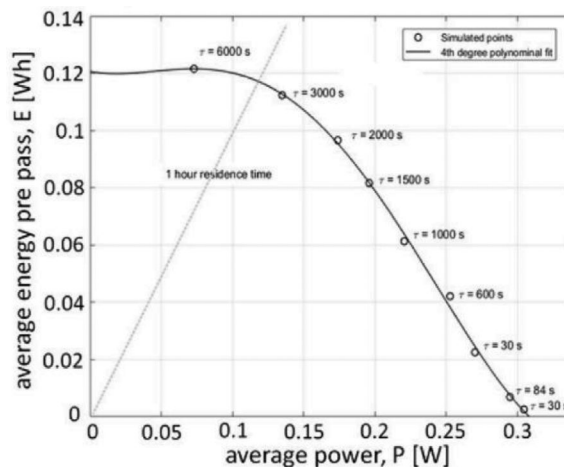


**Figure 25.** Ragone plot of the NiMH SSFB indicating the high energy and power derived from a single pass at different flow residence times. Reproduced with permission.<sup>[160b]</sup> Copyright 2019, Elsevier.

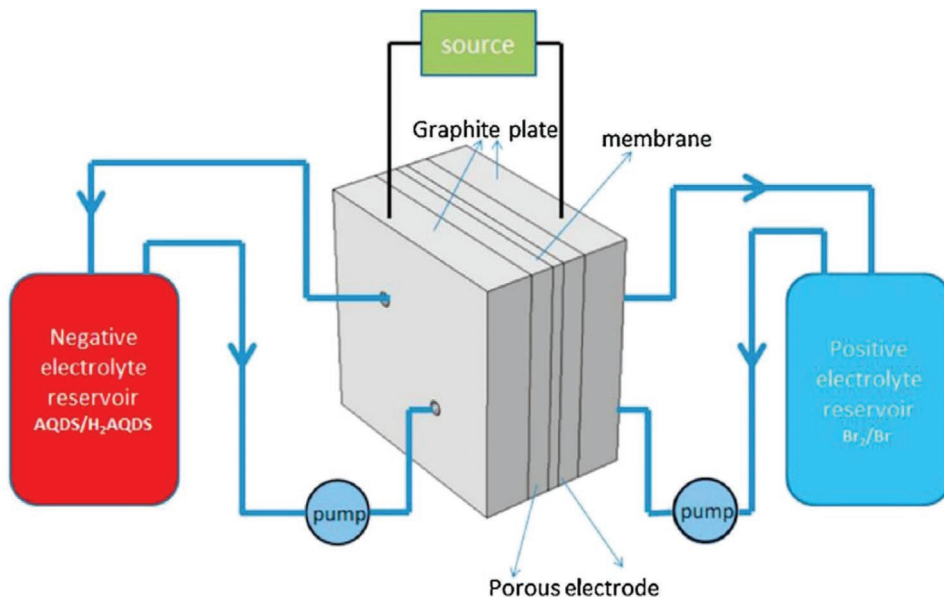


**Figure 26.** Schematic of a metal-free Organic-inorganic (quinone–bromide) flow battery. Reproduced with permission.<sup>[166b]</sup> Copyright 2015, Elsevier.

method consistently validates the existence of interdependent parameters and phenomena revealing the competitive and dominating variables. This new concept of modeling the complex SSFBs also give room to categorize and reduce the impact of different phenomena which consequently simplify the entire system.

## 6. Organic Flow Batteries

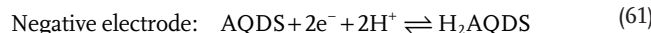
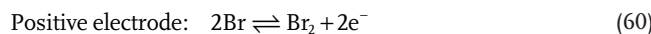
Organic flow battery technology was proposed as an alternative energy storage options with the aim to overcome the solubility issues common in metal-based flow batteries, and therefore achieve increase in energy density.<sup>[162]</sup> In terms of cost, to substitute the use of expensive metallic elements as the electroactive species in flow battery electrolytes. Some of the organic flow batteries specially utilize complex organic molecules or compounds derived from natural sources as their electroactive species, while others use ligand-controlled transition metals which are dissolvable in either aqueous or nonaqueous electrolytes. The abundance of organic substances, high structural flexibility, diverse redox potentials, and low-capital cost are some of the advantages for introducing organic materials into flow battery systems.<sup>[9c,25,163]</sup> They are therefore expected to be promising candidates for clean and sustainable energy storage systems. Over the years, numerous forms of organic flow batteries have been proposed and developed by different researchers.<sup>[162c,164]</sup> Some aspects of organic flow batteries still require improvements such as establishing novel organic couples for higher cell potential and improved charge storage capacity, boosting organic molecules stability and voltage window, optimization of pump consumption, and the development of suitable electrode and membranes for different organic flow battery chemistries.<sup>[163]</sup> Till date, most of the studies on the performance analysis of organic flow batteries are based on experiments.

### 6.1. Working Principle

A number of redox-active organic molecules, which are either based on aqueous or nonaqueous electrolytes, have been employed in the operation of organic flow battery technology. Furthermore, the electroactive species in organic flow battery can either be metal-free organic active species or metal-involved organic active species.<sup>[25,163b]</sup> Hence the working principle of any organic flow battery system largely depends on the electrolyte system together with the electroactive materials similar to VRFBs, with the difference that some organic flow batteries, especially the ones with metal-free organic active species, involves the transfer of more than one electron. Quinone-bromide flow battery shown in **Figure 26.** is one of the organic flow batteries that has received a considerable research attention, particularly by Aziz and his research group.<sup>[162a,165]</sup>

### 6.2. Modeling of Organic Flow Batteries

To shed more light on the operation and performance of organic molecule-based flow batteries, only two model-based studies have been carried out over the years.<sup>[166]</sup> Following the demonstration of quinones and their derivatives<sup>[162a,167]</sup> as suitable candidates for low-cost organic flow batteries, the first numerical model which describes a quinone–bromine flow battery using quinone/hydroquinone redox couple at the negative side and bromine Br<sub>2</sub>/Br<sup>-</sup> at the positive side as follows<sup>[166a]</sup>



A 3D model domain as shown in **Figure 27** with a flow through electrode configuration was developed to examine the

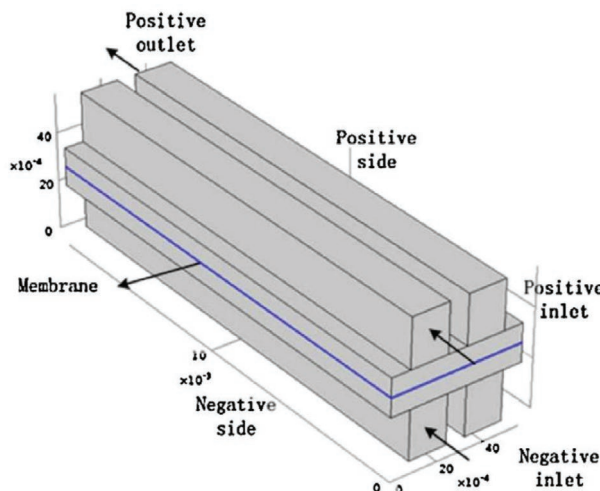


**Figure 27.** A 3D modeling domain of a quinone–bromide flow battery. Reproduced with permission.<sup>[166a]</sup> Copyright 2015, Elsevier.

impacts of electrode thickness on the operation characteristics of a quinone–bromide flow battery. The numerical simulations identified 6 layers of carbon paper as the most suitable electrode thickness for the metal-free organic–inorganic flow battery. Another highlight of the study is the improvement of a previous electrolyte conductivity equation<sup>[81]</sup>

$$\sigma_{\text{pre}} = \frac{F^2}{RT} \sum_i z_i^2 D_i c_i \quad (62a)$$

by introducing a correction coefficient  $k$  given as

$$k = \frac{\sigma_{\text{measured}}}{\sigma_{\text{pre}}} \quad (62b)$$

The resulting polarization curves from the previous and corrected electrolyte conductivity equations were compared as shown in **Figure 28** alongside with the result from an experimental data unlike the previous model, the inclusion of the correction coefficient  $k$  makes the polarization trend calculated by the corrected equation fits with the experimental data.

The scope of this modeling framework<sup>[166a]</sup> was later extended through the consideration of the effects of more operational variables on the charge and discharge behavior of the organic flow battery system.<sup>[166b]</sup> The improved model lay much emphasis on the effects of graphite plates and flow channels on current distribution and the influence of temperature, different applied current densities and time-dependent variables such as flow rate on the cell performance. From the range of applied current densities considered in the simulation as shown in **Figure 29**, lower values were found to improve the battery operation via the reduction of charging voltage and its corresponding electric energy consumption, while boosting discharge voltage and energy. At such low current density, the magnitude of flow rates has no influence on the battery operations, which in turn promotes the usage of low flow rates

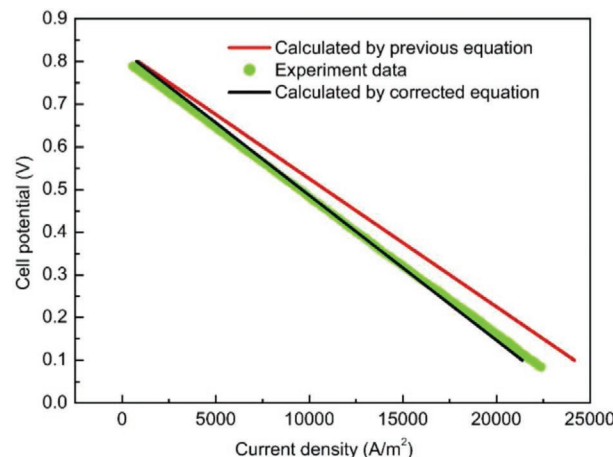


**Figure 28.** Comparison of the resulting polarization curves from the previous and corrected electrolyte conductivity equations with results from an experimental study. Reproduced with permission.<sup>[166a]</sup> Copyright 2015, Elsevier.

to minimize pump consumption. But at low current density, slow reaction and cycling rates tend to happen. Hence, a trade-off between this occurrence and operating current density is needed. Regarding the effect of temperature, the cell voltage and overpotential increase in tandem with temperature to a certain level as seen in **Figure 30** where elevating the temperature will have little or no effect on the battery performance. It is therefore essential to effectively regulate the thermal unit of the organic flow battery, particularly during its charge and discharge cycles. Both numerical studies thus provide fundamental guide for further research and development toward the rational design and advancement of organic flow battery systems.

## 7. Zinc Nickel Flow Batteries

The zinc nickel flow battery was introduced by Cheng et al.<sup>[168]</sup> as a single flow battery system, with a simplified stack design

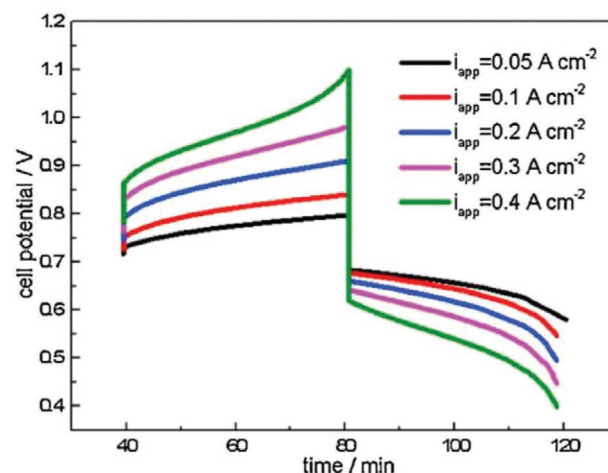


**Figure 29.** The simulated charge–discharge curves of a metal-free quinone–bromide for five different applied current densities. Reproduced with permission.<sup>[166b]</sup> Copyright 2015, Elsevier.

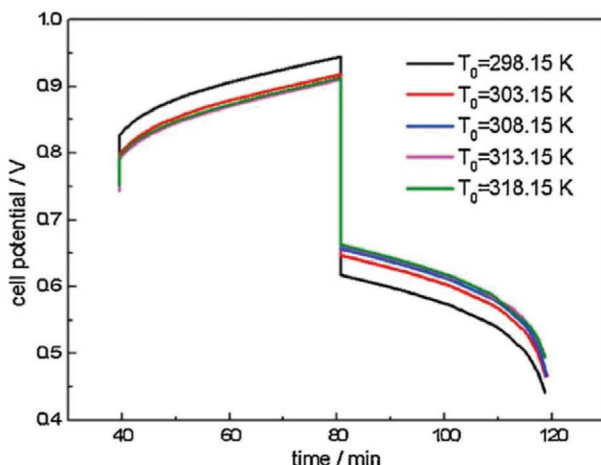


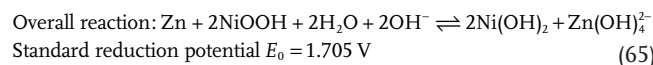
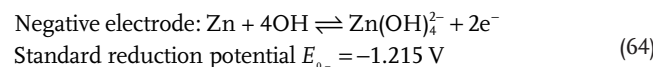
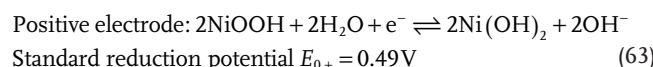
**Figure 30.** The Simulated charge–discharge curves of a metal-free quinone–bromide for five different temperature levels. Reproduced with permission.<sup>[166b]</sup> Copyright 2015, Elsevier.

without a membrane, suitable for scaled energy storage at reduced capital cost. Flowing electrolyte was primarily integrated into the conventional zinc-based batteries to revamp their mass transfer process, subdue internal short circuit and also to prolong the battery cycle life. The advantages of the developed zinc nickel flow battery, which include high voltage window, high efficiency, and low cost, has therefore presented the battery system as a propitious energy storage option for enhancing the effective use of renewable energy resources. Large polarization, with its adverse effects of low power density, has plagued the performance of zinc nickel flow batteries. However, with the various improvements in cell configuration,<sup>[169]</sup> electrode structure<sup>[170]</sup> and electrolyte composition and additives,<sup>[171]</sup> significant reduction in the polarization has been achieved at high current density up to  $80 \text{ mA cm}^{-2}$  without compromising the battery efficiencies. Other exigent challenges on the market penetration of zinc nickel flow batteries include poor kinetic reactions and cycling instability at the positive electrode lowering both power and current densities, dendrite formation, and zinc accumulation at the negative electrode, reduction of the area capacity of the negative electrode, requirement of large areal nickel electrode, parasitic side reactions and corrosion of nickel electrodes, and short life cycle from possible heterogeneous reactions.<sup>[26,169–172]</sup> Numerical investigation of these issues and their effects on the charge–discharge behavior and other processes in the battery system is thus important.

### 7.1. Working Principle

**Figure 31** shows the basic structure of a typical zinc nickel flow battery and its major components include the cell stack, pump/hydraulic system, and storage tank. The positive electrode of the battery uses nickel hydroxide, the negative electrode employs an inert metallic conductor, and the circulating electrolyte is a concentrated solution of zinc oxide dissolved in an aqueous alkaline (KOH) medium.<sup>[171]</sup> The electrolyte, driven by the pump, flows in between the tank and stack during the charge and discharge processes while redox reactions take place

on the surface of the two electrodes. At discharge,  $\text{NiOOH}$  is reduced to  $\text{Ni(OH)}_2$  on the positive electrode whereas at the negative side, metallic zinc is oxidized to zincate. The reverse reaction occurs during the charging periods. Consequently, the reactions at the positive half-cell ends with solid phase forming solid to solid electrode reaction. On the other hand, simultaneous deposition and dissolution of zinc occurs at the negative electrode.<sup>[26,171,173]</sup> As a zinc-based hybrid flow battery, the cycle life of the battery depends on the reactions at negative electrode as the zinc deposition–dissolution can be endlessly continuous. The general characteristics of separate and independent power and energy module of flow batteries is therefore not applicable to zinc-based flow batteries due to the poor surface area from zinc dendrite on the negative electrode.<sup>[26,174]</sup> This phenomenon also occurs in zinc–bromine flow batteries discussed in subsequent sections. The electrochemical reactions at the positive and negative electrodes are given as follows<sup>[172]</sup>



### 7.2. Modeling of Zinc Nickel Flow Batteries

Asides the innovative model predictive control strategy developed for monitoring the working conditions, estimating the state of charge and battery capacity, and identifying reconditioning moments for zinc nickel single flow batteries,<sup>[175]</sup> most model numerical investigations on the dynamic operations of the battery have been majorly carried out by Yao and

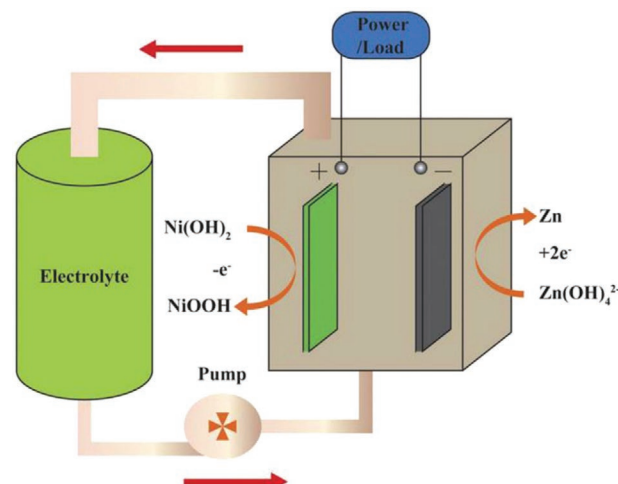


**Figure 31.** Schematic of a zinc nickel flow battery. Reproduced under the terms of the CC-BY license.<sup>[176b]</sup> Copyright 2017, The Authors.

his research team in China.<sup>[176]</sup> Yao et al.<sup>[176g]</sup> first developed a 3D model to describe the internal reaction and transport phenomena in a zinc nickel flow battery. Afterward, they developed a mechanical model of the pump system in addition to an electrochemical model of cell-stack to study the influence of electrolyte flow on the performance of zinc nickel flow battery.<sup>[176a]</sup> The simulation results show that stack voltage demonstrate linear changes under the steady state but becomes nonlinear at the end of charge and discharge due to the effect of temperature and zinc deposition. Flow rate between 0.06 and 0.08 L s<sup>-1</sup> was suggested by the simulation as the optimal electrolyte flow rate for the battery. An equivalent circuit model of the battery was later built to indicate model parameters via pulse experiment in order to solve parameters estimation problems.<sup>[176b]</sup> The identified parameters were then used to develop a mathematical model to simulate the cell voltage at discharge. The accuracy of the parameter fitting method, when compared to experiment result, show that it is an effective approach to further improve the modeling and simulation processes of zinc nickel flow battery. Another mathematical model of zinc nickel flow battery was developed by the same research team to study the effect of variation of ion concentration, electrode over potential and equilibrium potential with respect to time.<sup>[176c]</sup> The influence of all these operation parameters and more on a 23 cell-stacked zinc nickel flow battery were also numerically examined.<sup>[176h]</sup>

A more comprehensive model, validated against experimental data, was also established by Yao et al.<sup>[176d]</sup> to study the discharge process of zinc nickel flow battery. The 2D model investigated the effects of changes in hydroxide ions and zinc ions concentration, applied current density, and electrolyte flow rate on the discharge voltage. Increase in the initial concentration of hydroxide ion and zinc ions lead to an increase and slight decrease in the cell voltage, respectively. A higher current density increases the polarization of the reaction and therefore increases the transfer current density and the over-potential. The cell voltage of zinc nickel flow battery at discharge slightly increase with flow rate. The results obtained are consistent with similar studies performed with the all-vanadium redox flow battery.<sup>[83,85]</sup> The model was further extended to study the examine the impacts of self-discharge on the battery operations.<sup>[176e]</sup> Side reaction at the negative electrode was found to dominate the self-discharge process with drastic impacts on the battery voltage. More recently, lattice Boltzmann method was applied to study the transport phenomenal in porous electrodes of a zinc nickel flow battery. Based on this, numerical simulations of a 2D model of the positive electrode were performed to evaluate the structural characteristics and the electrochemical mechanism of the electrode.<sup>[176f,i]</sup> The influence of inlet flow rates, charging current density, as well as porosity on percolation velocity and mass transfer through the porous electrode were also investigated and discussed. The modeling frameworks provide necessary foundation for advance researches in improving the structure and performance of electrode materials for zinc nickel flow battery. Based on the previous studies of the team on zinc nickel flow battery, they further developed an equivalent circuit model using Simulink in MATLAB to predict the charge–discharge characteristics of the battery stack.<sup>[176j]</sup> Then, the effects of a range of constant currents on the performance of the stack were simulated. While the coulombic efficiency increases with increase in current magnitude

due to a lesser time to complete a charge–discharge process; stack voltage, voltage efficiency, and energy efficiency all reduce with the rise in charge–discharge current as a result of concentration overpotential arising from slow diffusion rate. Apparently, consistent progress has been made in providing references for further research and development on the design optimization and operating conditions control of zinc nickel flow battery.

## 8. Zinc–Bromine Flow Batteries

The zinc–bromine flow battery (Zn/Br) is another zinc-based hybrid flow battery system introduced in 1977.<sup>[177]</sup> It is an attractive energy storage system suitable for large-scale practical applications due to its intrinsic and simple chemical reactions, excellent electrochemical reversibility, high energy density (70 Wh kg<sup>-1</sup>), abundant and inexpensive reactant materials. The high energy density of the battery is attributed to high solubility of bromine in electrolyte and reaction with complexing agent. The utilization of the same electroactive species in both half-cells of the battery eliminates cross contamination issues. As a result of these intriguing features, Zn/Br flow battery has been installed for some real-world commercial utilizations in different countries.<sup>[173,178]</sup> Despite the promising prospects of Zn/Br flow battery, a number of issues with the redox couples still need to be overcome. For example, the environmental risk associated with bromine, diffusion of Br<sub>2</sub>, the formation and accumulation of zinc dendrite, low reaction kinetics of the bromine species, and low power density.<sup>[19,26,178–179]</sup> Therefore, studies on how to address these issues have become necessary for further research and development of the battery. In addition to experimental studies toward improving the cell performance, mathematical models have also been developed to optimize the various operating conditions and parameter designs.

### 8.1. Working Principle

A typical zinc–bromine flow battery shown in Figure 32. Employs zinc bromide solution as electrolyte in both positive and negative half-cells. The electrochemical reactions involve the reduction of

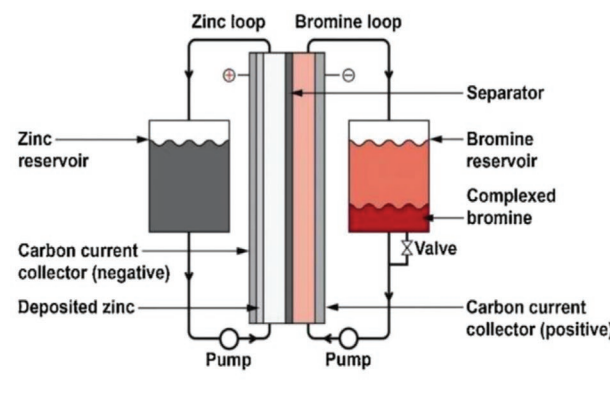
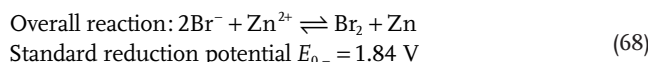
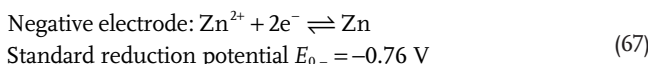
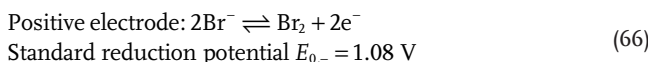


**Figure 32.** A schematic of a typical zinc–bromine flow battery and its components. Reproduced under the terms of the CC-BY license.<sup>[202]</sup> Copyright 2017, The Authors.

zinc ion to metallic zinc and the oxidation of bromide ion to bromine at the negative and positive electrodes, respectively, during charging, while the discharge process involves the anodic dissolution of zinc and cathodic formation of Br at the negative and positive electrodes, respectively, as described below<sup>[173,180]</sup>



## 8.2. Modeling of Zinc–Bromine Flow Batteries

Mathematical models for investigating various aspects of zinc–bromine flow battery have been developed since the early 80s. Evans and White<sup>[181]</sup> summarized most of these early model-based studies. In 2010, a zinc–bromide flow battery of high energy and power density coupled with high efficiency was tested and modeled for application in hybrid electric vehicles.<sup>[182]</sup> The results show that the internal resistance of the battery as well as the open-circuit voltage are dependent on the state of charge of battery. Kalman filtering method was then employed to regulate the state of charge toward enhancing the performance of the battery. Koo et al.<sup>[183]</sup> also performed a modeling study to estimate current distribution and predict the operational behavior of zinc–bromine flow cell during charge and discharge process. A simple modeling technique previously employed in the analysis of lithium-ion battery performance was adopted.<sup>[184]</sup> In addition to the charge and discharge characteristics, voltage, current and energy efficiencies of an 8-cell stack zinc–bromine flow battery at different discharge currents was accurately predicted by the model as shown in Figure 33. The model serves as a valuable tool to improve the design of cells-stacked flow batteries in achieving operating modes for optimal performance. Xu et al.<sup>[185]</sup> developed a more sophisticated model integrating the electrochemical reactions, mass and charge transport, and the hydraulic systems of a zinc–bromine flow battery. The

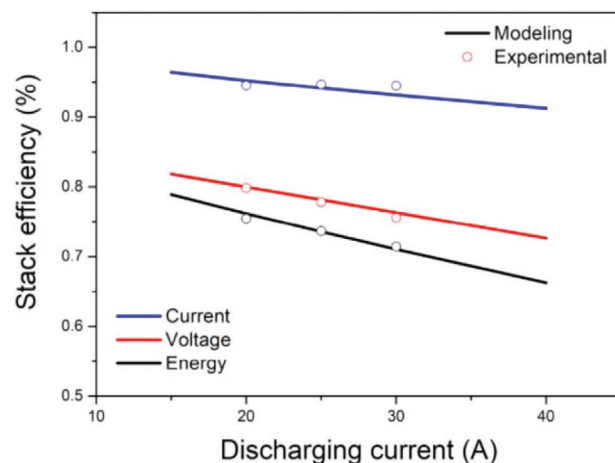


**Figure 33.** Comparison of the simulated current, voltage, and energy efficiencies with experimental data under various discharge conditions. Reproduced under the terms of the CC-BY license.<sup>[183]</sup> Copyright 2019, The Authors.

highlight of the numerical investigation is the analysis of the effects of two different flow channels structure—design 1 and design 2 with few and multiple curved flow channels, respectively, shown in Figure 34 on the flow battery performance. The mean velocity of electrolyte via both designs is almost the same, although the maximum velocity through design 2 was found to be slightly higher than that of design 1 due to small inflow area of the latter. The more curved channel structure, design 2, reduces discharge time and consequently improves discharge voltage. Both flow curvatures have little or no impact on the electrolyte current density distribution at each half-cell, however, the distribution in the membrane was nonuniform in both designs. Flow channel design also influences zinc deposition during the charge–discharge periods and design 2 shows more even distribution of the deposition on negative electrode. This hints that multiple curve channel as one of the methods of minimizing uneven zinc deposition. The comparison of the simulated coulombic, voltage and energy efficiencies obtained from zinc–bromine flow battery operated with either design is illustrated in Figure 35. While design 2 slightly improves the voltage efficiency of the battery, both coulombic and energy efficiencies were reduced. All these modeling and simulation studies can be used to further improve the design and establish comprehensive

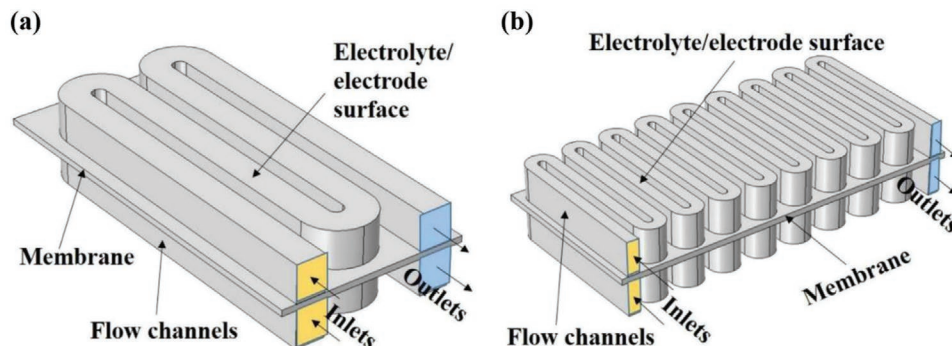


**Figure 34.** Channel designs for a zinc–bromine flow battery. a) Design 1 and b) Design 2. Reproduced with permission.<sup>[185]</sup> Copyright 2019, Elsevier.

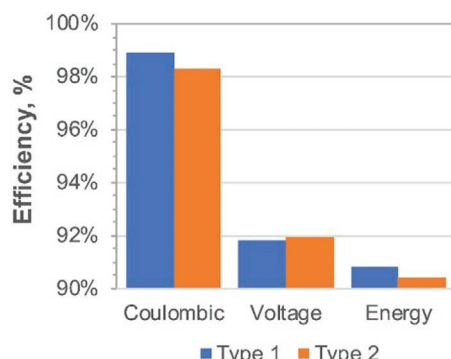


**Figure 35.** The efficiencies of a zinc–bromine flow battery with design type 1 and 2 flow channel structures. Reproduced with permission.<sup>[185]</sup> Copyright 2019, Elsevier.

understanding of zinc–bromine flow battery for varying performance requirements.

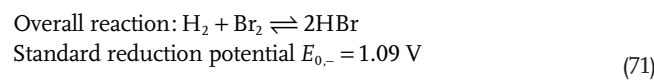
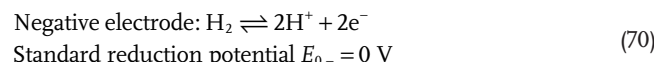
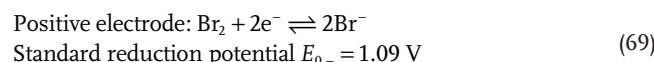
## 9. Hydrogen Bromine Flow Batteries

Hydrogen-bromine flow battery system is another interesting energy storage option first demonstrated in 1980.<sup>[186]</sup> It has then been reported as a promising candidate for large-scale storage applications due to the fast rate of its redox couples kinetic reactions, good reversibility of the electrode reactions, high energy capacity, abundance of reactants materials, excellent round-trip conversion efficiency, and low cost.<sup>[18,187]</sup> A hydrogen bromine flow battery of long cycling period exceeding 600 cycles with less capacity degradation and peak power density of about of 1.5 W cm<sup>-2</sup> was recently reported.<sup>[188]</sup> However, some of the performance limitations of the battery system include high bromine vapor pressure which must be reduced to gain practical applications, toxicity of bromine requires adequate safety measures, ohmic loss through crossover of bromine to the negative half-cell, instability of cycling process due to poisoning

and deactivation of negative electrode catalyst by bromide species, and limiting current density from the adsorption of bromide on the negative electrode.<sup>[18,188a,189]</sup>

### 9.1. Working Principle

The battery system whose operating principle is illustrated in Figure 36 consists of an electrochemical cell with circulating reactants from reservoir tanks holding hydrogen (gaseous state) at the negative side and an aqueous solution of Br<sub>2</sub>/H<sub>2</sub> at the positive compartment, both sides separated by an ion exchange membrane. However, a membraneless hydrogen bromine flow battery has been introduced.<sup>[190]</sup> The flow cell employs hydrobromide as a supporting electrolyte. At discharge, bromine solution Br<sub>2</sub> from an aqueous hydrobromide HBr is supplied into the positive half-cell of the battery where bromine reacts with protons and electrons from the negative side and in turn reduced to bromide Br<sup>-</sup>. On the other hand, a reverse in the direction of flow leads to hydrogen evolution reaction at the negative electrode and generation of Br<sub>2</sub> during charge, both from the decomposition of the hydrobromide.<sup>[189]</sup> The charge and discharge reactions occurring at both electrodes are as follows:<sup>[18,187b]</sup>



### 9.2. Modeling of Hydrogen Bromine Flow Batteries

Asides the reported mathematical models of hydrogen-bromine fuel cells,<sup>[191]</sup> researchers have also taken interest to predict,

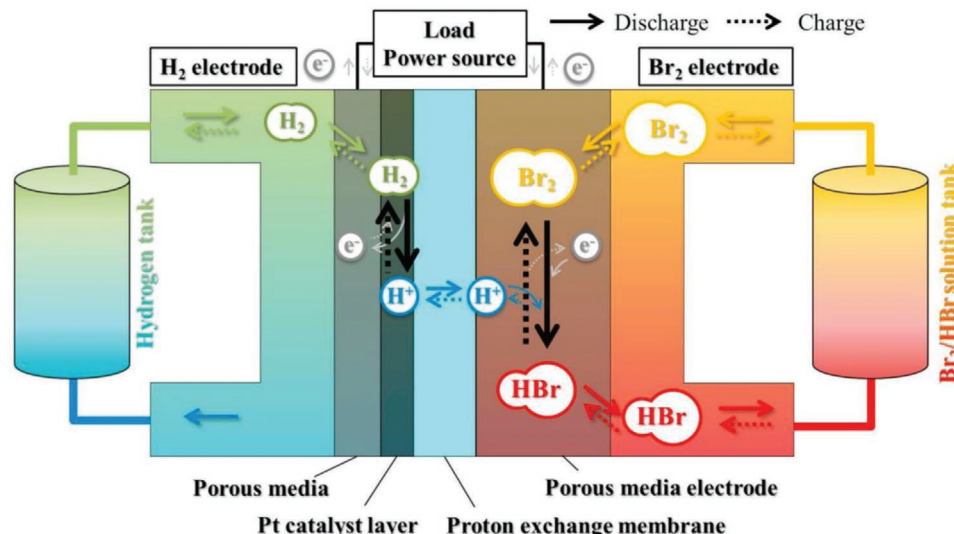
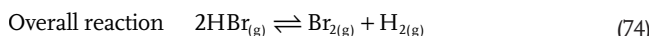
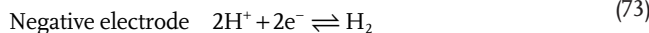
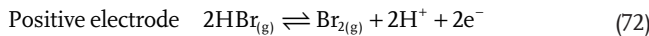


**Figure 36.** Schematic of a typical hydrogen bromine flow battery system. Reproduced with permission.<sup>[194]</sup> Copyright 2017, Elsevier.

improve and optimize the performance of hydrogen bromine flow batteries using numerical models. Due to the limited current density observed in previous liquid-based bromine flow cells, gas-phase bromine was introduced to replace the liquid-phase in the positive electrode reaction.<sup>[192]</sup> Following this, Zhang and Weidner<sup>[193]</sup> developed a mathematical model, validated against experimental data, to explore the operational processes of a gas-phase hydrogen bromine flow battery whose electrode reactions are given as follows



An important feature incorporated into model was water transport through the membrane, which provides insight on how to prevent water condensation in the flow cell. The model therefore tested the performance of the battery as a function of some operating parameters including flow rate, and pressure gradient across the separator. The results indicate that gas-phase hydrogen bromine flow battery greatly enhance mass transfer, which in turn facilitates higher current densities compared to its liquid-based counterpart. Based on one of the previous models of hydrogen-bromine fuel cell<sup>[191b]</sup>, You et al.<sup>[187b]</sup> developed a 2D modeling work to investigate the influence of electrode thickness, particularly a flow-through positive electrode, on the performance of a hydrogen bromine flow battery. This was accomplished in detail by breaking the voltage loss into three components—ohmic, activation and mass transport, during the charge and discharge processes. Considering the trade-off among the three components, the results recommended a positive electrode thickness between 2 and 3 mm for the optimum operation of hydrogen bromine flow battery. Considering the flow field design for the liquid phase electrolyte in hydrogen bromine flow battery, the suitability and efficiency of flow through and flow by designs were numerically investigated and compared.<sup>[194]</sup> The simulation of the 3D model of the battery indicate that flow through design provides more advantages and performance improvement than flow-by. Unlike the flow-by structure, the design of flow through channels give room for more uniform electrolyte flow distribution and less compression of porous media during the integration of the flow cell. As a consequence, the flow through design facilitate smooth diffusion of electroactive species through the bromine porous media and effect high convective flow of the liquid electrolyte. Ohmic loss from charge transport is therefore substantially reduced, leading to performance improvement of the battery system.

## 10. Sodium–Air Flow Batteries

The abundance of sodium offers a great prospect for an inexpensive application of the element in electrochemical energy storage devices. Sodium–air flow battery was introduced to replace and improve not only the conventional sodium–air batteries but also the existing metal–air batteries which suffer

from inadequate mass transfer and lower specific capacities at high discharge rate.<sup>[27,195]</sup> More importantly, the successful development and capacity improvement of lithium–oxygen flow battery<sup>[196]</sup> provided an insight that the use of sodium in place of lithium would offer better and higher capacity performance.

### 10.1. Working Principle

The schematic configuration of a sodium air flow battery is shown in Figure 37. The structural components and working principle are similar to the lithium–air flow battery described in refs. [196,197], except for the use of sodium at the anode in place of lithium.

### 10.2. Modeling of Sodium–Air Flow Batteries

Based on the established modeling frameworks on lithium–air flow battery,<sup>[196–197]</sup> Ranmode et al.<sup>[27]</sup> developed a microscopic model to investigate the discharge performance of sodium air flow battery. A parametric study of the influence of varying parameters, including current density and pressure gradient, on the discharge characteristics of the battery was performed. Simulation results show that the distribution of the oxygen through the cell predominantly determines the specific capacity and cell performance of the flow battery. Comparative analysis carried out shows that to the sodium–air flow battery exhibit improved oxygen transport and in turn, a higher specific capacity over the nonflow sodium–air battery due to enough flow of oxygen electrolyte at a suitable pressure gradient. Small pressure gradient was concluded to be beneficial for the sodium air flow battery at very low discharge current densities usually below  $0.05 \text{ mA cm}^{-2}$  whereas, higher pressure gradient is preferred at a relatively higher values of discharge current densities above  $0.125 \text{ mA cm}^{-2}$ . This is currently the only model-based study on sodium–air flow battery. Apparently, the developed model is a useful tool

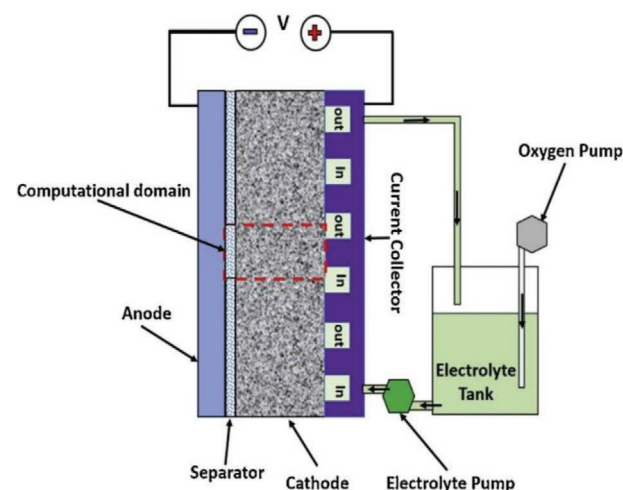
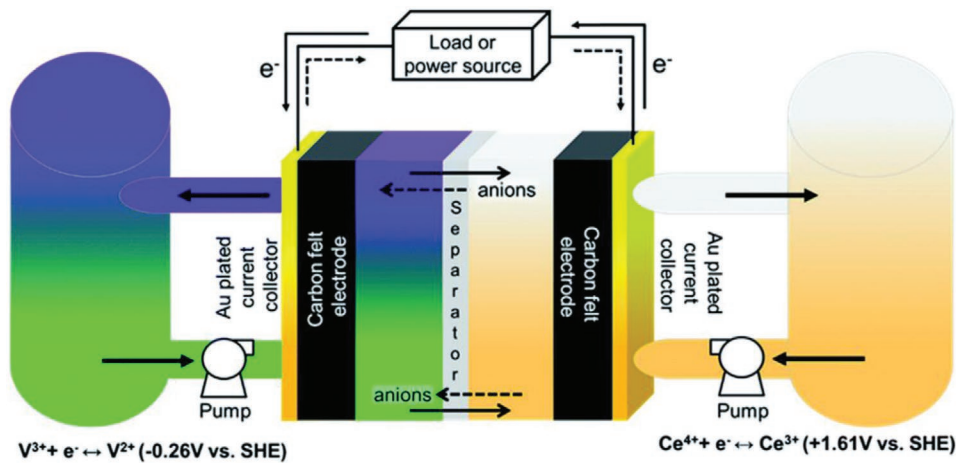


Figure 37. Schematic of a sodium air flow battery. Reproduced with permission.<sup>[27]</sup> Copyright 2019, Elsevier.



**Figure 38.** Schematic of a Vanadium–cerium flow battery showing its components. Reproduced with permission.<sup>[201]</sup> Copyright 2019, The Royal Society of Chemistry.

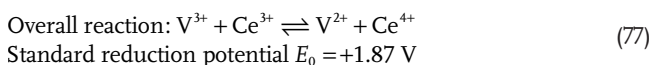
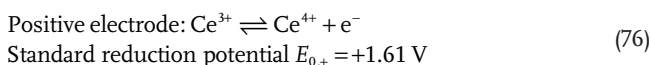
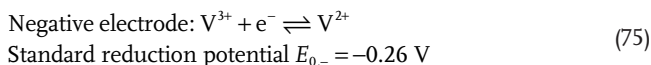
for researchers and developers to better understand and stimulate improved design and optimization of sodium air flow battery.

## 11. Vanadium–Cerium Flow Batteries

The vanadium–cerium flow battery system which combines the advantages of vanadium and cerium as suitable elements for energy storage applications was proposed in 2002<sup>[198]</sup> followed by some performance evaluations in a single acid solution.<sup>[28,199]</sup> The comparatively large gaps between the electrode potentials of both elements in aqueous solution suggests the combination as a promising system for flow battery.

### 11.1. Working Principle

Due to high redox couple potential, the cerium redox couple ( $Ce^{3+}$  and  $Ce^{4+}$ ) is used in the positive electrode reaction while vanadium ions ( $V^{2+}$  and  $V^{3+}$ ) are used as redox couple in the positive side as shown in **Figure 38**. Both redox couples in the V-Ce flow battery system are commonly dissolved in a mixed acid electrolyte solution, usually sulfuric acid and methanesulfonic acid to enhance the solubility of both elements.<sup>[200]</sup> Just as in VRFB, the state of the reacting species of vanadium–cerium flow battery does not change and only one electron-transfer occurs during the electrochemical reactions. The redox reactions in both half-cells and the overall reaction are<sup>[201]</sup>



### 11.2. Modeling of Vanadium–Cerium Flow Batteries

The first and only numerical model and simulation study on vanadium–cerium flow battery available in literature was recently carried out by Daoud and his research team.<sup>[200a]</sup> The transient model demonstrated the deviation of state of charge (SOC) and flow efficiency as novel yardsticks for assessing the durability and energy density of a flow battery system. While SOC deviation is the difference between the SOC in the two half-cells, flow efficiency refers to the means of ensuring a balance between the electrolyte flow rate and flow of current. In the mathematical model, the effect of heat transfer on the liquid in both half-cells were included. In addition, heat generated as a result of the presence of current in the electrode, electrolyte, and membrane were all considered using this equation

$$\rho C_p \partial_t T + \rho C_p \vec{v} \cdot \nabla T - k^h \nabla^2 T = S^h \quad (78)$$

where  $\rho$  is the density of material conducting heat,  $C_p$  heat capacity,  $T$  temperature,  $k^h$  thermal conductivity, and  $S^h$  heat source. The numerical study further illustrated the influence of several physical parameters including membrane thickness and electrode conductivity toward the overall performance and optimum design of the flow battery. However, more studies are still needed to improve the model accuracy and further consider other vital factors to ensure the widespread application of the flow cell.

## 12. Summary and Outlook

Flow battery technology maintains the most promising and practical option for large-scale renewable energy storage applications primarily due to its excellent energy-conversion efficiency at low cost as well as structural design flexibility for diverse electrochemical reactions and materials. In addition to resolving contradictory and seemingly difficult experimental studies, modeling technology has been progressively applied toward addressing the various critical issues hampering the

broad market penetration of flow battery systems. Through mathematical modeling and numerical simulations, improved structural design, optimization of operation parameters, performance prediction and improvement, capacity enhancement, and the formulation of more flow battery chemistries have been successfully realized. In this paper, we thus review research and development progress in the modeling and simulation of flow batteries. Unlike previous reviews, we extend the understanding of modeling efforts beyond the most studied all-vanadium redox flow battery by including and discussing soluble lead-acid, semisolid, organic, zinc-nickel, zinc bromine, hydrogen bromine, sodium-air, and vanadium-cerium flow batteries. We provide comprehensive review and state-of-the-art numerical investigations on the common all-vanadium redox flow batteries by considering improved transport phenomena, flow field structures design, control and optimization of electrolyte flow rates, minimization of shunt current, quantification, and suppression of side reactions. Moreover, we discuss the working principles, the electrochemical redox reactions, and the various modeling studies, simulation implications, and the performance trends of other flow battery chemistries mentioned above. Without doubt, there remains some pressing challenges and technical aspects of these flow batteries which are yet to be numerically explored.

Even though VRFBs have received extensive modeling research works, some of its design components such as investigating the microstructure of electrodes and membranes, and simultaneously optimizing most of the various operation conditions still requires advanced modeling frameworks beyond the existing models. To achieve rational design and development of high performance VRFBs, future modeling research should also focus on evaluating the various levels of electrochemical reactions occurring at the porous electrodes other than electrode dimensions. In lieu of modeling small-scale cells, more research attention should also focus on formulating mathematical models that adequately capture most, if not the entire, processes including the mass/charge transfer, heat transport, electrolyte flow channel and distribution, and charge-discharge behavior in a full-scale flow-cell and battery system. Reducing and reconsidering some of the commonly used assumptions and simplifications is of paramount importance to achieving a sophisticated model of the battery. Intensified efforts should be made to also enhance the energy density of VRFBs through a thorough investigation to minimize solubility issues.

The electrochemical reaction mechanisms at SLFBs electrodes, particularly the redox kinetics at the positive electrode, should be thoroughly understood. The reactions at this electrode significantly influence the efficiencies and cycle life of SLFB. Due to the complexity of reactions that take place at the positive electrode of the battery, a better and broad understanding of the optimization of the redox couple and effective strategy for minimizing accumulation of lead on the electrode is required. This can be accomplished by performing further studies to numerically investigate lead deposition-dissolution phenomena and gas evolution in the battery system.

Addressing the inadequate understanding of the slurry electrode phenomena and the influence of the electrode compositions on conductivity is especially important for improved engineering design of SSFBs. This indicates the need for new

strategies in cell geometry modeling and material properties assessment. To demystify the complexity and achieve more accurate prediction of SSFBs, mathematical modeling of active particles and suspension dynamics beyond their viscosity should be made with some suitable assumptions including the selection of current collectors which suit the fluid flow. To improve the rheology and electrochemical performance of the battery, a modeling study may explore more operational characteristics which include assessing mass transport limitations and optimizing flow field design.

Despite the numerous experimental discoveries on different types of organic flow batteries, unfortunately, only the quinone bromine flow battery has received modeling attention with limited investigations. Detailed examination of electroactive species crossover and flow channel design for quinone bromine flow battery are yet to be explored. The characteristics and performance of more organic flow battery systems are required to be theoretically predicted. This may be achieved through stack and system model under varying operating conditions to explore stack designs for simplified structural design, optimized components and reaction interface, minimized pump loss and shunt current, and extended cycle life. Addressing limited voltage window, energy density and membrane selection for nonaqueous organic flow batteries are also important for high storage efficiency, high power output and battery commercialization.

Zinc nickel and zinc bromine are the two zinc-based flow batteries discussed in this article. The operation and development of both flow battery systems encounter similar issues due to the common plating-stripping activities of zinc at their negative electrode. A better understanding of the plating-stripping on the electrode surface is needed. This would provide a sound basis for finding effective solutions to the problems associated with zinc dendrite and accumulation. Designing new membranes with high resistance to zinc dendrite effects, improving the electrolyte properties to induce zinc plating, and performing a trade-off between electrode thickness and battery size should be taken into consideration in ameliorating this issue. Better still, an innovative design of zinc-based battery configuration that would effectively accommodate zinc dendrites without compromising high potential and current density would significantly increase the utilization of these batteries. For zinc-bromine flow batteries, future research should also focus on preventing bromine emission and  $\text{Br}_2$  crossover across membrane, improving the kinetics at the bromine reactions at the positive electrode and developing high performance complexing agents. Regarding zinc nickel flow batteries, their performance improvement specially needs the design and development of positive electrode material of equal surface area with the negative material to achieve homogeneous electrochemical reaction, augment power density and regulate parasitic side reactions in the battery.

The key issue in hydrogen bromine flow batteries is the undesired crossover of bromine across membrane to the negative half-cell. Such bromine transport not only result in ohmic losses but also deactivate the negative electrode catalyst and its adsorption on the electrode leads to limiting current density. It is therefore critical to investigate the dominant mechanisms of bromine transport to gain insight on how to optimize

the transport process and further improve the cycle life of the battery. A comprehensive study and analysis of the roles and effects of complexing agents on vapor pressure of bromine, safety, performance, and characteristics of membrane and the entire battery system should also be considered.

The development and performance evaluation of sodium-air and vanadium–cerium flow batteries is at its nascent stage, both with limited studies. Hence there is enough room to explore and optimize the design components, influence of different operating conditions, charge–discharge performance, and other significant processes and phenomena pertaining to each battery. To facilitate rapid development, capacity enhancement and commercialization success of sodium–air and vanadium–cerium flow batteries, both experimental and modeling approaches are ultimately required. Due to similar electrode reaction with VRFB, vanadium–cerium flow battery is expected to receive more research focus, replicating most of the existing investigations on VRFBs. Following this, advancement and wide applications of flow battery technology will be achieved.

## Acknowledgements

The work described in this paper was fully supported by a grant from the Research Grant Council of the Hong Kong Special Administrative Region, China (Project No. T23-601/17-R).

## Conflict of Interest

The authors declare no conflict of interest.

## Keywords

battery performance, flow batteries, modeling, simulation, system optimization

Received: February 27, 2020

Revised: April 30, 2020

Published online: June 8, 2020

- [1] a) R. C. Armstrong, C. Wolfram, K. P. De Jong, R. Gross, N. S. Lewis, B. Boardman, A. J. Ragauskas, K. Ehrhardt-Martinez, G. Crabtree, M. Ramana, *Nat. Energy* **2016**, *1*, 15020; b) M. Armand, J.-M. Tarascon, *Nature* **2008**, *451*, 652; c) D. Larcher, J.-M. Tarascon, *Nat. Chem.* **2015**, *7*, 19; d) S. Chu, A. Majumdar, *Nature* **2012**, *488*, 294.
- [2] a) M. Carabajales-Dale, C. J. Barnhart, S. M. Benson, *Energy Environ. Sci.* **2014**, *7*, 1538; b) O. Schmidt, A. Hawkes, A. Gambhir, I. Staffell, *Nat. Energy* **2017**, *2*, 1.
- [3] a) S. Chu, Y. Cui, N. Liu, *Nat. Mater.* **2017**, *16*, 16; b) J. W. Ager, A. A. Lapkin, *Science* **2018**, *360*, 707; c) R. M. Darling, K. G. Gallagher, J. A. Kowalski, S. Ha, F. R. Brushett, *Energy Environ. Sci.* **2014**, *7*, 3459; d) D. Rekioua, *Hybrid Renewable Energy Systems*, Springer, Berlin, Germany **2020**, Ch. 4, p. 139.
- [4] a) S. Hameer, J. L. van Niekerk, *Int. J. Energy Res.* **2015**, *39*, 1179; b) H. Chen, T. N. Cong, W. Yang, C. Tan, Y. Li, Y. Ding, *Prog. Nat. Sci.* **2009**, *19*, 291; c) J. M. Tarascon, M. Armand, *Nature* **2001**,

- 414, 359; d) V. Aravindan, Y. S. Lee, S. Madhavi, *Adv. Energy Mater.* **2015**, *5*, 1402225.
- [5] G. L. Soloveichik, *Annu. Rev. Chem. Biomol. Eng.* **2011**, *2*, 503.
- [6] M. Skyllas-Kazacos, M. H. Chakrabarti, S. A. Hajimolana, F. S. Mjalli, M. Saleem, *J. Electrochem. Soc.* **2011**, *158*, R55.
- [7] S. Dutta, *J. Ind. Eng. Chem.* **2014**, *20*, 1148.
- [8] a) M. Li, J. Lu, Z. Chen, K. Amine, *Adv. Mater.* **2018**, *30*, 1800561; b) R. Van Noorden, *Nature* **2014**, *507*, 26.
- [9] a) L. Thaller, *Patent US3996064 1976*; b) M. Bartolozzi, *J. Power Sources* **1989**, *27*, 219; c) M. L. Perry, A. Z. Weber, *J. Electrochem. Soc.* **2016**, *163*, A5064.
- [10] L. H. Thaller, *Google Patents*, **1976**.
- [11] a) Y. K. Zeng, T. S. Zhao, L. An, X. L. Zhou, L. Wei, *J. Power Sources* **2015**, *300*, 438; b) X. Ke, J. M. Prahl, J. I. D. Alexander, J. S. Wainright, T. A. Zawodzinski, R. F. Savinell, *Chem. Soc. Rev.* **2018**, *47*, 8721; c) C. Zhang, L. Zhang, Y. Ding, S. Peng, X. Guo, Y. Zhao, G. He, G. Yu, *Energy Storage Mater.* **2018**, *15*, 324.
- [12] a) C. P. De Leon, A. Frías-Ferrer, J. González-García, D. Szántó, F. C. Walsh, *J. Power Sources* **2006**, *160*, 716; b) A. Z. Weber, M. M. Mench, J. P. Meyers, P. N. Ross, J. T. Gostick, Q. Liu, *J. Appl. Electrochem.* **2011**, *41*, 1137.
- [13] a) P. Leung, X. Li, C. Ponce de León, L. Berlouis, C. T. J. Low, F. C. Walsh, *RSC Adv.* **2012**, *2*, 10125; b) B. Dunn, H. Kamath, J.-M. Tarascon, *Science* **2011**, *334*, 928; c) H. M. Zhang, *ECS Trans.* **2010**, *22*, 1; d) M. V. Holland-Cunz, F. Cording, J. Friedl, U. Stimming, *Front. Energy* **2018**, *12*, 198; e) T. Nguyen, R. F. Savinell, *Electrochem. Soc. Interface* **2010**, *19*, 54.
- [14] a) A. Poullikkas, *Renewable Sustainable Energy Rev.* **2013**, *27*, 778; b) B. Li, J. Liu, *Natl. Sci. Rev.* **2017**, *4*, 91.
- [15] a) M. Skyllas-Kazacos, F. Grossmith, *J. Electrochem. Soc.* **1987**, *134*, 2950; b) M. Rychcik, M. Skyllas-Kazacos, *J. Power Sources* **1988**, *22*, 59.
- [16] M. Lopez-Atalaya, G. Codina, J. R. Perez, J. L. Vazquez, A. Aldaz, *J. Power Sources* **1992**, *39*, 147.
- [17] D. Pletcher, R. Wills, *Phys. Chem. Chem. Phys.* **2004**, *6*, 1779.
- [18] G. Lin, P. Y. Chong, V. Yarlagadda, T. Nguyen, R. Wycisk, P. Pintauro, M. Bates, S. Mukerjee, M. Tucker, A. Weber, *J. Electrochem. Soc.* **2016**, *163*, A5049.
- [19] M. C. Wu, T. S. Zhao, H. R. Jiang, Y. K. Zeng, Y. X. Ren, *J. Power Sources* **2017**, *355*, 62.
- [20] W. Wang, V. Sprenkle, *Nat. Chem.* **2016**, *8*, 204.
- [21] M. Duduta, B. Ho, V. C. Wood, P. Limthongkul, V. E. Brunini, W. C. Carter, Y.-M. Chiang, *Adv. Energy Mater.* **2011**, *1*, 511.
- [22] a) M. Ulaganathan, V. Aravindan, Q. Yan, S. Madhavi, M. Skyllas-Kazacos, T. M. Lim, *Adv. Mater. Interfaces* **2016**, *3*, 1500309; b) K. Lourenssen, J. Williams, F. Ahmadpour, R. Clemmer, S. Tasnim, *J. Energy Storage* **2019**, *25*, 100844.
- [23] a) Q. Zheng, X. Li, Y. Cheng, G. Ning, F. Xing, H. Zhang, *Appl. Energy* **2014**, *132*, 254; b) Á. Cunha, J. Martins, N. Rodrigues, F. P. Brito, *Int. J. Energy Res.* **2015**, *39*, 889; c) P. Alotto, M. Guarneri, F. Moro, *Renewable Sustainable Energy Rev.* **2014**, *29*, 325.
- [24] M. Krishna, E. Fraser, R. Wills, F. Walsh, *J. Energy Storage* **2018**, *15*, 69.
- [25] P. Leung, A. A. Shah, L. Sanz, C. Flox, J. R. Morante, Q. Xu, M. R. Mohamed, C. Ponce de León, F. C. Walsh, *J. Power Sources* **2017**, *360*, 243.
- [26] Z. Yuan, Y. Yin, C. Xie, H. Zhang, Y. Yao, X. Li, *Adv. Mater.* **2019**, *31*, 1902025.
- [27] V. Ranmode, J. Bhattacharya, *J. Energy Storage* **2019**, *25*, 100827.
- [28] B. Fang, S. Iwasa, Y. Wei, T. Arai, M. Kumagai, *Electrochim. Acta* **2002**, *47*, 3971.
- [29] a) W. Liu, W. Lu, H. Zhang, X. Li, *Chem. - Eur. J.* **2019**, *25*, 1649; b) Q. Xu, T. S. Zhao, *Prog. Energy Combust. Sci.* **2015**, *49*, 40;

- c) B. Huskinson, S. Nawar, M. R. Gerhardt, M. J. Aziz, *ECS Trans.* **2013**, *53*, 101.
- [30] P. Tan, W. Kong, Z. Shao, M. Liu, M. Ni, *Prog. Energy Combust. Sci.* **2017**, *62*, 155.
- [31] A. Seaman, T.-S. Dao, J. McPhee, *J. Power Sources* **2014**, *256*, 410.
- [32] a) J. Sánchez-Monreal, P. A. García-Salaberri, M. Vera, *Appl. Energy* **2019**, *251*, 113264; b) L. An, Z. H. Chai, L. Zeng, P. Tan, T. S. Zhao, *Int. J. Hydrogen Energy* **2013**, *38*, 14067; c) L. An, R. Chen, *Appl. Therm. Eng.* **2017**, *124*, 232.
- [33] a) G. F. Castelli, W. Dörfler, *Comput. Math. Appl.* **2019**, *77*, 1527; b) S. S. Madani, E. Schaltz, S. K. Kær, *Energies* **2019**, *12*, 679.
- [34] a) W. Xiao, L. Tan, *Renewable Energy* **2019**, *133*, 1445; b) A. Tang, J. McCann, J. Bao, M. Skyllas-Kazacos, *J. Power Sources* **2013**, *242*, 349.
- [35] K. N. Grew, W. K. Chiu, *J. Power Sources* **2012**, *199*, 1.
- [36] a) S. Shi, J. Gao, Y. Liu, Y. Zhao, Q. Wu, W. Ju, C. Ouyang, R. Xiao, *Chin. Phys. B* **2016**, *25*, 018212; b) A. Xu, W. Shyy, T. Zhao, *Acta Mech. Sin.* **2017**, *33*, 555.
- [37] J. Pan, X. Xie, J. Wang, S. Wang, Y. Shang, T. Zhou, *CIESC J.* **2011**, *62*, 7.
- [38] a) X. L. Zhou, T. S. Zhao, L. An, Y. K. Zeng, L. Wei, *J. Power Sources* **2017**, *339*, 1; b) G. L. Soloveichik, *Chem. Rev.* **2015**, *115*, 11533.
- [39] a) K. J. Kim, M.-S. Park, Y.-J. Kim, J. H. Kim, S. X. Dou, M. Skyllas-Kazacos, *J. Mater. Chem. A* **2015**, *3*, 16913; b) R. M. Darling, M. L. Perry, *J. Electrochem. Soc.* **2014**, *161*, A1381; c) Q. Xu, T. S. Zhao, *Phys. Chem. Chem. Phys.* **2013**, *15*, 10841; d) D. You, H. Zhang, J. Chen, *J. Electroanal. Chem.* **2009**, *625*, 165.
- [40] a) B. R. Chalamala, T. Soundappan, G. R. Fisher, M. R. Anstey, V. V. Viswanathan, M. L. Perry, *Proc. IEEE* **2014**, *102*, 976; b) X. Zhou, T. Zhao, L. An, Y. Zeng, L. Wei, *J. Power Sources* **2017**, *339*, 1.
- [41] M. H. Chakrabarti, N. P. Brandon, S. A. Hajimolana, F. Tariq, V. Yufit, M. A. Hashim, M. A. Hussain, C. T. J. Low, P. V. Aravind, *J. Power Sources* **2014**, *253*, 150.
- [42] a) X. L. Zhou, Y. K. Zeng, X. B. Zhu, L. Wei, T. S. Zhao, *J. Power Sources* **2016**, *325*, 329; b) X. L. Zhou, T. S. Zhao, Y. K. Zeng, L. An, L. Wei, *J. Power Sources* **2016**, *329*, 247; c) Q. Wu, Y. Lv, L. Lin, X. Zhang, Y. Liu, X. Zhou, *J. Power Sources* **2019**, *410–411*, 152; d) P. Han, H. Wang, Z. Liu, X. Chen, W. Ma, J. Yao, Y. Zhu, G. Cui, *Carbon* **2011**, *49*, 693; e) P. Han, Y. Yue, Z. Liu, W. Xu, L. Zhang, H. Xu, S. Dong, G. Cui, *Energy Environ. Sci.* **2011**, *4*, 4710.
- [43] a) G. Qiu, C. R. Dennison, K. W. Knehr, E. C. Kumbur, Y. Sun, *J. Power Sources* **2012**, *219*, 223; b) D. Zhang, Q. Cai, O. O. Taiwo, V. Yufit, N. P. Brandon, S. Gu, *Electrochim. Acta* **2018**, *283*, 1806; c) D. Maggioli, F. Zanini, F. Picano, A. Trovo, S. Carmignato, M. Guarneri, *Energy Storage Mater.* **2019**, *16*, 91; d) A. G. Lombardo, B. A. Simon, O. Taiwo, S. J. Neethling, N. P. Brandon, *J. Energy Storage* **2019**, *24*, 100736; e) S. J. Yoon, S. Kim, D. K. Kim, *Energy* **2019**, *172*, 26.
- [44] a) G. Qiu, A. S. Joshi, C. R. Dennison, K. W. Knehr, E. C. Kumbur, Y. Sun, *Electrochim. Acta* **2012**, *64*, 46; b) L. Chen, Y. He, W.-Q. Tao, P. Zelenay, R. Mukundan, Q. Kang, *Electrochim. Acta* **2017**, *248*, 425; c) R. Banerjee, N. Bevilacqua, L. Eifert, R. Zeis, *J. Energy Storage* **2019**, *21*, 163; d) M. D. Kok, R. Jervis, T. G. Tranter, M. A. Sadeghi, D. J. Brett, P. R. Shearing, J. T. Gostick, *Chem. Eng. Sci.* **2019**, *196*, 104.
- [45] a) K. Bromberger, J. Kaunert, T. Smolinka, *Energy Technol.* **2014**, *2*, 64; b) Q. Wang, Z. Qu, Z. Jiang, W. Yang, *Appl. Energy* **2018**, *220*, 106; c) K. Oh, S. Won, H. Ju, *Electrochim. Acta* **2015**, *181*, 13.
- [46] a) P. Leung, T. Martin, A. Shah, M. Anderson, J. Palma, *Chem. Commun.* **2016**, *52*, 14270; b) P. K. Leung, T. Martin, A. A. Shah, M. R. Mohamed, M. A. Anderson, J. Palma, *J. Power Sources* **2017**, *341*, 36;
- [47] a) Y. Shi, C. Eze, B. Xiong, W. He, H. Zhang, T. Lim, A. Ukil, J. Zhao, *Appl. Energy* **2019**, *238*, 202; b) W. Lu, Z. Yuan, Y. Zhao, H. Zhang, H. Zhang, X. Li, *Chem. Soc. Rev.* **2017**, *46*, 2199; c) R. Darling, K. Gallagher, W. Xie, L. Su, F. Brushett, *J. Electrochem. Soc.* **2016**, *163*, A5029; d) H. Prifti, A. Parasuraman, S. Winardi, T. M. Lim, M. Skyllas-Kazacos, *Membranes* **2012**, *2*, 275.
- [48] X. Wei, Z. Nie, Q. Luo, B. Li, V. Sprenkle, W. Wang, *J. Electrochem. Soc.* **2013**, *160*, A1215.
- [49] T. K. Hoang, P. Chen, *RSC Adv.* **2015**, *5*, 72805.
- [50] a) L. Ling, M. Xiao, D. Han, S. Ren, S. Wang, Y. Meng, *J. Membr. Sci.* **2019**, *585*, 230; b) Y. Zhang, L. Zheng, B. Liu, H. Wang, H. Shi, *J. Membr. Sci.* **2019**, *584*, 173; c) L. Zhang, L. Ling, M. Xiao, D. Han, S. Wang, Y. Meng, *J. Power Sources* **2017**, *352*, 111; d) X. Teng, J. Dai, J. Su, G. Yin, *J. Membr. Sci.* **2015**, *476*, 20.
- [51] a) M. Dassisti, G. Cozzolino, M. Chimienti, A. Rizzuti, P. Mastorilli, P. L'Abbate, *Int. J. Hydrogen Energy* **2016**, *41*, 16477; b) W. Li, R. Zaffou, C. C. Sholvin, M. L. Perry, Y. She, *ECS Trans.* **2013**, *53*, 93; c) B. G. Kim, S. J. Lee, *Google Patents*, **2016**; d) A. Parasuraman, T. M. Lim, C. Menictas, M. Skyllas-Kazacos, *Electrochim. Acta* **2013**, *101*, 27; e) S. Kim, M. Vijayakumar, W. Wang, J. Zhang, B. Chen, Z. Nie, F. Chen, J. Hu, L. Li, Z. Yang, *Phys. Chem. Chem. Phys.* **2011**, *13*, 18186; f) M. Skyllas-Kazacos, L. Cao, M. Kazacos, N. Kausar, A. Mousa, *ChemSusChem* **2016**, *9*, 1521.
- [52] Y. Zhao, L. Liu, X. Qiu, J. Xi, *Electrochim. Acta* **2019**, *303*, 21.
- [53] a) L. Cao, M. Skyllas-Kazacos, C. Menictas, J. Noack, *J. Energy Chem.* **2018**, *27*, 1269; b) A. Mousa, M. Skyllas-Kazacos, *ChemElectroChem* **2015**, *2*, 1742; c) X. Wu, J. Liu, X. Xiang, J. Zhang, J. Hu, Y. Wu, *Pure Appl. Chem.* **2014**, *86*, 661; d) J. G. Lee, S. J. Park, Y. I. Cho, Y. G. Shul, *RSC Adv.* **2013**, *3*, 21347.
- [54] D. N. Buckley, D. Oboroceanu, N. Quill, C. Lenihan, D. N. Eidehin, S. P. Albu, R. P. Lynch, *J. Electrochem. Soc.* **2018**, *165*, A3263.
- [55] a) Y. Lei, B. W. Zhang, B. F. Bai, T. S. Zhao, *J. Power Sources* **2015**, *299*, 202; b) Y. Lei, B. W. Zhang, Z. H. Zhang, B. F. Bai, T. S. Zhao, *Appl. Energy* **2018**, *215*, 591.
- [56] a) K. Kontturi, L. Murtomäki, J. A. Manzanares, *Ionic transport Processes: In Electrochemistry and Membrane Science*, Oxford University Press, Oxford **2008**; b) K. Knehr, E. Agar, C. Dennison, A. Kalidindi, E. Kumbur, *J. Electrochem. Soc.* **2012**, *159*, A1446.
- [57] a) Y. Wang, L. Hao, *J. Electrochem. Soc.* **2019**, *166*, A3784; b) L. Hao, Y. Wang, Y. He, *J. Electrochem. Soc.* **2019**, *166*, A1310.
- [58] a) P. Hamilton, B. Pollet, *Fuel Cells* **2010**, *10*, 489; b) Q. Xu, T. Zhao, P. Leung, *Appl. Energy* **2013**, *105*, 47; c) S. Kumar, S. Jayanti, *J. Power Sources* **2016**, *307*, 782.
- [59] B. H. Lim, E. H. Majlan, W. R. W. Daud, M. I. Rosli, T. Husaini, *Int. J. Hydrogen Energy* **2017**, *42*, 9210.
- [60] K. M. Lisboa, J. Marschewski, N. Ebejer, P. Ruch, R. M. Cotta, B. Michel, D. Poulikakos, *J. Power Sources* **2017**, *359*, 322.
- [61] J. Houser, A. Pezeshki, J. T. Clement, D. Aaron, M. M. Mench, *J. Power Sources* **2017**, *351*, 96.
- [62] Y. Zeng, F. Li, F. Lu, X. Zhou, Y. Yuan, X. Cao, B. Xiang, *Appl. Energy* **2019**, *238*, 435.
- [63] M. Yue, Q. Zheng, F. Xing, H. Zhang, X. Li, X. Ma, *AIChE J.* **2018**, *64*, 782.
- [64] J. Marschewski, L. Brenner, N. Ebejer, P. Ruch, B. Michel, D. Poulikakos, *Energy Environ. Sci.* **2017**, *10*, 780.
- [65] D. S. Aaron, Q. Liu, Z. Tang, G. M. Grim, A. B. Papandrew, A. Turhan, T. A. Zawodzinski, M. M. Mench, *J. Power Sources* **2012**, *206*, 450.
- [66] A. Khazaeli, A. Vatani, N. Tahouni, M. H. Panjeshahi, *J. Power Sources* **2015**, *293*, 599.
- [67] a) A. Tang, J. Bao, M. Skyllas-Kazacos, *J. Power Sources* **2014**, *248*, 154; b) A. Tang, S. Ting, J. Bao, M. Skyllas-Kazacos, *J. Power Sources* **2012**, *203*, 165.
- [68] a) Z. Wei, J. Zhao, B. Xiong, *Appl. Energy* **2014**, *135*, 1; b) Y. Zhang, J. Zhao, P. Wang, M. Skyllas-Kazacos, B. Xiong, R. Badrinarayanan, *J. Power Sources* **2015**, *290*, 14.

- [69] a) X. Ma, H. Zhang, C. Sun, Y. Zou, T. Zhang, *J. Power Sources* **2012**, 203, 153; b) B. Xiong, J. Zhao, K. J. Tseng, M. Skyllas-Kazacos, T. M. Lim, Y. Zhang, *J. Power Sources* **2013**, 242, 314.
- [70] X. Z. Yuan, C. Song, A. Platt, N. Zhao, H. Wang, H. Li, K. Fatih, D. Jang, *Int. J. Energy Res.* **2019**, 43, 6599.
- [71] a) S. Yin, L. Zhou, X. Du, Y. Yang, *Ionics* **2019**, 25, 593; b) Y. Yan, Y. Li, M. Skyllas-Kazacos, J. Bao, *J. Power Sources* **2016**, 322, 116; c) L. Wei, T. S. Zhao, Q. Xu, X. L. Zhou, Z. H. Zhang, *Appl. Energy* **2017**, 190, 1112.
- [72] a) C. Zhang, T. S. Zhao, Q. Xu, L. An, G. Zhao, *Appl. Energy* **2015**, 155, 349; b) Y. Yan, M. Skyllas-Kazacos, J. Bao, *J. Energy Storage* **2017**, 11, 104.
- [73] a) E. Sum, M. Skyllas-Kazacos, *J. Power Sources* **1985**, 15, 179; b) E. Sum, M. Rychcik, M. Skyllas-Kazacos, *J. Power Sources* **1985**, 16, 85.
- [74] R. F. Service, New generation of 'flow batteries' could eventually sustain a grid powered by the sun and wind, <https://www.sciencemag.org/news/2018/10/new-generation-flow-batteries-could-eventually-sustain-grid-powered-sun-and-wind> (accessed: June 2019).
- [75] H. R. Jiang, J. Sun, L. Wei, M. C. Wu, W. Shyy, T. S. Zhao, *Energy Storage Mater.* **2020**, 24, 529.
- [76] B. Liu, M. Zheng, J. Sun, Z. Yu, *J. Energy Storage* **2019**, 23, 278.
- [77] a) M. Kazacos, M. Cheng, M. Skyllas-Kazacos, *J. Appl. Electrochem.* **1990**, 20, 463; b) F. Rahman, M. Skyllas-Kazacos, *J. Power Sources* **1998**, 72, 105; c) N. Kausar, R. Howe, M. Skyllas-Kazacos, *J. Appl. Electrochem.* **2001**, 31, 1327; d) M. Skyllas-Kazacos, D. Kasherman, D. Hong, M. Kazacos, *J. Power Sources* **1991**, 35, 399.
- [78] a) C. Ding, H. Zhang, X. Li, T. Liu, F. Xing, *J. Phys. Chem. Lett.* **2013**, 4, 1281; b) C. Doetsch, J. Burfeind, *Storing Energy*, Elsevier, Amsterdam **2016**, Ch. 12, p. 227; c) C. Blanc, *Ph.D. Thesis*, École polytechnique fédérale de lausanne, **2009**.
- [79] C. Choi, H. Noh, S. Kim, R. Kim, J. Lee, J. Heo, H.-T. Kim, *J. Energy Storage* **2019**, 21, 321.
- [80] M. Li, T. Hikihara, *IEICE Trans. Fundam. Electron., Commun. Comput. Sci.* **2008**, 91, 1741.
- [81] A. Shah, M. Watt-Smith, F. Walsh, *Electrochim. Acta* **2008**, 53, 8087.
- [82] H. Al-Fetlawi, A. A. Shah, F. C. Walsh, *Electrochim. Acta* **2009**, 55, 78.
- [83] A. A. Shah, H. Al-Fetlawi, F. C. Walsh, *Electrochim. Acta* **2010**, 55, 1125.
- [84] H. Al-Fetlawi, A. A. Shah, F. C. Walsh, *Electrochim. Acta* **2010**, 55, 3192.
- [85] D. You, H. Zhang, J. Chen, *Electrochim. Acta* **2009**, 54, 6827.
- [86] M. Vynnycky, *Energy* **2011**, 36, 2242.
- [87] D. You, H. Zhang, C. Sun, X. Ma, *J. Power Sources* **2011**, 196, 1578.
- [88] A. A. Shah, R. Tangirala, R. Singh, R. G. A. Wills, F. C. Walsh, *J. Electrochem. Soc.* **2011**, 158, A671.
- [89] I. M. Bayanov, R. Vanhaelst, *J. Math. Chem.* **2011**, 49, 2013.
- [90] X. Ma, H. Zhang, F. Xing, *Electrochim. Acta* **2011**, 58, 238.
- [91] K. Knehr, E. Kumbur, *Electrochim. Commun.* **2011**, 13, 342.
- [92] a) B. Xiong, J. Zhao, J. Li, presented at 2013 IEEE Power & Energy Society General Meeting, Vancouver, British Columbia, Canada, July **2013**; b) J. Fu, M. Zheng, X. Wang, J. Sun, T. Wang, *J. Energy Eng.* **2017**, 143, 04017064; c) S. König, M. R. Suriyah, T. Leibfried, presented at IREC2015 The Sixth International Renewable Energy Congress, Tunisia **2015**; d) S. König, M. R. Suriyah, T. Leibfried, *J. Power Sources* **2016**, 333, 134; e) D. K. Kim, S. J. Yoon, J. Lee, S. Kim, *Appl. Energy* **2018**, 228, 891; f) T. Wang, J. Fu, M. Zheng, Z. Yu, *Appl. Energy* **2018**, 227, 613.
- [93] a) C. R. Dennison, E. Agar, B. Akuzum, E. C. Kumbur, *J. Electrochem. Soc.* **2016**, 163, A5163; b) J. Houser, J. Clement, A. Pezeshki, M. M. Mench, *J. Power Sources* **2016**, 302, 369; c) T. Jayanti, J. Appl. Electrochem. **2014**, 44, 995; d) T. J. Latha, S. Jayanti, *J. Power Sources* **2014**, 248, 140; e) Q. Xu, T. S. Zhao, C. Zhang, *Electrochim. Acta* **2014**, 142, 61.
- [94] B. W. Zhang, Y. Lei, B. F. Bai, T. S. Zhao, *Int. J. Heat Mass Transfer* **2019**, 135, 460.
- [95] a) R. Gundlapalli, S. Jayanti, *J. Energy Storage* **2019**, 23, 148; b) J. Lee, J. Kim, H. Park, *Int. J. Hydrogen Energy* **2019**, 44, 29483; c) M. Al-Yasiri, J. Park, *J. Electrochem. Soc.* **2017**, 164, A1970.
- [96] Q. Zheng, F. Xing, X. Li, G. Ning, H. Zhang, *J. Power Sources* **2016**, 324, 402.
- [97] C. Yin, Y. Gao, S. Guo, H. Tang, *Energy* **2014**, 74, 886.
- [98] H. Ishitobi, J. Saito, S. Sugawara, K. Oba, N. Nakagawa, *Electrochim. Acta* **2019**, 313, 513.
- [99] C. Yin, Y. Gao, G. Xie, T. Li, H. Tang, *J. Power Sources* **2019**, 438.
- [100] C.-H. Chen, K. Yaji, S. Yamasaki, S. Tushima, K. Fujita, *J. Energy Storage* **2019**, 26.
- [101] M. Messaggi, P. Canzi, R. Mereu, A. Baricci, F. Inzoli, A. Casalegno, M. Zago, *Appl. Energy* **2018**, 228, 1057.
- [102] M. Messaggi, C. Rabissi, C. Gambaro, L. Meda, A. Casalegno, M. Zago, *J. Power Sources* **2020**, 449, 227588.
- [103] S. Maurya, P. T. Nguyen, Y. S. Kim, Q. Kang, R. Mukundan, *J. Power Sources* **2018**, 404, 20.
- [104] a) Y.-P. Sun, K. Scott, *Chem. Eng. J.* **2004**, 102, 83; b) M. M. Saleh, *J. Phys. Chem. B* **2004**, 108, 13419; c) S. Devan, V. R. Subramanian, R. E. White, *J. Electrochem. Soc.* **2005**, 152.
- [105] P. A. Boettcher, E. Agar, C. R. Dennison, E. C. Kumbur, *J. Electrochem. Soc.* **2016**, 163, A5244.
- [106] J. Newman, E. Thomas-Alyea, *Electrochemical Systems*, John Wiley & Sons, New York **2004**.
- [107] a) S. Won, K. Oh, H. Ju, *Electrochim. Acta* **2015**, 177, 310; b) Y. A. Gandomi, D. Aaron, M. Mench, *Electrochim. Acta* **2016**, 218, 174; c) D. K. Kim, S. J. Yoon, S. Kim, *Int. J. Heat Mass Transfer* **2020**, 148.
- [108] J. S. Lawton, A. M. Jones, Z. Tang, M. Lindsey, T. Zawodzinski, *J. Electrochem. Soc.* **2017**, 164, A2987.
- [109] a) A. Tang, J. Bao, M. Skyllas-Kazacos, *J. Power Sources* **2011**, 196, 10737; b) M. Skyllas-Kazacos, L. Goh, *J. Membr. Sci.* **2012**, 399400, 43.
- [110] K. Oh, S. Won, H. Ju, *Electrochim. Acta* **2015**, 181, 238.
- [111] K. W. Knehr, E. C. Kumbur, *Electrochim. Commun.* **2012**, 23, 76.
- [112] R. M. Darling, A. Z. Weber, M. C. Tucker, M. L. Perry, *J. Electrochem. Soc.* **2016**, 163, A5014.
- [113] M. Pugach, M. Kondratenko, S. Briola, A. Bischi, *Appl. Energy* **2018**, 226, 560.
- [114] E. Agar, K. Knehr, D. Chen, M. A. Hickner, E. Kumbur, *Electrochim. Acta* **2013**, 98, 66.
- [115] X.-G. Yang, Q. Ye, P. Cheng, T. S. Zhao, *Appl. Energy* **2015**, 145, 306.
- [116] C. Sun, J. Chen, H. Zhang, X. Han, Q. Luo, *J. Power Sources* **2010**, 195, 890.
- [117] a) T. A. Zawodzinski, C. Derouin, S. Radzinski, R. J. Sherman, V. T. Smith, T. E. Springer, S. Gottesfeld, *J. Electrochem. Soc.* **1993**, 140, 1041; b) T. Mohammadi, M. Skyllas-Kazacos, *J. Power Sources* **1996**, 63, 179; c) T. Mohammadi, S. C. Chieng, M. S. Kazacos, *J. Membr. Sci.* **1997**, 133, 151; d) T. Sukkar, M. Skyllas-Kazacos, *J. Membr. Sci.* **2003**, 222, 235; e) T. Sukkar, M. Skyllas-Kazacos, *J. Membr. Sci.* **2003**, 222, 249.
- [118] K. Oh, M. Moazzam, G. Gwak, H. Ju, *Electrochim. Acta* **2019**, 297, 101.
- [119] a) Z. Jiang, K. Klyukin, K. Miller, V. Alexandrov, *J. Phys. Chem. B* **2019**, 123, 3976; b) A. A. Shinkle, A. E. Sleightholme, L. T. Thompson, C. W. Monroe, *J. Appl. Electrochem.* **2011**, 41, 1191.
- [120] a) Z. Yang, J. Zhang, M. C. Kintner-Meyer, X. Lu, D. Choi, J. P. Lemmon, J. Liu, *Chem. Rev.* **2011**, 111, 3577; b) A. Trovò, A. Saccardo, M. Giomo, M. Guarneri, *J. Power Sources* **2019**, 424, 204; c) F. Wandschneider, S. Röhm, P. Fischer, K. Pinkwart, J. Tübke, H. Nirschl, *J. Power Sources* **2014**, 261, 64.
- [121] a) F. Xing, H. Zhang, X. Ma, *J. Power Sources* **2011**, 196, 10753; b) M. Skyllas-Kazacos, J. McCann, Y. Li, J. Bao, A. Tang, *ChemistrySelect* **2016**, 1, 2249.

- [122] a) H. Fink, M. Remy, *J. Power Sources* **2015**, *284*, 547; b) J. A. Schaeffer, L.-D. Chen, J. P. Seaba, *J. Power Sources* **2008**, *182*, 599.
- [123] a) P. R. Prokopius, *Contract* **1976**, *506*, 23; b) N. Hagedorn, M. Hoberecht, L. Thaller, *NASA Lewis Research Centre*, Cleveland, OH, USA **1982**.
- [124] F. Moro, A. Trovò, S. Bortolin, D. Del Col, M. Guarnieri, *J. Power Sources* **2017**, *340*, 229.
- [125] F. T. Wandschneider, S. Röhm, P. Fischer, K. Pinkwart, J. Tübke, H. Nirschl, *J. Power Sources* **2014**, *261*, 64.
- [126] Q. Ye, J. Hu, P. Cheng, Z. Ma, *J. Power Sources* **2015**, *296*, 352.
- [127] B. R. Munson, D. F. Young, T. H. Okiishi, *Oceanogr. Lit. Rev.* **1995**, *10*, 831.
- [128] M. Zahn, P. G. Grimes, R. J. Bellows, *Google Patents*, **1980**.
- [129] A. Trovò, G. Marini, A. Sutto, P. Alotto, M. Giomo, F. Moro, M. Guarnieri, *Appl. Energy* **2019**, *240*, 893.
- [130] C. Yin, S. Guo, H. Fang, J. Liu, Y. Li, H. Tang, *Appl. Energy* **2015**, *151*, 237.
- [131] a) L. Eifert, Z. Jusys, R. J. Behm, R. Zeis, *Carbon* **2020**, *158*, 580; b) L. Eifert, R. Banerjee, Z. Jusys, R. Zeis, *J. Electrochem. Soc.* **2018**, *165*, A2577; c) R. Schweiss, A. Pritzl, C. Meiser, *J. Electrochem. Soc.* **2016**, *163*, A2089.
- [132] S. Rudolph, U. Schröder, I. M. Bayanov, G. Pfeiffer, *J. Electroanal. Chem.* **2013**, *709*, 93.
- [133] L. Liu, Z. Li, J. Xi, H. Zhou, Z. Wu, X. Qiu, *Appl. Energy* **2017**, *185*, 452.
- [134] F. Chen, J. Liu, H. Chen, C. Yan, *Int. J. Electrochem. Sci.* **2012**, *7*, 3750.
- [135] E. Agar, C. R. Dennison, K. W. Knehr, E. C. Kumbur, *J. Power Sources* **2013**, *225*, 89.
- [136] H. Liu, Q. Xu, C. Yan, Y. Qiao, *Electrochim. Acta* **2011**, *56*, 8783.
- [137] A. A. Shah, M. J. Watt-Smith, F. C. Walsh, *Electrochim. Acta* **2008**, *53*, 8087.
- [138] A. A. Franco, *RSC Adv.* **2013**, *3*, 13027.
- [139] J. Bao, V. Murugesan, C. J. Kamp, Y. Shao, L. Yan, W. Wang, *Adv. Theory Simul.* **2019**, *3*, 1900167.
- [140] A. Hazza, D. Pletcher, R. Wills, *Phys. Chem. Chem. Phys.* **2004**, *6*, 1773.
- [141] C. P. Zhang, S. M. Sharkh, X. Li, F. C. Walsh, C. N. Zhang, J. C. Jiang, *Energy Convers. Manage.* **2011**, *52*, 3391.
- [142] M. Krishna, R. G. A. Wills, A. A. Shah, D. Hall, J. Collins, *J. Appl. Electrochem.* **2018**, *48*, 1031.
- [143] a) M. G. Verde, K. J. Carroll, Z. Wang, A. Sathrum, Y. S. Meng, *Energy Environ. Sci.* **2013**, *6*, 1573; b) M. Lanfranconi, H.-J. Lilienhof, *J. Sustainable Dev. Energy, Water Environ. Syst.* **2019**, *7*, 343; c) Y.-T. Lin, H.-L. Tan, C.-Y. Lee, H.-Y. Chen, *Electrochim. Acta* **2018**, *263*, 60.
- [144] M. Krishna, E. J. Fraser, R. G. A. Wills, F. C. Walsh, *J. Energy Storage* **2018**, *15*, 69.
- [145] R. G. A. Wills, J. Collins, D. Stratton-Campbell, C. T. J. Low, D. Pletcher, F. C. Walsh, *J. Appl. Electrochem.* **2010**, *40*, 955.
- [146] D. Pletcher, R. Wills, *J. Power Sources* **2005**, *149*, 96.
- [147] A. Oury, A. Kirchev, Y. Bultel, E. Chainet, *Electrochim. Acta* **2012**, *71*, 140.
- [148] A. A. Shah, X. Li, R. G. A. Wills, F. C. Walsh, *J. Electrochem. Soc.* **2010**, *157*.
- [149] A. Bates, S. Mukerjee, S. C. Lee, D.-H. Lee, S. Park, *J. Power Sources* **2014**, *249*, 207.
- [150] M. N. Nandanwar, S. Kumar, *J. Electrochem. Soc.* **2014**, *161*, A1602.
- [151] M. Nandanwar, S. Kumar, *Chem. Eng. Sci.* **2016**, *154*, 61.
- [152] a) P. E. Pascoe, A. H. Anbukey, *J. Power Sources* **2002**, *111*, 304; b) A. Delaille, M. Perrin, F. Huet, L. Hernout, *J. Power Sources* **2006**, *158*, 1019.
- [153] A. Oury, A. Kirchev, Y. Bultel, *J. Power Sources* **2014**, *246*, 703.
- [154] M. Nandanwar, S. Kumar, *J. Power Sources* **2019**, *412*, 536.
- [155] J. Collins, G. Kear, X. Li, C. T. J. Low, D. Pletcher, R. Tangirala, D. Stratton-Campbell, F. C. Walsh, C. Zhang, *J. Power Sources* **2010**, *195*, 1731.
- [156] a) E. Ventosa, D. Buchholz, S. Klink, C. Flox, L. G. Chagas, C. Vaalma, W. Schuhmann, S. Passerini, J. R. Morante, *Chem. Commun.* **2015**, *51*, 7298; b) Z. Li, K. C. Smith, Y. Dong, N. Baram, F. Y. Fan, J. Xie, P. Limthongkul, W. C. Carter, Y. M. Chiang, *Phys. Chem. Chem. Phys.* **2013**, *15*, 15833.
- [157] E. Ventosa, G. Zampardi, C. Flox, F. La Mantia, W. Schuhmann, J. R. Morante, *Chem. Commun.* **2015**, *51*, 14973.
- [158] E. Ventosa, O. Amedu, W. Schuhmann, *ACS Appl. Energy Mater.* **2018**, *1*, 5158.
- [159] a) S. Hamelet, T. Tzedakis, J. B. Leriche, S. Sailler, D. Larcher, P. L. Taberna, P. Simon, J. M. Tarascon, *J. Electrochem. Soc.* **2012**, *159*, A1360; b) H. Chen, N.-C. Lai, Y.-C. Lu, *Chem. Mater.* **2017**, *29*, 7533; c) C. Wang, Q. Lai, P. Xu, X. Li, H. Zhang, *Chin. Chem. Lett.* **2018**, *29*, 716.
- [160] a) V. E. Brunini, Y.-M. Chiang, W. C. Carter, *Electrochim. Acta* **2012**, *69*, 301; b) K. Chayambuka, J. Fransaer, X. Dominguez-Benetton, *J. Power Sources* **2019**, *434*, 226740; c) R. Lacroix, J. J. Biendicho, G. Mulder, L. Sanz, C. Flox, J. R. Morante, S. Da Silva, *Electrochim. Acta* **2019**, *304*, 146.
- [161] G. Shukla, A. A. Franco, *J. Phys. Chem. C* **2018**, *122*, 23867.
- [162] a) B. Huskinson, M. P. Marshak, C. Suh, S. Er, M. R. Gerhardt, C. J. Galvin, X. Chen, A. Aspuru-Guzik, R. G. Gordon, M. J. Aziz, *Nature* **2014**, *505*, 195; b) G. L. Soloveichik, *Nature* **2014**, *505*, 163; c) Z. Li, Y.-C. Lu, *Chem* **2018**, *4*, 2020.
- [163] a) J. A. Kowalski, L. Su, J. D. Milshtein, F. R. Brushett, *Curr. Opin. Chem. Eng.* **2016**, *13*, 45; b) H. Chen, G. Cong, Y.-C. Lu, *J. Energy Chem.* **2018**, *27*, 1304.
- [164] a) J. D. Milshtein, J. L. Barton, R. M. Darling, F. R. Brushett, *J. Power Sources* **2016**, *327*, 151; b) S.-K. Park, J. Shim, J. Yang, K.-H. Shin, C.-S. Jin, B. S. Lee, Y.-S. Lee, J.-D. Jeon, *Electrochem. Commun.* **2015**, *59*, 68; c) F. R. Brushett, J. T. Vaughney, A. N. Jansen, *Adv. Energy Mater.* **2012**, *2*, 1390.
- [165] a) Q. Chen, M. R. Gerhardt, L. Hartle, M. J. Aziz, *J. Electrochem. Soc.* **2016**, *163*, A5010; b) Q. Chen, L. Eisenach, M. J. Aziz, *J. Electrochem. Soc.* **2016**, *163*, A5057.
- [166] a) X. Li, *Electrochim. Acta* **2015**, *170*, 98; b) D. Chu, X. Li, S. Zhang, *Electrochim. Acta* **2016**, *190*, 434.
- [167] S. Er, C. Suh, M. P. Marshak, A. Aspuru-Guzik, *Chem. Sci.* **2015**, *6*, 885.
- [168] a) J. Cheng, L. Zhang, Y.-S. Yang, Y.-H. Wen, G.-P. Cao, X.-D. Wang, *Electrochim. Commun.* **2007**, *9*, 2639; b) L. Zhang, J. Cheng, Y.-S. Yang, Y.-H. Wen, X.-D. Wang, G.-P. Cao, *J. Power Sources* **2008**, *179*, 381.
- [169] Y. Cheng, H. Zhang, Q. Lai, X. Li, D. Shi, *Electrochim. Acta* **2013**, *105*, 618.
- [170] Y. Cheng, H. Zhang, Q. Lai, X. Li, D. Shi, L. Zhang, *J. Power Sources* **2013**, *241*, 196.
- [171] J. Cheng, Y.-H. Wen, G.-P. Cao, Y.-S. Yang, *J. Power Sources* **2011**, *196*, 1589.
- [172] Y. Cheng, X. Xi, D. Li, X. Li, Q. Lai, H. Zhang, *RSC Adv.* **2015**, *5*, 1772.
- [173] A. Khor, P. Leung, M. R. Mohamed, C. Flox, Q. Xu, L. An, R. G. A. Wills, J. R. Morante, A. A. Shah, *Mater. Today Energy* **2018**, *8*, 80.
- [174] J. Winsberg, T. Janoschka, S. Morgenstern, T. Hagemann, S. Muench, G. Hauffman, J. F. Gohy, M. D. Hager, U. S. Schubert, *Adv. Mater.* **2016**, *28*, 2238.
- [175] S. Li, K. Li, E. Xiao, R. Xiong, J. Zhang, P. Fischer, *J. Power Sources* **2020**, *445*, 227282.
- [176] a) S. Yao, P. Liao, M. Xiao, J. Cheng, K. He, *AIP Adv.* **2016**, *6*, 125; b) S. Yao, P. Liao, M. Xiao, J. Cheng, K. He, *AIP Adv.* **2017**, *7*, 055112; c) S. Yao, P. Liao, M. Xiao, J. Cheng, W. Cai,

- Energies* **2017**, *10*, 1101; d) S. Yao, Y. Zhao, X. Sun, Q. Zhao, J. Cheng, *Electrochim. Acta* **2019**, *307*, 573; e) S. Yao, X. Sun, Y. Chen, M. Xiao, J. Cheng, Y. Shen, *J. Renewable Sustainable Energy* **2019**, *11*, 024105; f) S. Yao, H. Wu, M. Xiao, J. Cheng, Y. Shen, *Int. J. Electrochem. Sci.* **2019**, *14*, 8340; g) M. Xiao, Y. Wang, S. Yao, Y. Song, J. Cheng, K. He, *J. Renewable Sustainable Energy* **2016**, *8*, 064102; h) S. Yao, Y. Zhao, X. Sun, D. Ding, J. Cheng, *Int. J. Electrochem. Sci.* **2019**, *14*, 2160; i) S. G. Yao, L. K. Xu, Z. Y. Sun, J. Cheng, *Int. J. Heat Mass Transfer* **2019**, *138*, 903; j) X. Sun, S. Yao, Q. Zhao, Y. Zhao, J. Cheng, *Int. J. Electrochem. Sci.* **2020**, *15*, 651.
- [177] H. Lim, A. Lackner, R. Knechtli, *J. Electrochem. Soc.* **1977**, *124*, 1154.
- [178] Q. Lai, H. Zhang, X. Li, L. Zhang, Y. Cheng, *J. Power Sources* **2013**, *235*, 1.
- [179] H. S. Yang, J. H. Park, H. W. Ra, C.-S. Jin, J. H. Yang, *J. Power Sources* **2016**, *325*, 446.
- [180] M. C. Wu, T. S. Zhao, L. Wei, H. R. Jiang, R. H. Zhang, *J. Power Sources* **2018**, *384*, 232.
- [181] T. Evans, R. E. White, *J. Electrochem. Soc.* **1987**, *134*, 866.
- [182] E. Manla, A. Nasiri, C. H. Rentel, M. Hughes, *IEEE Trans. Ind. Electron.* **2010**, *57*, 624.
- [183] B. Koo, D. Lee, J. Yi, C. B. Shin, D. J. Kim, E. M. Choi, T. H. Kang, *Energies* **2019**, *12*, 1159.
- [184] a) U. S. Kim, J. Yi, C. B. Shin, T. Han, S. Park, *J. Power Sources* **2011**, *196*, 5115; b) U. S. Kim, C. B. Shin, C.-S. Kim, *J. Power Sources* **2009**, *189*, 841.
- [185] Z. Xu, J. Wang, S. C. Yan, Q. Fan, P. D. Lund, *J. Power Sources* **2020**, *450*, 227436.
- [186] a) R. Yeo, D. T. Chin, *J. Electrochem. Soc.* **1980**, *127*, 549; b) Y. V. Tolmachev, *Russ. J. Electrochem.* **2014**, *50*, 301.
- [187] a) K. T. Cho, P. Ridgway, A. Z. Weber, S. Haussener, V. Battaglia, V. Srinivasan, *J. Electrochem. Soc.* **2012**, *159*, A1806; b) X. You, Q. Ye, T. Van Nguyen, P. Cheng, *J. Electrochem. Soc.* **2016**, *163*, A447.
- [188] a) M. C. Tucker, K. T. Cho, A. Z. Weber, G. Lin, T. Van Nguyen, *J. Appl. Electrochem.* **2015**, *45*, 11; b) K. T. Cho, M. C. Tucker, M. Ding, P. Ridgway, V. S. Battaglia, V. Srinivasan, A. Z. Weber, *ChemPlusChem* **2015**, *80*, 402.
- [189] K. Saadi, P. Nanikashvili, Z. Tatus-Portnoy, S. Hardisty, V. Shokhen, M. Zysler, D. Zitoun, *J. Power Sources* **2019**, *422*, 84.
- [190] W. A. Braff, M. Z. Bazant, C. R. Buie, *Nat. Commun.* **2013**, *4*, 2346.
- [191] a) W. A. Braff, C. R. Buie, *ECS Trans.* **2011**, *33*, 179; b) V. Yarlagadda, T. Van Nguyen, *J. Electrochem. Soc.* **2013**, *160*, F535.
- [192] R. Zhang, T. G. Stanford, L. Wolters, J. Weidner, *ECS Trans.* **2011**, *33*, 169.
- [193] R. Zhang, J. W. Weidner, *J. Appl. Electrochem.* **2011**, *41*, 1245.
- [194] K. Oh, T. J. Kang, S. Park, M. C. Tucker, A. Z. Weber, H. Ju, *Electrochim. Acta* **2017**, *230*, 160.
- [195] a) X. Zhang, X.-G. Wang, Z. Xie, Z. Zhou, *Green Energy Environ.* **2016**, *1*, 4; b) U. Sahapatsombut, H. Cheng, K. Scott, *J. Energy Storage* **2016**, *7*, 220.
- [196] J. Huang, A. Faghri, *Electrochim. Acta* **2015**, *174*, 908.
- [197] X. Li, J. Huang, A. Faghri, *Energy* **2015**, *81*, 489.
- [198] X. Xia, H.-T. Liu, Y. Liu, *J. Electrochem. Soc.* **2002**, *149*, A426.
- [199] Y. Liu, X. Xia, H. Liu, *J. Power Sources* **2004**, *130*, 299.
- [200] a) S. Smith, I. Firdous, Q. Wang, S. Esmalla, W. A. Daoud, *Electrochim. Acta* **2019**, *328*, 135019; b) M. Govindan, K. He, I.-S. Moon, *Int. J. Electrochem. Sci.* **2013**, *8*, 10265; c) P. K. Leung, M. R. Mohamed, A. A. Shah, Q. Xu, M. B. Conde-Duran, *J. Power Sources* **2015**, *274*, 651.
- [201] S. Sankarasubramanian, Y. Zhang, V. Ramani, *Sustainable Energy Fuels* **2019**, *3*, 2417.
- [202] G. J. May, A. Davidson, B. Monahov, *J. Energy Storage* **2018**, *15*, 145.
- [203] X. L. Zhou, T. S. Zhao, L. An, Y. K. Zeng, X. H. Yan, *Appl. Energy* **2015**, *158*, 157.
- [204] G. Merei, S. Adler, D. Magnor, D. U. Sauer, *Electrochim. Acta* **2015**, *174*, 945.
- [205] Y. Li, M. Skyllas-Kazacos, J. Bao, *J. Power Sources* **2016**, *311*, 57.
- [206] S. Won, K. Oh, H. Ju, *Electrochim. Acta* **2016**, *201*, 286.
- [207] S. König, M. R. Suriyah, T. Leibfried, *J. Power Sources* **2017**, *360*, 221.
- [208] X. Ke, J. M. Prahl, J. I. D. Alexander, R. F. Savinell, *Electrochim. Acta* **2017**, *223*, 124.
- [209] H. Chen, X. Li, H. Gao, J. Liu, C. Yan, A. Tang, *Appl. Energy* **2019**, *247*, 13.
- [210] E. Ali, H. Kwon, J. Choi, J. Lee, J. Kim, H. Park, *J. Energy Storage* **2020**, *28*, 101208.
- [211] C. Yuan, F. Xing, Q. Zheng, H. Zhang, X. Li, X. Ma, *Energy* **2020**, *194*, 116839.